



HAL
open science

Viscoelasticity of model aggregate polymer nanocomposites

Yang Wang

► **To cite this version:**

Yang Wang. Viscoelasticity of model aggregate polymer nanocomposites. Mathematical Physics [math-ph]. Université de Lyon, 2018. English. NNT : 2018LYSE1027 . tel-02059856

HAL Id: tel-02059856

<https://theses.hal.science/tel-02059856>

Submitted on 7 Mar 2019

HAL is a multi-disciplinary open access archive for the deposit and dissemination of scientific research documents, whether they are published or not. The documents may come from teaching and research institutions in France or abroad, or from public or private research centers.

L'archive ouverte pluridisciplinaire **HAL**, est destinée au dépôt et à la diffusion de documents scientifiques de niveau recherche, publiés ou non, émanant des établissements d'enseignement et de recherche français ou étrangers, des laboratoires publics ou privés.



N° d'ordre NNT : 2018LYSE1027

THÈSE DE DOCTORAT DE L'UNIVERSITÉ DE LYON

opérée au sein de
l'Université Claude Bernard Lyon 1

École Doctorale ED52
L'école doctorale de Physique et d'Astrophysique (PHAST)

Spécialité de doctorat : Physique de la matière molle
Discipline : Rheologie des polymères nanocomposites

Soutenue publiquement le 06/03/2018, par :
Yang WANG

Viscoelasticity of model aggregate polymer nanocomposites

Devant le jury composé de :

ROUSSEAU Bernard, DR CNRS, Laboratoire de Chimie Physique (Paris Sud)	Rapporteur
PEREZ Michel, Professeur, Laboratoire Mateis (INSA Lyon)	Rapporteur
BARENTIN Catherine, Professeure, Institut Lumière Matière	Examinatrice
JARDAT Marie, Professeure, Laboratoire PHENIX (UPMC)	Examinatrice
OBERDISSE Julian, DR CNRS, Laboratoire Charles Coulomb Montpellier	Examinateur
MERABIA Samy, CR CNRS, Institut Lumière Matière	Directeur de thèse
DETCHEVERRY François, CR CNRS, Institut Lumière Matière	Invité
COUTY Marc, Ingénieur de recherches, Michelin	Invité
MAUREL Gaëtan, Ingénieur de recherches, Michelin	Invité

Acknowledgments

Special thanks to all the jury members for having examined this project of thesis, especially to Pr. Bernard ROUSSEAU and Pr. Michel PEREZ for being the rapporteurs, and all their remarks to better this thesis.

I desire to thank to Pr. Samy MERABIA and Pr. François DETCHEVERRY from the Institut Lumière Matière, who are my supervisors of the thesis, and for having proposed their brilliant remarks and plans for this work. Through their trust and efforts, I could achieve the autonomy and reach the finish-line. Likewise, I'd like to thank Pr. Marc COUTY and Pr. Gaëtan MAUREL from the society MICHELIN for having their confidence on me and their constructive propositions in the last years.

I would love also to thank to all my friends and colleagues in the laboratory and their warmhearted accompanying for these days. The memory with you guys/girls is always a relief for me.

At the end, I could never have finished this project without the endless support from my wife, my parents and my grandparents. Their unconditional love is the one and the only fuel to moving me forward and attaining the ultimate success. This work is particularly dedicated to you, my beloved family.

君子居则终日而
不自息也

甲午秋月于香安

奇哉書



"As heaven maintains vigor through movements, a gentle man should constantly strive for self-perfection", written by my grandfather, as a gift for my journey to France.

Contents

General introduction	1
1 Background	3
1.1 Polymer nanocomposites (PNCs)	4
1.1.1 Applications of PNCs	4
1.1.2 Filler type	4
1.1.3 Aggregates	6
1.1.4 Miscibility of filler	8
1.2 Rheological properties of PNCs	9
1.2.1 Linear rheology	10
1.2.2 LAOS: large amplitude oscillatory shear	12
1.2.3 Payne effect	12
1.2.4 Mullins effect	14
1.2.5 Start up steady deformation	15
1.3 Modeling methods	15
1.3.1 Micro-scale modeling	16
1.3.2 Meso-scale modeling	18
1.3.3 Macroscale modeling	21
1.4 Physical mechanisms	21
1.4.1 Contribution of the polymer	22
1.4.2 Polymer chain structure near surface of filler	23
1.4.3 Filler structure	24
1.4.4 Interface: percolation network	24
1.5 Motivations and objectives of the present work	25
1.6 Appendix: Rheology and viscoelasticity	26
2 Mesoscopic modeling of PNCs	31
2.1 Filler types	32
2.1.1 Individual nanoparticles	32
2.1.2 Aggregates	32
2.2 Simulation method	36
2.2.1 Interparticle potential	36
2.2.2 Brownian dynamics	37
2.2.3 Generalized Langevin dynamics (GLE)	38
2.2.4 Application of the GLE to entangled polymer dynamics	41
2.2.5 System units	42
2.2.6 Initial configurations	42

3	Linear rheology: simulations and results	47
3.1	Stress relaxation modulus	48
3.1.1	Microscopic view of stress tensor	48
3.1.2	Green-Kubo approach	49
3.1.3	Diagonal and cross contributions to the stress	49
3.1.4	Harmonic zone	50
3.2	Influence of filler and matrix parameters	51
3.2.1	Effect of filler type	52
3.2.2	Effect of filler volume fraction	53
3.2.3	Effect of aggregate size	55
3.2.4	Effect of primary particle size	56
3.2.5	Effect of polymer matrix relaxation time	57
3.2.6	Effect of aggregates polydispersity	58
3.2.7	Summary: Reinforcement	58
3.3	Slow dynamics	59
3.3.1	Diffusion coefficient	60
3.3.2	Orientation of aggregates	61
3.3.3	Dynamic structure factor	62
4	Nonlinear rheology: simulations and results	67
4.1	Rheology in nonlinear regime	68
4.1.1	Method in practice	68
4.1.2	Storage and loss modulus	70
4.2	Influence of aggregates properties	71
4.2.1	Effect of filler type	71
4.2.2	Effect of filler volume fraction	72
4.2.3	Effect of aggregate size	73
4.2.4	Effect of polydispersity	74
4.3	High order harmonics	75
4.3.1	Dynamic moduli	75
4.3.2	Shear stress	76
4.4	Filler behavior under LAOS	77
4.4.1	Gyration tensor	77
4.4.2	Results	77
4.5	History-dependent LAOS	80
4.5.1	Single shear cycle	81
4.5.2	Long time relaxation	81
4.5.3	Multiple shear cycles	82
4.6	Aggregates with attractive interaction	83
	General conclusion	89

General introduction

Polymer nanocomposites have drawn a lot of attention both from the academic and industrial research in the last decades, thanks to their remarkable mechanical and rheological properties as compared to pure polymers. Both the fillers and the polymer matrix can be of various types and the possibility of the compounds is theoretically infinite. This opens the way to new materials having tailored properties for specific industrial applications. For instance, polymer nanocomposites are very attractive for tire applications [1, 2]. The presence of the fillers, such as carbon black or silica nanoparticles, in a polymer or rubber matrix can boost the dissipative properties of the formed polymer nanocomposites system and leads to mechanical reinforcement [3]. Furthermore, the polymer nanocomposites system display better shock resistance and wear resistance than the pure polymer matrix. The "Green X" tires from MICHELIN are also specially designed to reduce the fuel consumption.

Among the various kinds of fillers, aggregates have been used in the industrial applications for decades. They can lead to large levels of mechanical reinforcement. Apart from reinforcement, filled polymer composites exhibit nonlinear response, which is generally characterized by a significant drop of the storage modulus. This is referred to as the Payne effect. The Mullins effect, which refers to stress softening in repeated cycles, is another important nonlinear effect observed in filled polymer composites.

In spite of decades of research, the relation between nanocomposites structure and rheology is far from being understood. Macroscopic approaches such as Einstein's law for suspensions or Guth's law in the context of filled elastomers generally fail for the volume fraction typical of applications. The lack of complete understanding so far may come from the various competing mechanisms and factors occurring in polymer nanocomposites and which contribute to reinforcement. First, the state of dispersion of the nanoparticles plays a pivotal role in the reinforcement of polymer nanocomposites [4]. Poorly dispersed nanoparticles could build small aggregates or agglomerates or even mesoscopic clusters, which can enhance the effects of both the filler-filler and polymer-filler interactions. Similarly, fractal-like aggregates are known to display outstanding viscoelastic properties even with relatively low volume fraction [5, 6, 7]. These observations are generally interpreted as a result of the formation of a gel, mediated by filler-filler interactions [8]. The polymer chains near filler may have hindered mobility. The existence of a glassy layer [9, 10] is, however, still in debate since the relaxation dynamics of polymer chains near particles surface is found to be not different from the chain dynamics far away from particles [11], as evidenced experimentally [12, 13].

Simulation approaches, such as Molecular Dynamics, can give a detailed view of the interplay between polymers chains and fillers at an atomistic local scale. This is currently the focus of many studies [14]. However, it is much more difficult to address the properties emerging at a mesoscopic scale. To simulate a large number of aggregates, each at least

100 nm in diameter in an entangled polymeric matrix is presently out of reach.

In this work, we propose a mesoscopic model to simulate polymer nanocomposites and measure the contribution of fillers to the rheological reinforcement. The first ingredient of the model is an explicit description of fillers. Their size and structure can thus be chosen at will. For the sake of comparison, we will consider individual nanoparticles, flexible or rigid aggregates. The second ingredient of the model is an implicit description of the polymeric matrix: it is represented by an effective viscoelastic medium, through a memory kernel which depends on the history of the filler velocity. Again for comparison, we will compare two limiting cases of matrix: a simple fluid and an entangled melt, that are relevant respectively to colloidal suspension and polymer nanocomposites.

In chapter 1, we introduce the general background about the rheology of a polymer nanocomposites. We illustrate some key experimental results and briefly introduce the various theoretical and simulations approaches, as well as the physical mechanisms put forward.

In chapter 2, we explain our modelling of nanocomposites. We describe the aggregates and explain the simulation technique used to represent the viscoelastic matrix.

Chapter 3 is devoted to linear rheology. We use simulation at equilibrium and a Green-Kubo approach. We probe the influence of the key parameters, such as the filler type and the filler volume fraction, etc. We investigate the cause of reinforcement in the stress relaxation modulus $G(t)$ by looking at the motion of aggregates and the dynamic structure factor.

Finally, chapter 4 addresses non-linear rheology. Our simple model of nanocomposite exhibits the Payne effect, which we study in detail. We also try to relate the microscopic structure of aggregates to the macroscopic behavior of the material.

CHAPTER 1

Background

Contents

1.1	Polymer nanocomposites (PNCs)	4
1.1.1	Applications of PNCs	4
1.1.2	Filler type	4
1.1.3	Aggregates	6
1.1.4	Miscibility of filler	8
1.2	Rheological properties of PNCs	9
1.2.1	Linear rheology	10
1.2.2	LAOS: large amplitude oscillatory shear	12
1.2.3	Payne effect	12
1.2.4	Mullins effect	14
1.2.5	Start up steady deformation	15
1.3	Modeling methods	15
1.3.1	Micro-scale modeling	16
1.3.2	Meso-scale modeling	18
1.3.3	Macroscale modeling	21
1.4	Physical mechanisms	21
1.4.1	Contribution of the polymer	22
1.4.2	Polymer chain structure near surface of filler	23
1.4.3	Filler structure	24
1.4.4	Interface: percolation network	24
1.5	Motivations and objectives of the present work	25
1.6	Appendix: Rheology and viscoelasticity	26

In this chapter, we present a rapid overview of nanocomposites. We first describe what fillers are and how they may be dispersed. Next, some typical experimental results are summarized, both the linear and non-linear regimes. Modelling approaches ranging from atomistic simulations to hydrodynamic theory have been used for polymers, they are briefly presented. Finally, we explain the various mechanisms that have been put forward to rationalize the rheology of nanocomposites.

1.1 Polymer nanocomposites (PNCs)

Composites are materials which consist of two or more components and the combination has better properties than any single component considered alone. For instance, polymer composites consist of filler particles within a polymer matrix and the hybrid system provides improved properties compared with the pure polymer matrix. The polymer matrix can be a polymer melt or a rubber-like material. The former material is polymer liquid above its glass and/or crystallization temperature and the latter can be natural rubber, without any extraction process, or an elastomer, which has rubber-like elasticity due to the cross-links between polymer chains. Polymer composites can undergo a large deformation and display a good energy dissipation owing to the enhanced elasticity.

Contrary to traditional polymer composites, in which the filler has much larger size than nanoscale particles, polymer nanocomposites contain nanoparticles as filler, that leads to an increased polymer-filler interaction surface. For instance, the nano-scale filler can provide a small mean particle-particle distance and increase the interfacial area as compared to macro-scale filler. Thus the macroscopic properties can be enhanced [15, 16].

1.1.1 Applications of PNCs

Owing to their outstanding mechanical properties, the polymer nanocomposites have been developed since the 1940s with a specific focus on rubber tires. In the following decades, new fillers have been developed, such as carbon nanotube, graphite or C_{60} , and a great number of polymer nanocomposites combinations has been discovered. Hence the polymer nanocomposites have been employed in a wide range of domains owing to their various properties. First, the tire industries continue developing new generation of productions based on the exceptional mechanical properties of polymer nanocomposites. For instance, the MICHELIN "Green X" tires offer an excellent performance with high wear resistance, outstanding grip on wet roads and reduced fuel consumption. The polymer nanocomposites can also be useful for electronics and automobile applications, such as the electrical insulation and capacitors, for their unique combination with dielectric properties. Moreover, polymer nanocomposites may be used as products with low flammability owing to their flame retardancy and limited gas permeation [17, 18, 19].

1.1.2 Filler type

The filler in polymer nanocomposites can be of various types, for instance, carbon black, silica, C_{60} , clay, carbon nanotubes, graphite, nanorods or organic nanofillers. The fillers can have different shapes, such as spherical, rods, plate or group of primary particles, such as agglomerate or aggregate [19, 16]. The interface between the nanoparticles and the polymer matrix may play a critical role in the dispersion state, chain dynamics and many resulting properties of polymer nanocomposites. The controllable polymerization methods, such as atom transfer radical polymerization (ATRP) and reversible addition-fragmentation chain transfer (RAFT), have been employed to attach polymers to nanoparticle surface. Some specific interfaces can also be created by the grafting-to and grafting-from approaches within

is the main component of natural rubber. It has a size comparable to graphite basic unit. The polymer coil has a diameter around 50 nm, which is comparable with the size of a primary particle, such as nanoparticles of carbon black or silica, and much smaller than the filler aggregates, with a size ranging from 100 to 200 nm. The filler agglomerate is much bigger with size reaching 10 μm [3]. The length scales of the different components in a polymer nanocomposites are extremely diverse, ranging from several angstrom (monomer) to micrometer (agglomerate).

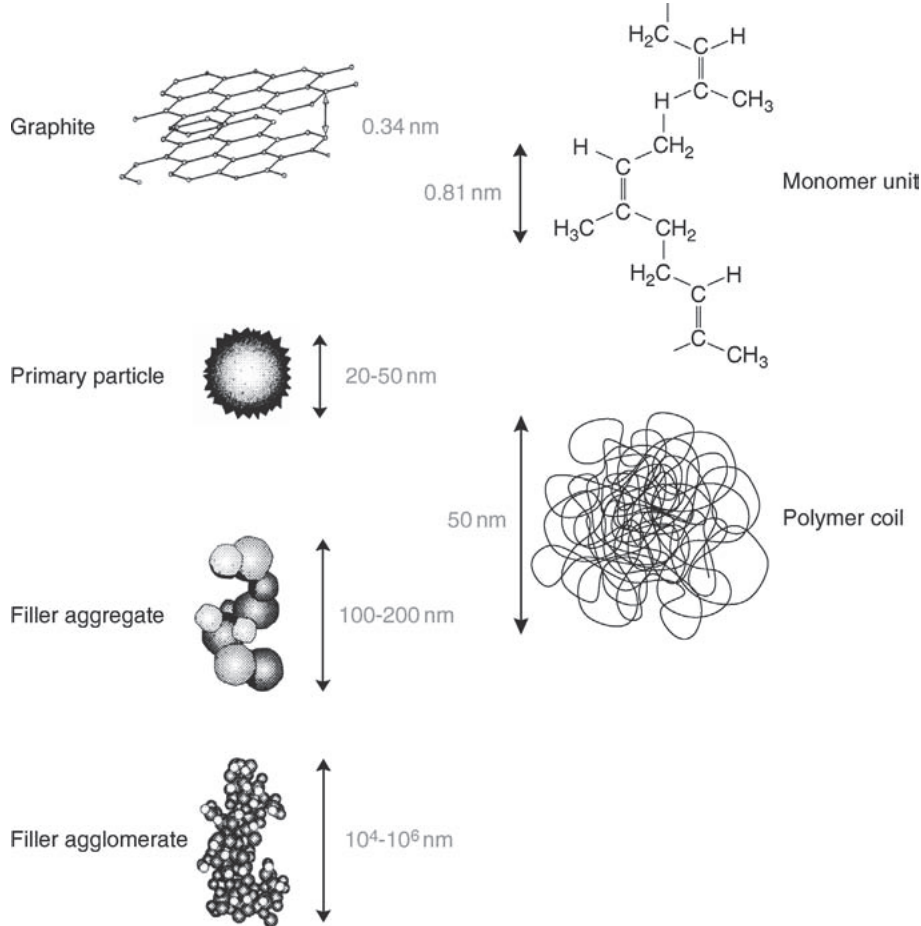


Figure 1.2: Schematic of the length scales of the different components of polymer nanocomposites [3].

1.1.3 Aggregates

The aggregates consist of primary filler particles which are linked via chemical or physical interactions, and they are usually recognized to be unbreakable under deformation [21]. They display a porous and fractal-like structure [22]. If aggregates are fractal with fractal dimension d_f , they obey the following relation,

$$V_p \sim N_p \sim d^{d_f}, \quad (1.1)$$

where N_p is the number of primary particles in an aggregate, V_p the volume they occupy and d is the aggregate size, which is usually given by the aggregate radius of gyration. The volume fraction of particle ϕ_p within an aggregate is then [3],

$$\phi_p = \frac{V_p}{(\pi/6) d^3} \sim d^{d_f-3}. \quad (1.2)$$

A typical carbon black aggregate contains from 2 to 100 primary particles, and has a typical radius near 200 to 300 nm [23, 3]. Transmission electron microscopical pictures of carbon black aggregates are shown in Fig 1.3. The left picture (Fig 1.3a) illustrates an aggregate composing from spherical carbon black nanoparticles with a distribution of radii from 10 to 30 nm. The sample is deposited without solvent [23]. The right figure (Fig 1.3b) shows a TEM (transmission electron micrographs) of the furnace black within S-SBR¹ composites after removing the unbound polymer. The aggregates here are composed of 50 to 200 carbon black particles [3].

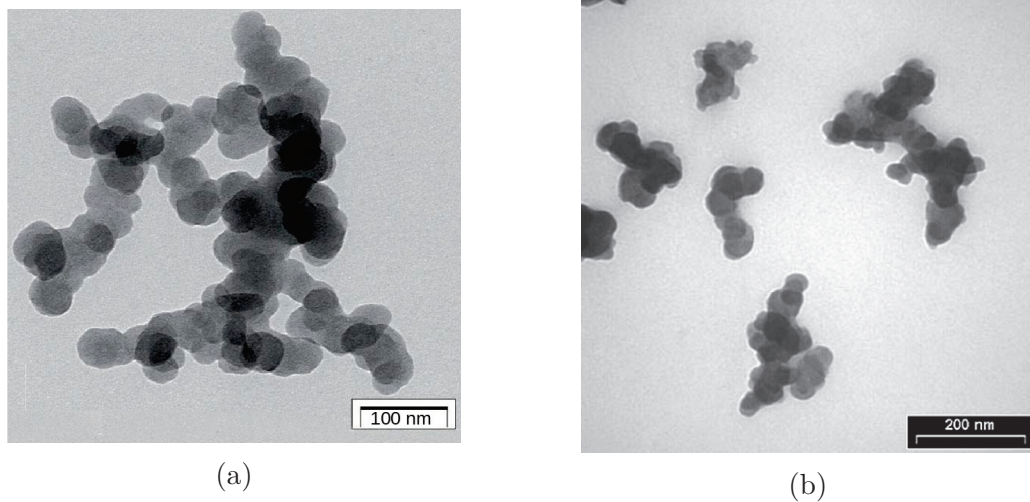


Figure 1.3: TEM pictures of carbon black aggregates [23, 3].

A microscopic view of a nanocomposite is given in Fig 1.4: the polymer nanocomposites consist of silica and SBR, with filler volume fractions 8.4% and 21.1%, where dark grey levels represent the silica particles and the light grey is for SBR polymer matrix. The compounds (a) shows dense aggregates with a diameter near 150 nm and the pure polymer fraction is around 41% in the surface of analysis. In the case of dense silica volume fraction, a large filler structure has been seen and the polymer fraction in the surface of analysis is only about 20% [7].

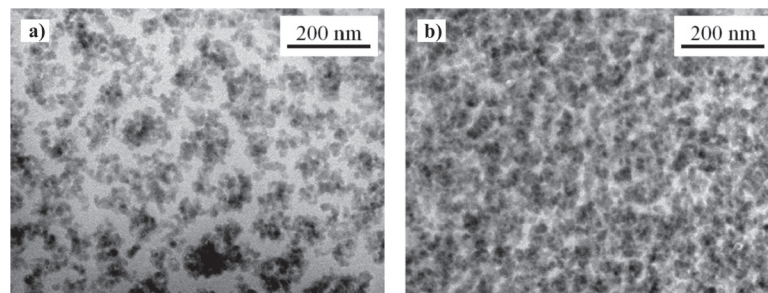


Figure 1.4: TEM pictures of silica-filled SBR nanocomposites, (a) $\Phi_{si} = 8.4\%$ vol. and (b) $\Phi_{si} = 21.1\%$ vol. [7].

The spatial structure of the aggregates may be characterized by small angle X-ray scattering (SAXS) [24]. A SAXS study of silica-filled SBR nanocomposites with a series of silica volume fraction Φ_{si} is shown in Fig 1.5, including the nanocomposites systems represented in Fig 1.4. The scattered intensity $I(q)$ of the monodisperse and spherical silica

¹SBR is the styrene-butadiene rubber from families of synthetic rubbers and S-SBR is the SBR polymerized from solution.

particles can be written as follows:

$$I(q) = \Phi_{si} \Delta \rho^2 V_{si} S(q) P(q), \quad (1.3)$$

where $q = \pi/R$ is the norm of the wave vector, Φ_{si} is the silica volume fraction, $\Delta \rho$ is the density contrast between silica and polymer matrix, $S(q)$ is the total bead-bead structure factor and $P(q)$ is the normalized form factor of the beads. The rupture in slope seen in Fig 1.5 indicates a structure change and is associated to the typical size of particle or structure. The reduced intensity $I(q)/\Phi_{si}$ emphasizes the structure factor $S(q)$ of distinct filler structure, at a fixed $P(q)$. In the left figure, the primary particles can be found at position $q_{si} = \pi/R_{si}$ and the typical sizes of large structures, aggregates and agglomerate (or branch) can be seen at $q_{agg} = \pi/R_{agg}$ and $q_{branch} = \pi/R_{branch}$, respectively. In the right figure at intermediate q and high q regions, the scattered intensity decreases with increasing silica volume fraction at intermediate q and the break in slope related to the aggregate size moves to high q , which indicates a small aggregate with a dense filler concentration. Moreover, the aggregates considered here are polydisperse in size and they have a log-normal distribution on the aggregate size, the number of primary particles in a single aggregate. The typical sizes of aggregates or the agglomerates measured here are the average value of system and the mean silica bead-bead distance is reported as $\langle R_{si} \rangle = 8.9$ nm [7].

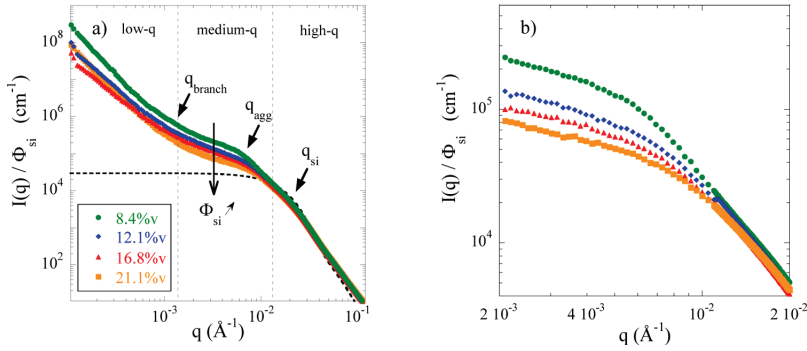


Figure 1.5: SAXS data for silica structure of SBR nanocomposites. (a) Reduced scattered intensity $I(q)/\Phi_{si}$ as a function of silica volume fraction. The dotted line is the form factor of silica beads. (b) Zoom of the figure for intermediate q wave vectors [7].

Compared to bare or grafted single nanoparticles, the aggregates provide a wider structure with an amount of void volume, which leads to a fractal and porous structure, which can trap polymer chains. Owing to their unique capacity for enhancing the mechanical polymer properties, the aggregates are interesting for various industrial applications, such as tires, shoes and reinforced plastics, etc [15].

1.1.4 Miscibility of filler

Miscibility is associated to the dispersion state of nanoparticles in a polymer matrix, which may crucially influence the properties of the composites system. Bare nanoparticles can have a good miscibility if the polymer chain are big enough. However, it is hard to obtain a uniform dispersion of nanoparticles in a polymer matrix [18, 25].

Usually the nanoparticles, except carbon-based fillers, are non-organic while the polymers are organic, thus their different chemical natures can raise an issue of miscibility. A common technique is to graft the polymer chains at the surface of fillers with a chemical nature similar to that of matrix chains [23, 3, 18]. The influence of grafted chains to the miscibility of nanoparticles into a polymer matrix is dependent on the grafted chain density

and the size ratio between grafted chain and chain in matrix. As shown in Fig 1.6, a hybrid system can display four possible structures namely, strings (chains), sheets, amorphous aggregates and dispersed particles [19]. A good dispersion state occurs when the grafted chains are smaller than the chains of the matrix. The large grafted chains length may lead to the anisotropic string and sheet like conformation [26]. If in addition grafted density is low, the amorphous aggregates can also be observed [26, 27].

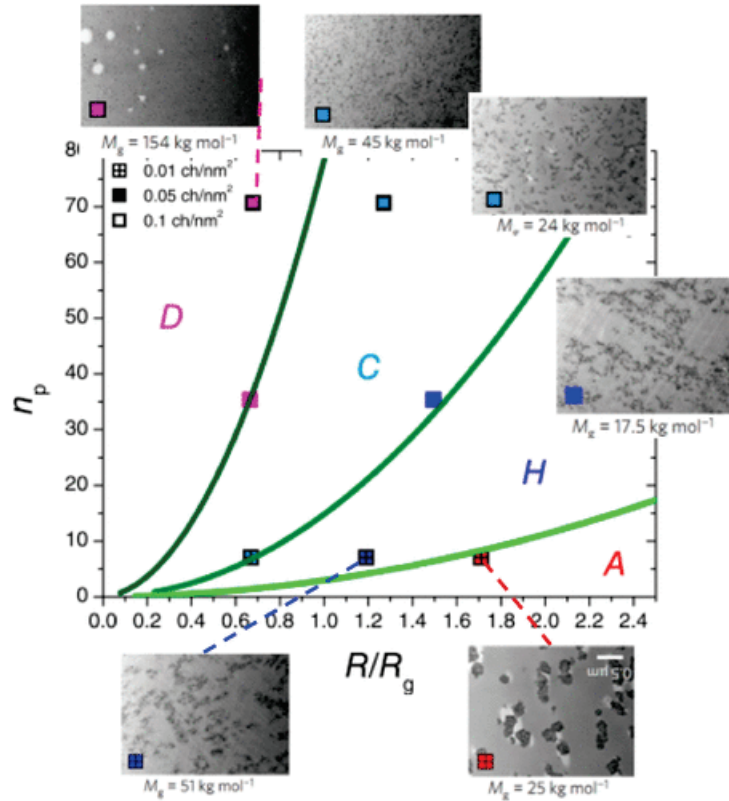


Figure 1.6: Miscibility of nanoparticles in terms of the grafting chain density n_p and the ratio of radius of gyration between grafted chains and matrix chain. The letters A, H, C and D represent the amorphous aggregates, sheets, chains and dispersed nanoparticles, respectively [19, 26].

In the industrial productions, as explained in ref [23], the first step is to breakdown the fillers agglomerate in order to separate the nanoparticles and aggregates from the agglomerate and to disperse the fillers into the polymer matrix. The second step is the breakdown of polymer chains at high temperature and under large extensions, which depends strongly on the chemical nature of the polymer chains and the functional part can be inserted by a specific chemical process. The last step relies on active agents to anchor on the surface of fillers polymer chains formed during the previous step.

1.2 Rheological properties of PNCS

Polymer nanocomposites exhibit different behaviors from the pure polymer matrix both in the linear and the nonlinear regimes. They are addressed in turn below.

1.2.1 Linear rheology

In this regime, the system manifests a linear response, which occurs when the deformation is small, for instance, a small strain amplitude (less than 1%) in an oscillatory shear. The basic quantities are the storage and loss dynamic moduli:

$$G'(\omega) = \omega \int_0^{\infty} G(t') \sin(\omega t') dt', \quad (1.4)$$

$$G''(\omega) = \omega \int_0^{\infty} G(t') \cos(\omega t') dt', \quad (1.5)$$

where ω is the frequency and $G(t)$ is the stress relaxation modulus (see section 1.6 for details).

Liquid/solid transition

In the linear regime, the response is characterized by the dynamic modulus, the storage modulus G' and the loss modulus G'' , which represent the elastic and viscous response of a viscoelastic material. Some background materials on these quantities can be found in section 1.6. When the storage modulus is larger than the loss modulus, the material exhibits a solid-like behavior. Similarly, when the storage modulus is smaller than the loss modulus, the behavior is liquid-like. The intermediate point, where the two dynamic moduli have a close value $G' \simeq G''$, is called the gel point.

As shown in Fig 1.7, in the linear region, both the storage and loss modulus of grafted-silica-filled PS matrix nanocomposites exhibit a frequency dependence. Besides, the filler volume fraction apparently affects the behavior of polymer nanocomposites, especially with a high filler density and large polymer chains. The pure polymer matrix displays a liquid-like behavior even at high shear frequency while the nanocomposites with a weak silica volume fraction, $\phi_{si} = 0.5\%$ to 5% , is dominated by the polymer matrix and manifests a liquid-like behavior in a wide range of frequency. Nonetheless, the dense filled nanocomposites, here with a silica volume fraction $\phi_{si} = 15\%$, displays a solid-to-liquid transition with increasing frequency. The nanocomposites exhibit a solid-like behavior at low frequency while the polymer matrix is dominant at high frequency and a liquid phase can be seen. Even though the polymer chain length may play a relatively minor role as compared to the filler-filler interactions or the polymer-filler interactions, we can observe reinforcement on the magnitude of both dynamic modulus and the gel point moves towards low frequency with long polymer chains.

Reinforcement

The storage and the loss moduli of a pure polymer exhibit the power laws behavior in the low frequency limit: $G'(\omega \rightarrow 0) \sim \omega^2$ and $G''(\omega \rightarrow 0) \sim \omega^1$. Some dilute filled polymer nanocomposites can display similar behavior, which indicates the dominant role of the polymer matrix.

The reinforcement factor R is defined from the ratio between the storage modulus and that of the unfilled system

$$R = \frac{G'(\phi)}{G'(\phi = 0)} - 1, \quad (1.6)$$

where ϕ is the volume fraction of filler. In the dilute regime, the filled polymer matrix carries a weak filler volume or mass fraction, which leads to polymer matrix dominant liquid-like behaviors and may be described by hydrodynamic regime. The reinforcement for such a dilute hybrid system manifests a linear dependence on the filler volume fraction, as expressed by the Einstein-Smallwood equation [29]:

$$R = 2.5\phi, \quad (1.7)$$

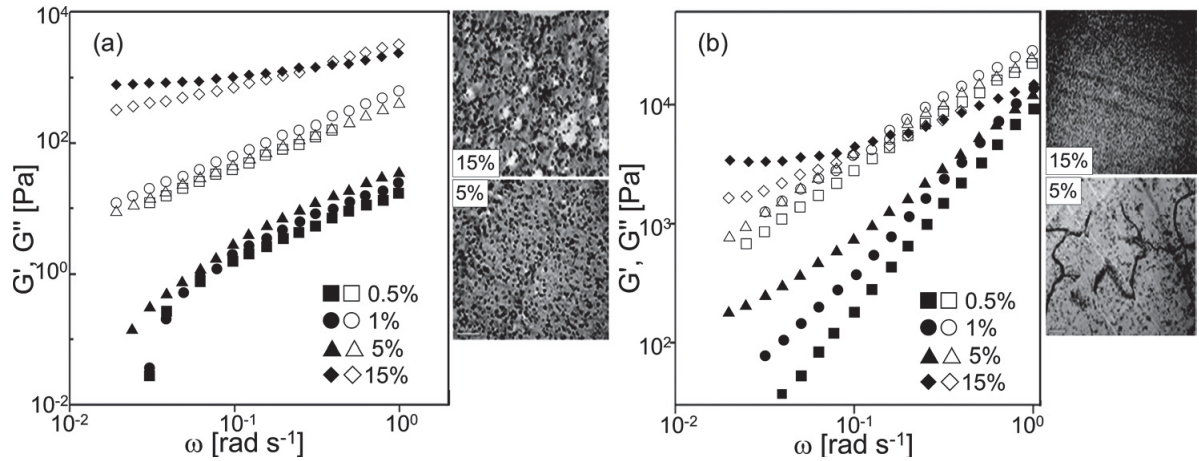


Figure 1.7: Storage (G' , solid symbols) and loss (G'' , hollow symbols) modulus of PS grafted-silica filled PS (a) 44 kg/mol and (b) 150 kg/mol for different volume fractions of filler and the TEM images of samples [28].

Regarding the complicated interaction between elements in a polymer nanocomposites, some additional components should be taken into account, for instance, the filler-filler interaction and the polymer-filler interface, this will be discussed in section 1.4.

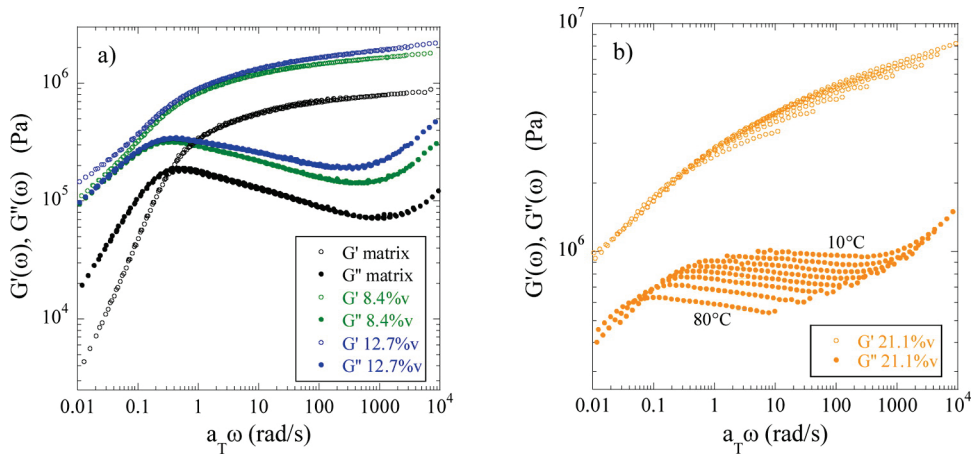


Figure 1.8: Dynamical modulus G' (hollow symbols) and G'' (solid symbols) of silica filled SBR systems as a function of angular frequency ω (a) with a series of silica volume fraction (0%, 8.4% and 12.7%) at a given temperature (50°C) and (b) with a various temperature at a given filler volume fraction 21.1% [7].

The pure and filled SBR polymer nanocomposites at a given temperature manifest a solid-like behavior in a large range of frequency while the filled SBR polymer nanocomposites with a high silica volume fraction presents a clear temperature dependence on the loss modulus, whose magnitude decreases versus increasing temperature, as shown in Fig 1.8(a) and (b). The corresponding reinforcement factors obeys the Einstein-Smallwood equation (Eq 1.7) below the critical volume fraction, after which a percolating structure may be built up and the reinforcement is no longer described by the Einstein-Smallwood power law [7], as shown in Fig 1.9.

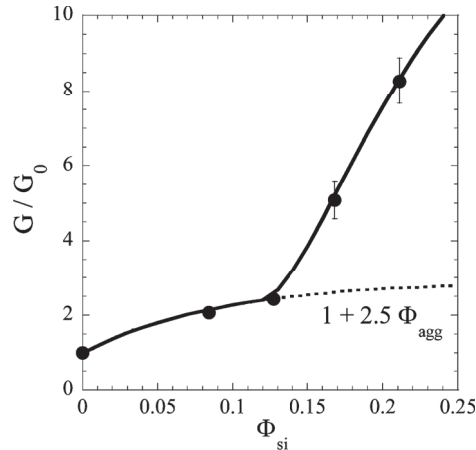


Figure 1.9: Reinforcement factor G'/G'_0 (G/G_0 in the figure) of nanocomposites with filler volume fraction from 8.4% to 21.1%, where G' is the storage modulus at frequency $\omega = 150$ Hz and G'_0 corresponds to that of the polymer matrix. The dashed line represents the Einstein law given by Eq 1.7 [7].

1.2.2 LAOS: large amplitude oscillatory shear

A schematic of the dynamic modulus versus the strain amplitude in an oscillatory shear with a given frequency is illustrated in Fig 1.10. At small strain amplitudes, both the dynamic moduli are independent of the strain amplitude and the shear stress exhibits a sinusoidal form, corresponding to the applied shear deformation. The system is in the linear regime or undergoing SAOS (small amplitude oscillatory shear), as already discussed in previous section 1.2.1. The nonlinear behavior occurs at large strain amplitudes and the shear stress is distorted because of the high order harmonic terms in the stress, then the system is in the nonlinear region or undergoing LAOS (large amplitude oscillatory shear) [30].

The nonlinear behavior of dynamic modulus for different complex fluids can be classified into four classes: strain thinning, strain hardening, weak and strong strain overshoot, as shown in Fig 1.11 [31]. The strain thinning and hardening correspond to a monotonous dependence on strain amplitude, where the dynamic moduli decrease and increase with an increasing strain amplitude, respectively. Most polymer solutions and melts are classified into the strain thinning while PVA/Borax solution can be associated to the strain hardening. The weak strain overshoot corresponds to an overshoot on the loss modulus, for instance, Xanthan gem solution, PEO/PBO diblock copolymer solution, fumed silica suspensions and 5% silica dispersion in mineral oil belong to this class. The last category is the strong strain overshoot where the overshoots occur on both dynamic modulus. Typical examples for this class are the colloidal aggregate gel and 10% silica suspension in PPG [31].

1.2.3 Payne effect

The Payne effect is a well-known nonlinear phenomenon of polymer nanocomposites and it is named after the British rubber scientist A. R. Payne who made extensive studies of the phenomenon. Payne's original paper [32] investigates the nonlinear relationship between the storage modulus and the strain amplitude for a carbon black filler rubber system. As shown in Fig 1.12, the Young's modulus of a MAS carbon filler rubber system exhibits a nonlinear dependence on the strain amplitude while the pure rubber displays a linear behavior over the whole range of deformation. The nonlinearity appears for strain amplitude 1.% and the Young's modulus drops by almost one order of magnitude for high volume fraction. That is the Payne effect, which describes a dependence of the viscoelastic storage modulus on the

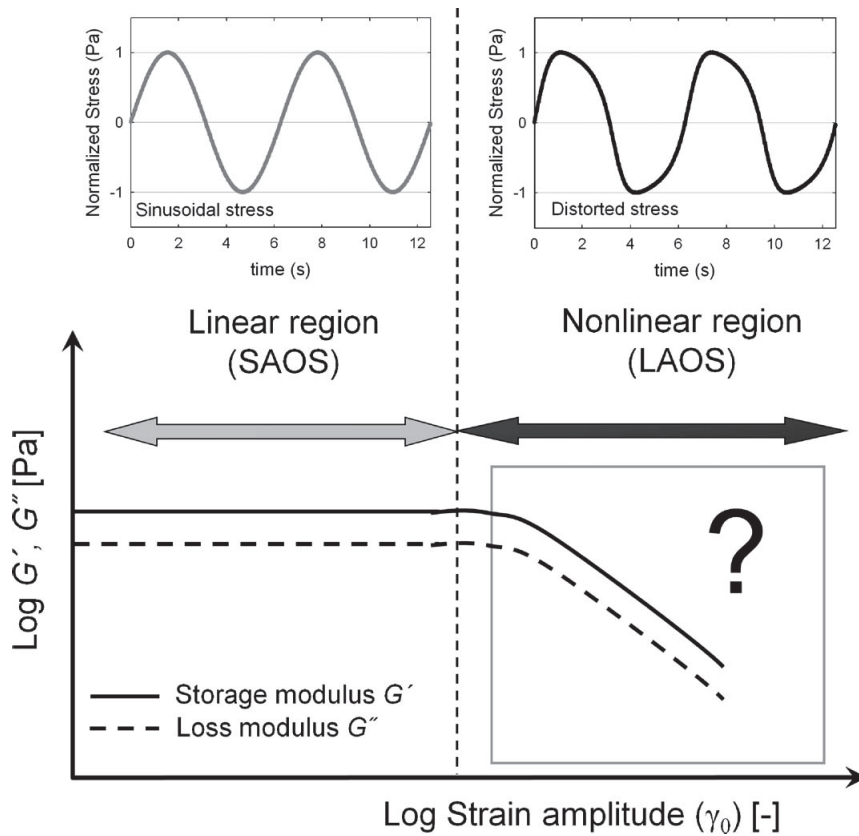


Figure 1.10: Schematic illustration of the strain sweep test at a fixed frequency in order to determine the linear and nonlinear viscoelastic regions [30].

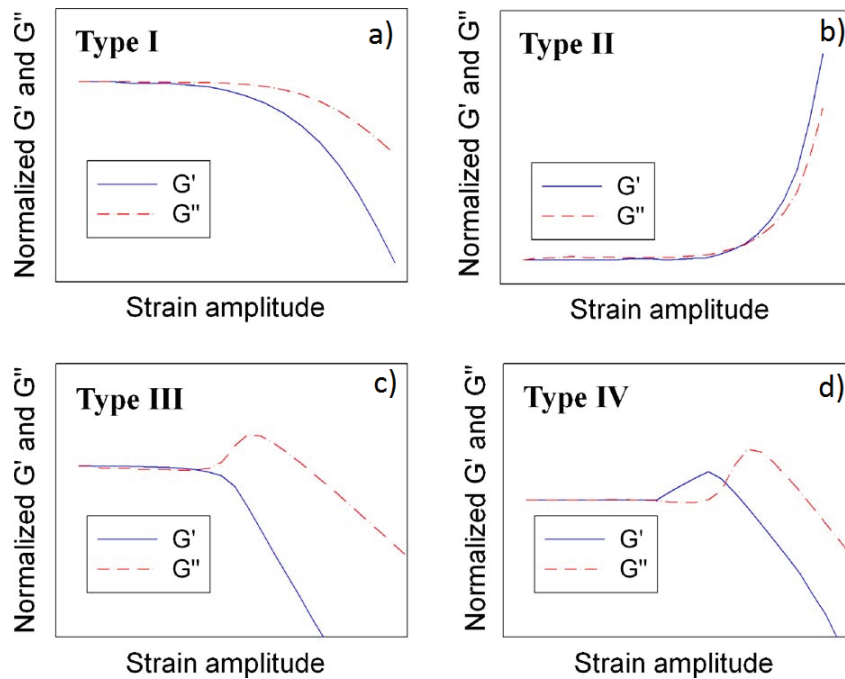


Figure 1.11: Four archetypes of LAOS behavior: (a) strain thinning, (b) strain hardening, (c) weak strain overshoot and (d) strong strain overshoot [31].

imposed strain amplitude.

In the following decades, a large number of studies were devoted to the Payne effect [33,

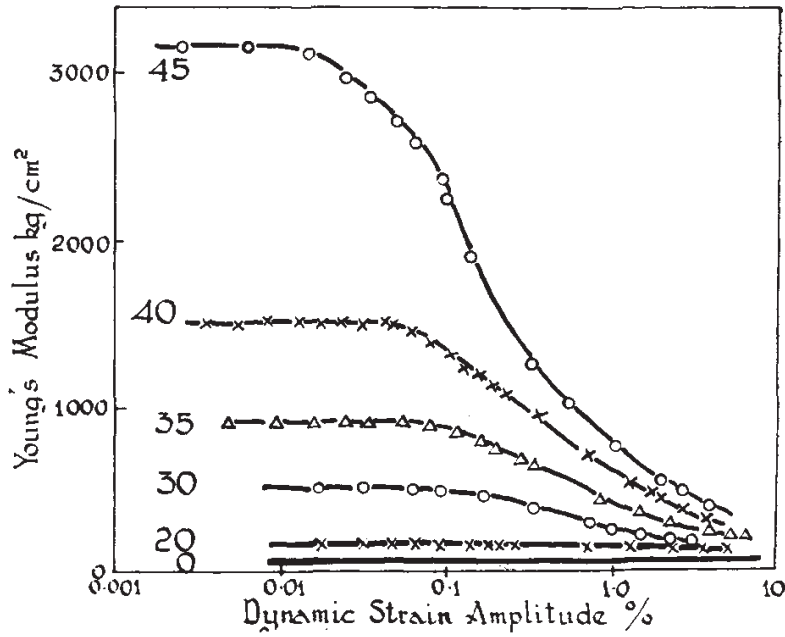


Figure 1.12: Variation of Young's modulus E^* versus the dynamic strain amplitude for a natural rubber vulcanizates containing distinct proportions of MAF black [32]. The numbers along the curves are the volume fractions of filler.

34, 35, 36, 37]. The Payne effect affects not only the storage modulus G' but also the loss modulus G'' , as shown in Fig 1.13, where both the dynamic modulus of a carbon black filled S-SBR compounds show a reinforcement increasing with the filler loading. The storage modulus G' shows a monotonous decrease with increasing strain amplitude while the loss modulus G'' presents clearly an overshoot when the filler loading is important. This is associated to the type III (weak strain overshoot) of Fig 1.11.

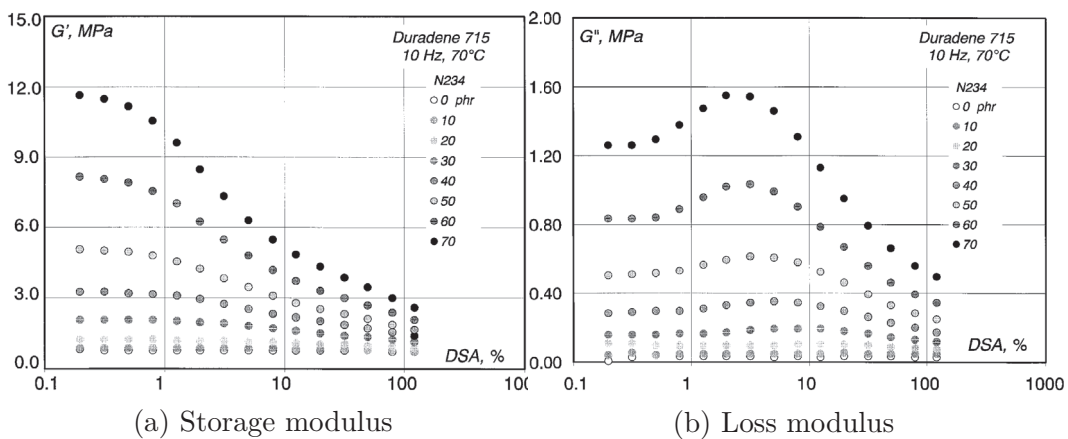


Figure 1.13: Storage (a) and loss (b) modulus as a function of strain amplitude for carbon black filled S-SBR compounds with different filler loadings [38].

1.2.4 Mullins effect

Stress softening is also an important nonlinear effect for both filled and unfilled rubbery systems, which is usually referred to as the Mullins effect [39, 3]. The stress softening occurs

with a cyclic shear at a given strain amplitude, where the shear stress follows distinct stress-strain curves in the stationary state and in the transient state. Whenever the stress-strain cycle exhibits an apparently reduced hysteresis and a stress amplitude at stationary state reduced to that at transient state, this is referred to as stress softening or the Mullins effect. As shown in Fig 1.14, a carbon black filled SBR system has been undergoing a uniaxial deformation and a uniaxial cyclic deformation (5 cycles at each fixed strain amplitude) versus an increasing strain amplitude. At a given strain amplitude, the stress-strain cycles shrink apart from the very first cycle, which can be called the stress softening. Even by increasing the strain amplitude, the stress can no longer reach the same magnitude from the initial state at a given strain, which indicates an irreversible structure change has happened during the cyclic shear.

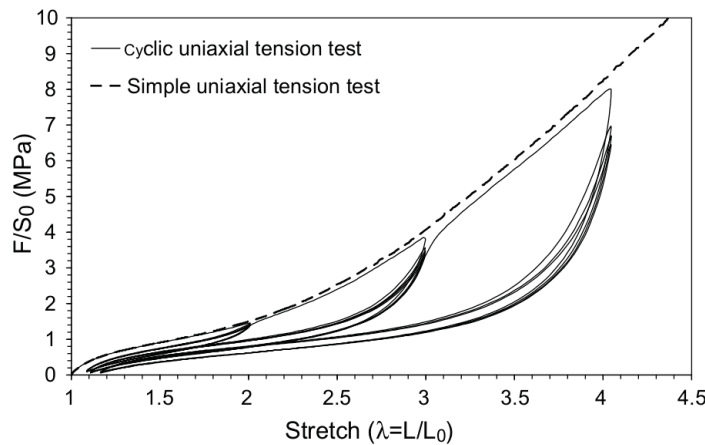


Figure 1.14: Stress-strain response for a carbon black filled SBR submitted to a simple uniaxial tension (dashed lines) and to a cyclic uniaxial tension (solid lines) with increasing strain amplitude, 5 cycles at each fixed strain amplitude [39].

1.2.5 Start up steady deformation

The time evolution of the shear stress in a start-up steady shear is shown in Fig 1.15, where the system are silica filled polymer matrix with a series of mass fraction from 0% (unfilled) to 15% and two polymer matrix already given in the legend. The start-up steady shear occurs at a given shear rate 0.1 s^{-1} . The stress exhibits an overshoot even with a small filler loading and it is generally considered to be related to the breakdown of the filler cluster, formed by aggregates or agglomeration of filler particles, and the morphology change when the system is forced to explore new stationary conformations by shear deformation [28].

1.3 Modeling methods

As shown in Fig 1.16, to model the properties of materials, one needs to distinguish the macro-, meso- and micro-scale structure. Modeling methods are developed corresponding to different length scales, from continuum mechanics to discrete molecular dynamics or quantum mechanics, with decreasing time scale [25]. Multi-scale modeling is essentially difficult because the physical hypothesis in modeling strategies within distinct length/time scale are rarely identical. For instance, it is impossible to simulate a macroscale material or estimate its relative macroscopic properties via a microscale discrete modeling method. Furthermore, the gap between the continuum and the discrete modeling methods requires

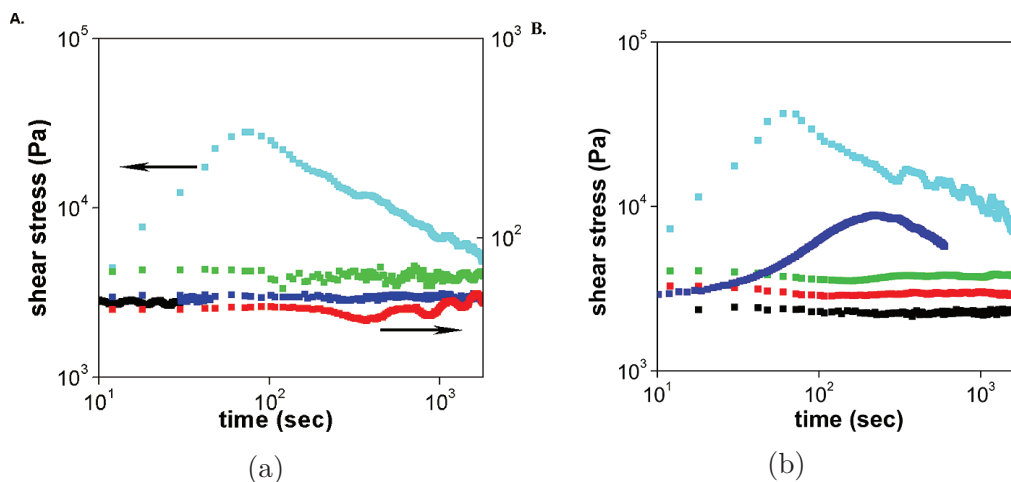


Figure 1.15: Shear stress response during the start-up of steady shear for (a) 44 kg/mol and (b) 150 kg/mol PS composites with 0 (black), 0.5 (red), 1 (green), 5 (blue), and 15 (cyan) in mass fraction with a fixed steady shear rate. The left axis only corresponds to a loading of 15% mass fraction silica while others are plotted on the right hand axis [28].

some physical bridging laws to connect these two kinds of methods, for the sake of completing the "top to bottom" or "bottom to up" algorithm.

1.3.1 Micro-scale modeling

Molecular dynamics

The molecular dynamics is a computation method to simulate and study the classical movement of atoms or molecules. As a recent example is given in the study by Davris [40], where the filler size effect and the filler surface effect have investigated via both the experimental and numerical results. Two models have been issued, the first is a particulate model in which the nanoparticles are surrounded by polymer chains, as shown in Fig 1.17a, and the second one is a simplified model which can reduce the computational resource and in which the polymer chains between nanoparticles are considered as polymer chains layer between two walls, representing filler surfaces, as shown in Fig 1.17b, in which three different values of the film thickness were used in the simulations, which are denoted (from left to right) in this paper as thick, thin, and ultrathin film. The reinforcement by a high filler volume fraction can be exhibited via both methods cited above.

In the molecular dynamics, all phenomenon are taken into account at the microscopic scale and this can provide detailed information of the evolution of the system [41, 42]. However, this induces a problem of scale when system of interest is composed of various elements with different size scale, for instance, a polymer nanocomposites, in which the size of elements varies from microscopic scale to mesoscopic scale. By the conventional molecular dynamics, the simulations are limited to systems with small number of nanoparticles [43, 44].

PRISM

The polymer reference interaction site model (PRISM) is the polymer integral equation theory based on the reference interaction site model and it has been developed to deal with the structure, thermodynamics and phase behavior of polymer nanocomposites melts [45, 46]. Within a polymer nanocomposites system, the PRISM takes into account the polymer-polymer, polymer-nanoparticles and nanoparticles-nanoparticles correlations. The

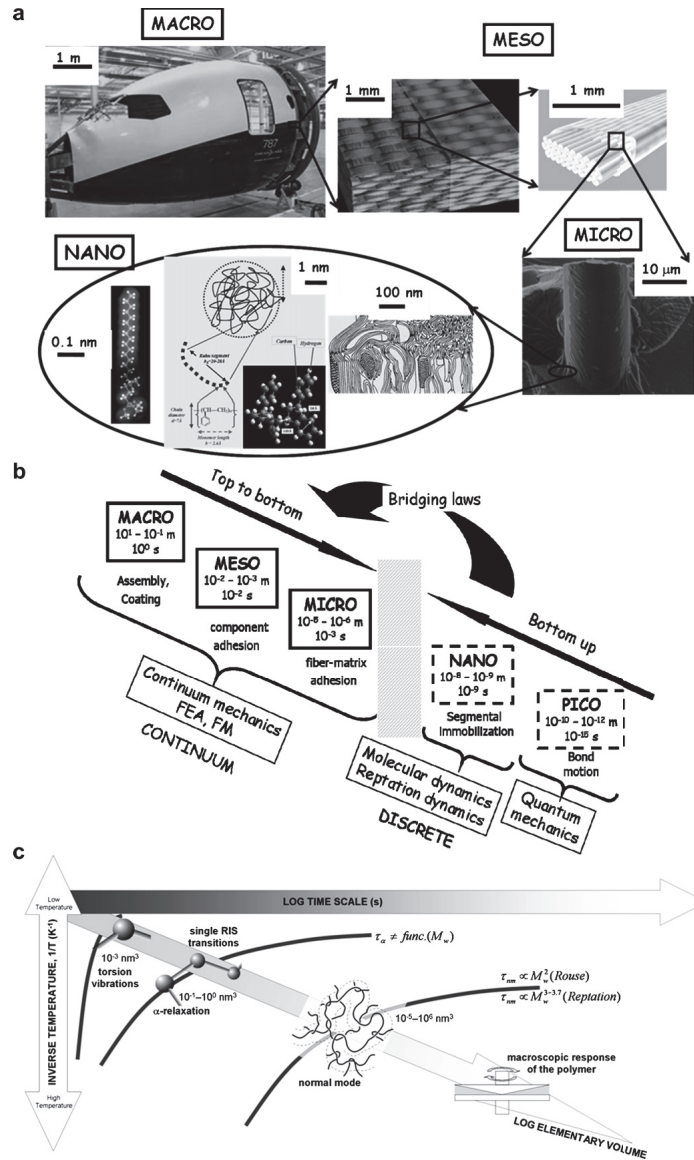


Figure 1.16: Schematic of a nanocomposite structure. (a) A part of airplane represents a large artificial multi-scale composite structure. (b) The top-to-bottom methodology within the continuum mechanics has been employed for engineering the functionality of material. While the gap between the continuum mechanics and discrete mechanics requires physics-based bridging laws to establish the up-bottom and the bottom-up methodology. (c) Relevant polymer relaxation processes as a function of time and temperature [25].

PRISM theory can predict correlation over all length scale within a compressible fluid framework thus it is not a mean field theory. Nonetheless, the PRISM theory can only be employed for spatially homogeneous states.

DFT

The classical density functional theory (DFT) is based on expressing the free energy of a system in terms of single particle density fields [47]. It can predict the density profile of spatially inhomogeneous system, such as fluids near surfaces, and phase transitions between homogeneous and inhomogeneous phases and polymer nanocomposites can be described

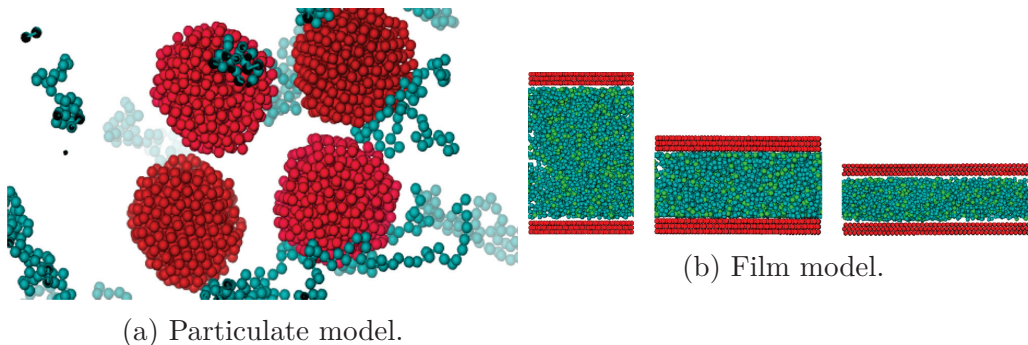


Figure 1.17: Two molecular dynamics simulations for the polymer nanocomposites. (a) Particulate model is a precise method to simulate the exact motion of polymer chains and nanoparticles. The filler beads are shown in red and the polymer chains in green. For clarity, only a fraction of the polymer chains are shown. Four nanoparticles of average diameter about 10 times the diameter of the monomer beads are shown. (b) Film model is a simplified simulation method for dense filled systems [40].

by DFT at one and two particle level. However, the influence of nanoparticles on the bulk polymer-polymer intermolecular correlation, collective scattering structure factors, and phase separation can not be addressed via DFT [46].

Self-consistent mean field theory

The self-consistent mean field theory is a classic approach in polymer physics [48]. It is a powerful tool to simulate block polymer with micro-phase separated on a mesoscopic length scale [46]. However, the intermolecular pair correlation functions are not addressed.

1.3.2 Meso-scale modeling

Slip link model

The slip link model is a powerful model to represent entangled polymers, which inherits the tube model by conserving the topological constraints onto chain motion [49]. The polymer chains are generally described as Rouse chains, in which the Brownian particles are connected by Hookean springs. The entanglements of polymer chains are artificially modeled by slip links [50]. The slip link model is an efficient approach to study the non-equilibrium dynamics of the entanglement of polymer chains and a number of applications of slip link models has been reported in the works [51, 52, 53, 54].

The Likhtman slip link model can reduce a significant computational cost by an order of magnitude compared to molecular dynamics [54]. In Likhtman's model [54], the polymer chains are described as non-interacting Rouse chains which are constrained by additional springs, which represent the topological constraints, known as slip links, as shown in Fig 1.18, where x_j is the location of the ring of one slip link and the fixed anchoring points \vec{a}_j are distributed around the segment position \vec{S}_j with a Boltzmann weight. The ring of the slip links can move along the chain following a straight lines between monomers.

As long as the ring of slip links is not destroyed, the corresponding anchoring points are fixed in space. Thus, the total potential of a single chain can be decomposed into 2 parts,

corresponding to Rouse chain U_{ROUSE} and the slip links U_{SL} :

$$U = U_{ROUSE} + U_{SL}, \quad (1.8)$$

$$U_{ROUSE}(\vec{r}_i) = \frac{3k_B T}{2b^2} \sum_{i=1}^{N_m} (\vec{r}_i - \vec{r}_{i-1})^2, \quad (1.9)$$

$$U_{SL}(\vec{s}_j) = \frac{3k_B T}{2N_s b^2} \sum_{j=1}^Z (\vec{a}_j - \vec{s}_j)^2, \quad (1.10)$$

where N_m is the total number of segments of a polymer chain, b the bond length and Z is the number of slip links per polymer chain.

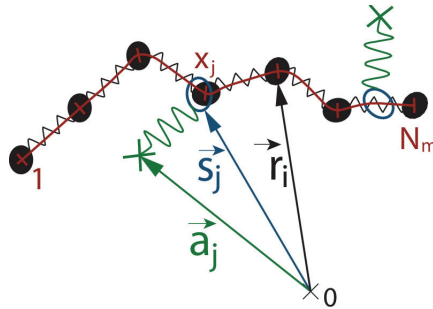


Figure 1.18: Schematic of a Rouse chain with slip links [49].

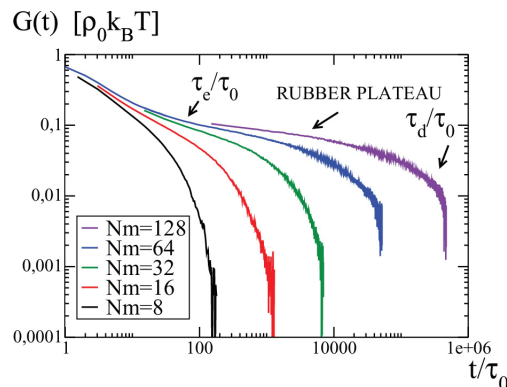


Figure 1.19: Stress relaxation modulus in terms of distinct chain length N_m [49].

In ref [49], the stress relaxation modulus of a slip link polymer model has been computed, as shown in Fig 1.19, where the longer chain length leads to a rubber plateau, which is not observed for short chains. In ref [50], the slip link model has been developed to simulate a filled entangled polymer melt in order to study the reinforcement induced by the effect of the fillers on the entangled network. The polymer chains are described as in [49] while the filler particles are immobile spherical object with or without grafted chains. The grafted chains on the fillers surface are represented by "additional" slip links in the vicinity of fillers. The effect of the grafted chain density on the viscosity of a filled entangled polymer system is shown in Fig 1.20. The bare (non-grafted) fillers follow the Einstein law, as shown in Fig 1.20a, whereas the grafted fillers exhibit a distinct dependence on filler volume fraction from the Einstein law and a reinforcement associated to the number of grafted chains ("additional" slip links), as shown in Fig 1.20b to Fig 1.20d.

Dissipative particle dynamics

The dissipative particle dynamics, developed by Hoogerbrugge and Koelman [55], is a mesoscopic particle-based method and combines features from molecular dynamics and

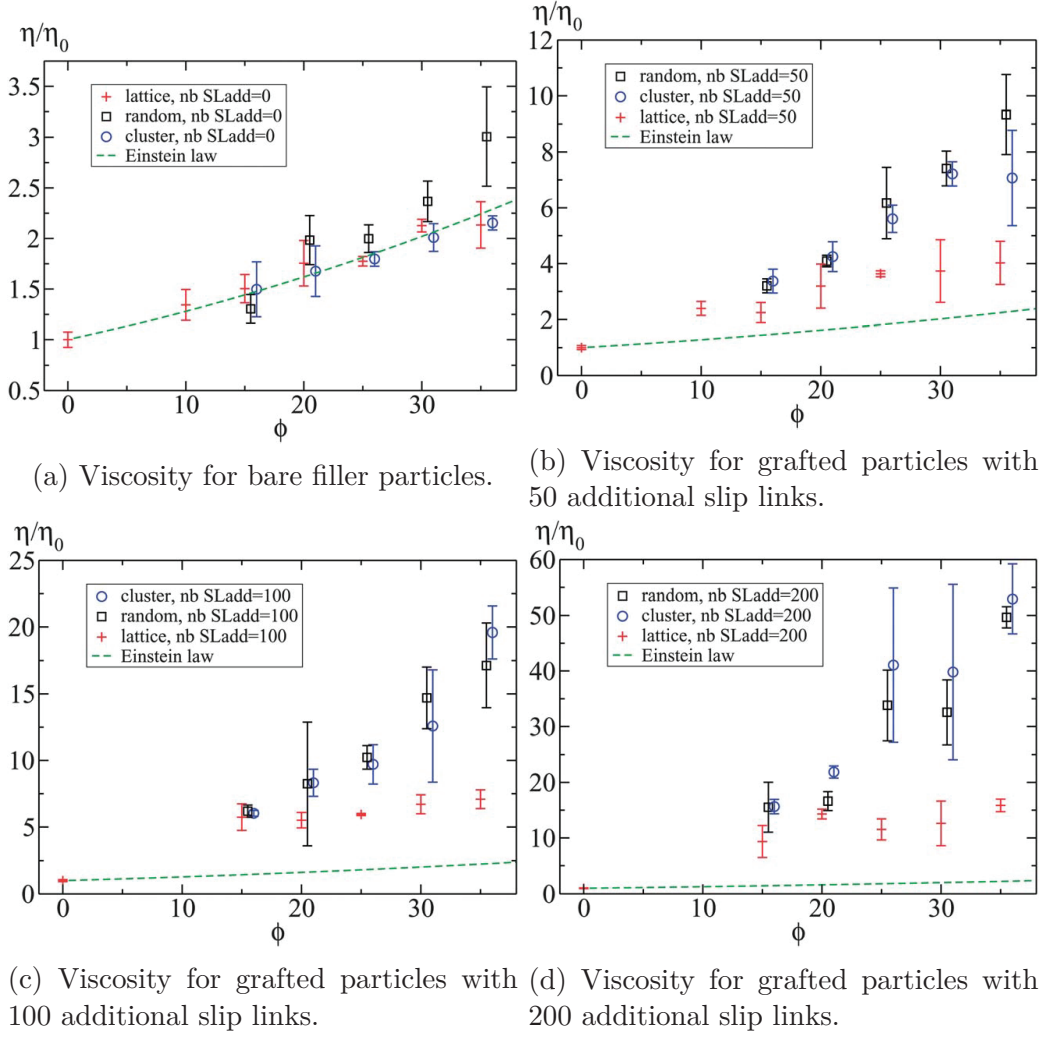


Figure 1.20: Viscosity as a function of the filler volume fraction for bare (a) and grafted (b) (c) (d) fillers distributed on a cubic lattice (red), randomly dispersed (black) and for clusters of three bare particles randomly dispersed (blue). The dashed lines represent the prediction of Einstein law. [50]

lattice-gas automata. In DPD, the forces felt by the particles include three parts:

$$F_i(t) = \sum_{j \neq i} \left(F_{ij}^C + F_{ij}^D + F_{ij}^R \right), \quad (1.11)$$

where F_i is the total force felt by particle i , the first term in the right $F_{ij}^C(r_{ij})$ is the conservative force between a pair of particles i and j and only depends on the corresponding distance r_{ij} , while the second term F_{ij}^D and the third term F_{ij}^R are the dissipative force and the random force, respectively [56].

Nowadays, dissipative particle dynamics (DPD) has been developed into a robust mesoscopic simulation method to study soft matter systems, including polymer solutions, polymer melts and polymer composites. The first unique feature of DPD is to respect the conservation of momentum, along the mass centers of particles/monomers, which is undergoing a potential such as the Lennard-Jones potential [57]. DPD has been developed and employed to study various features of polymers, for instance, the morphology of polymer nanocomposites [57]. As an illustration, the morphologies of filled polymer systems with a high filler volume fraction $\phi = 20\% - 30\%$ are shown in Fig 1.21 by equilibrium and non-equilibrium DPD simulations.

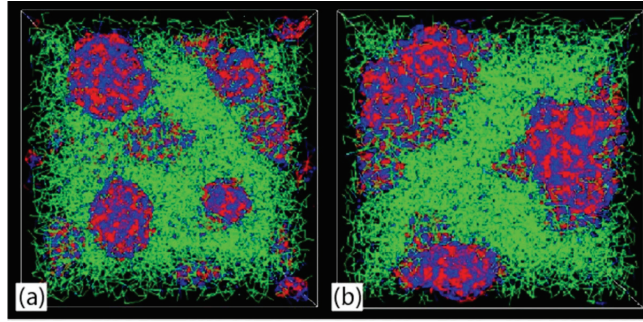


Figure 1.21: Fully dispersed (a) and fully aggregated (b) morphologies of filler particles as investigated in the DPD simulations. The polymer matrix is pictured in green. The particles are pictured in red and blue, corresponding to different types of filler atoms [58, 57].

DPD leads to a reduction of computational cost and increases the simulation performance. Indeed, the time step can be significantly larger than that used in traditional molecular dynamics [57]. Nonetheless, the usual DPD model does not describe a realistic polymer chain behaviors, on the contrary, the chains exhibit as "phantom" chains and they can pass through each other. Thus, quantitative predictions respecting the reptation dynamics can hardly be achieved, notably in a dense entanglement system.

1.3.3 Macroscale modeling

Macroscale approximation

The reinforcement factor can be defined in the following equations, corresponding to the dilute regime where the volume fraction is low,

$$R = \begin{cases} 2.5\phi_f, & \text{(Einstein – Smallwood)} \\ 2.5\phi_f + 14.1\phi_f^2, & \text{(Guth)} \\ [1 + 1.25\phi_f/(1 - 1.35\phi_f)]^2 - 1. & \text{(Eilers)} \end{cases} \quad (1.12)$$

The Einstein-Smallwood formula is suitable to materials with a low volume fraction of filler, so-called "dilute regime", where the reinforcement shows a linear superposition of the individual particles contributions [59]. The Guth's expression takes into account the contribution from the interaction among neighboring particles [60]. The Eilers equation considers the large increase in reinforcement, detected in glassy beads and non-vulcanized filled SBR [40].

However, these relationships only take into account the filler volume fraction of filler, and ignore the other influencing factors, such as the filler surface or the polymer-filler interaction. Therefore, the equation above does not describe a filled SBR rubber system where both the polymer-polymer and the polymer-filler interactions are significantly strong and can not be neglected. The comparison between glass-beads filled PVA (poly(vinyl alcohol)) and nonvulcanized filled SBR (styrene-butadiene rubber) is shown in Fig 1.22. Moreover, the filler volume fraction may not be the only crucial parameter in reinforcement, the filler particles' size and shape may play a role in the composite rheology.

1.4 Physical mechanisms

A general schematic of nanoparticles filled polymer matrix systems is shown in Fig 1.23, where we can distinguish the polymer bulky phase, the filler phase and the interfacial phase.

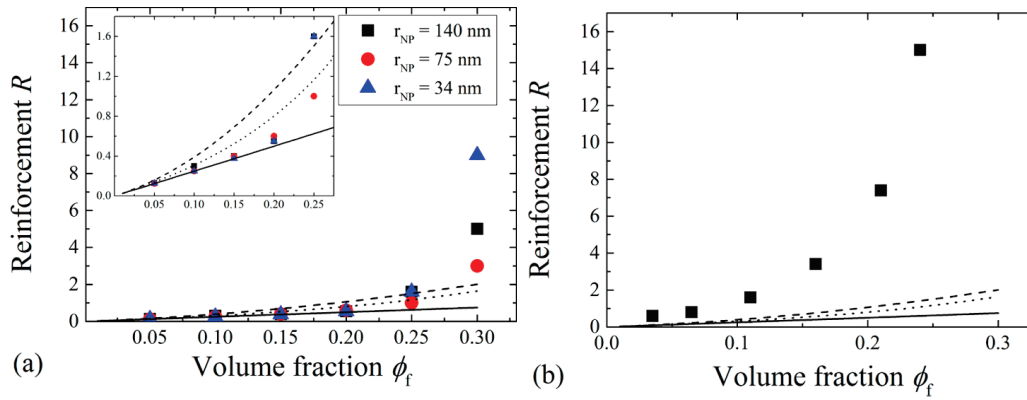


Figure 1.22: Reinforcement versus volume fraction for (a) the model system (PVA filled with glass beads of three different average radii r_{NP}) and (b) the nonvulcanized filled rubber (SBR filled with nanoparticles of precipitated silica), obtained from rheological experiments. The solid, dotted, and dashed lines correspond to the predictions of Einstein-Smallwood, Eilers, and Guth models, respectively [40].

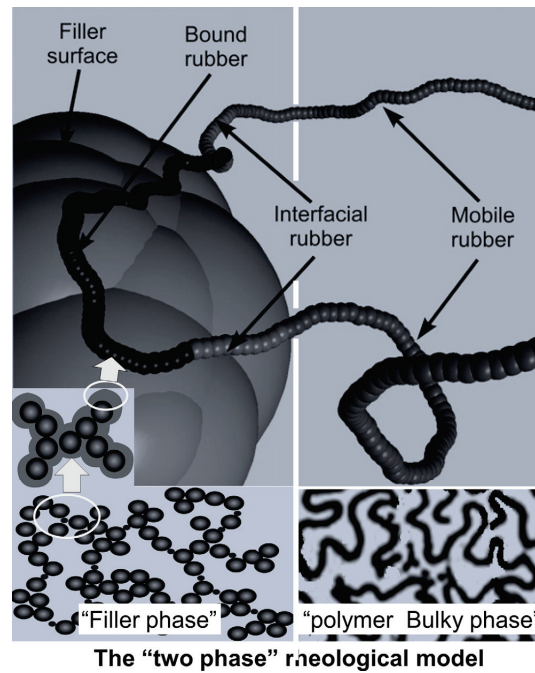


Figure 1.23: Schematic of the "two phase" model for nanoparticles filled polymer composites. The "filler phase" consists of nanoparticles together with their nearby bound segments and interfacial layer with restrained chain mobilities, while the "polymer bulky phase" consists of mobile segments away from the particles [61].

The polymer bulky phase contains the polymer chains far from the fillers and the filler phase is mostly related to aggregates or agglomerates of filler particles, while the interfacial phase is an intermediate region near filler surface where polymer chains are stuck or attached on the filler surface via polymer-filler interactions.

1.4.1 Contribution of the polymer

The chain dynamics can be induced by filler particles near their surface [62, 63, 64], and the nanoparticles can increase or decrease the entanglement density and the disentangle

relaxation time, depending on the nature of their surface (attractive or repulsive interaction). The glass transition temperature may be affected [65]. The polymer matrix is generally thought to play a minor role in reinforcement when compared to the filler or the interface effect.

1.4.2 Polymer chain structure near surface of filler

As illustrated in Fig 1.23, the polymer chains are strongly absorbed on the filler surface and this leads to an inhomogeneous configuration of polymer chain. The chains near filler surface can be classified into 3 kinds: dangling tail (D), absorbed segments/trains (T) and loops (L), where the letters correspond to the chains shown in Fig 1.24a [66]. The dangling tails are the free segments anchored by one side on particles' surface. The absorbed segments are totally running in the interfacial shell of particle. The loops are chains starting and ending in the same particle. As well as the three chains noted, the polymer chain can also connect different particles, a configuration called "bridge". With a high filler concentration, a polymer mediated network can occur owing to the chain absorption and bridging [67]. Furthermore, small fillers can boost the polymer-filler interaction surface rather than large filler particles, at a given filler concentration, and this leads to an enhanced bridging [68] [66], as shown in Fig 1.24b.

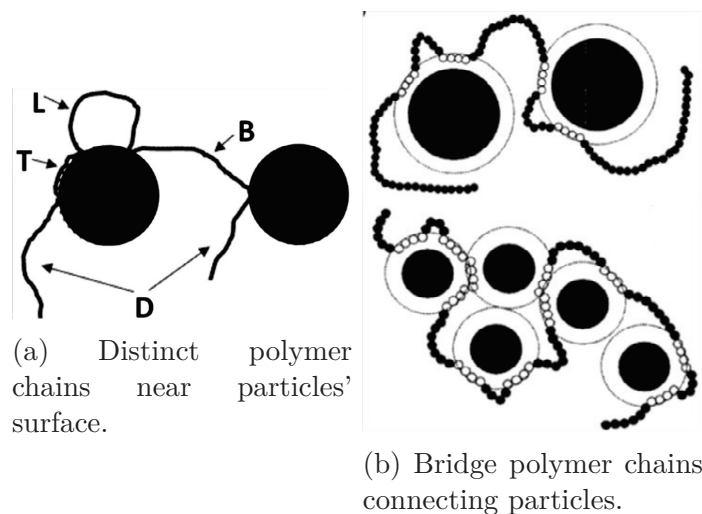


Figure 1.24: Schematic for (a) the polymer chain structure near the surface of filler [69] and (b) the bridge inter-particles [68].

The bound layer is defined as the tense chain conformation surrounding particles surface, which consists of tails, trains and loops. Whether this layer is glassy is still a matter of debate. It has been proposed in [9, 10], but this hypothesis does not always hold: the relaxation time and dynamics can be similar to that of chains far away from particles [11] and the anchored surface layer has been observed to be highly mobile rather than glassy [12, 13]. Thus, the bound layer can be characterized into different fractions and each fraction can exhibit a distinct dynamics from the others. For instance, the immobile interfacial fraction of chains comprising a great part of "trains" and "loops" exhibits a very slow dynamics and diffuse with particles [70]. While the segments in the middle fraction are strongly perturbed by chain-particle interaction, such as absorption. In the outer fraction, the segments/chains can diffuse with a dynamics almost similar to free chains [66].

1.4.3 Filler structure

The filler structure in polymer matrix can influence the rheology of the whole system. With a high filler concentration, the filler and their bound layer combining the bridge chains can participate in the formation of a percolation network, which induces the solid-like behavior of system [18, 71] and exhibits significant reinforcement.

The size of the agglomerate of filler particles can be reduced by imposing strain, as shown in Fig 1.25. This leads to release the trapped polymer chains (or rubber noted in the figure) and increase the polymer-particles interaction surface. Thus, it is generally considered that the breakdown of filler structure, for instance, the agglomerate or the aggregation of particles, under a strain is responsible of the nonlinear behavior of polymer nanocomposites.

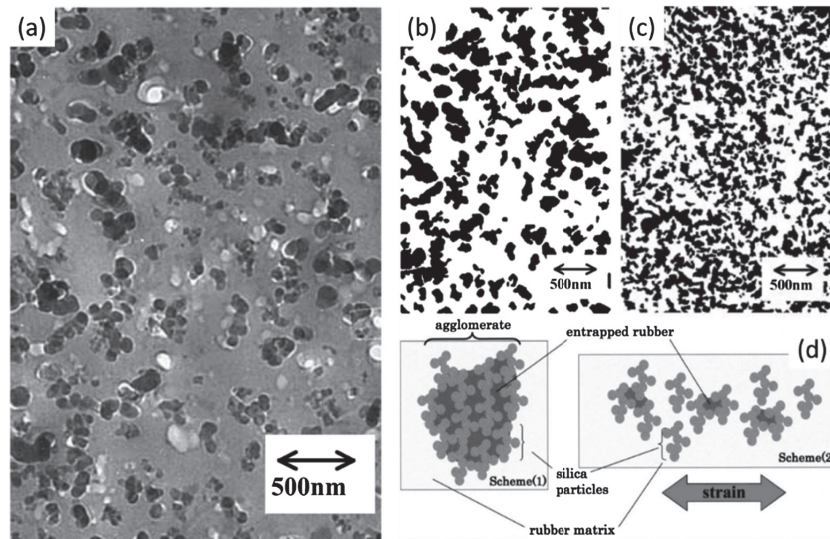


Figure 1.25: (a) TEM images of silica/SBR vulcanizate, TEM digital binary images of the vulcanizate at (b) zero and (c) 50% strains, and (d) schematic representation of the breakdown of agglomerates upon straining (Scheme 1: non stretched, Scheme 2: stretched) [72].

The breakdown of filler network is widely recognized to be the major cause of the Payne effect [3], as shown in Fig 1.26. In a polymer nanocomposite, the filler can form a global structure by the bridging, polymer-filler or filler-filler interaction, for instance, the aggregation and the agglomerate of filler. In the linear region, the filler network generally can provide a large contribution in the storage modulus. The nonlinear region, the breakdown of filler cluster can occur and it leads to the reduction on the storage modulus which indicates the weakening elasticity of the hybrid system.

1.4.4 Interface: percolation network

The polymer-filler interaction is considered a major cause of reinforcement of a polymer nanocomposites [73] and for enhanced hydrodynamic effect [74, 75]. As aforementioned, the nanoparticles can induce local entanglement and create an interphase zone where both the polymer chain mobility and the polymer chain structure are significantly altered [71]. This leads to a percolation network. Furthermore, the grafted chain can be treated as effective slip links around nanoparticles and consequently, the highly packed chain conformation in the vicinity of nanoparticles can be responsible for the enhanced viscosity versus increasing volume fraction of filler [76].

The Mullins effect is often ascribed to non-reversible changes of polymer-filler interface. They are the bond rupture, the molecules slipping, the filler rupture and the disentanglement

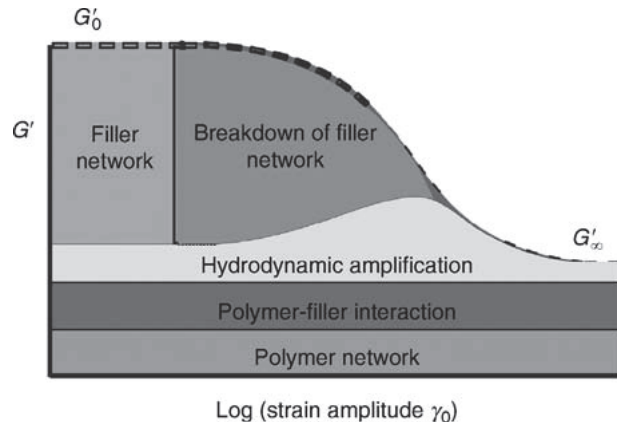


Figure 1.26: Schematic of the different contributions of the Payne effect of a polymer nanocomposites [3].

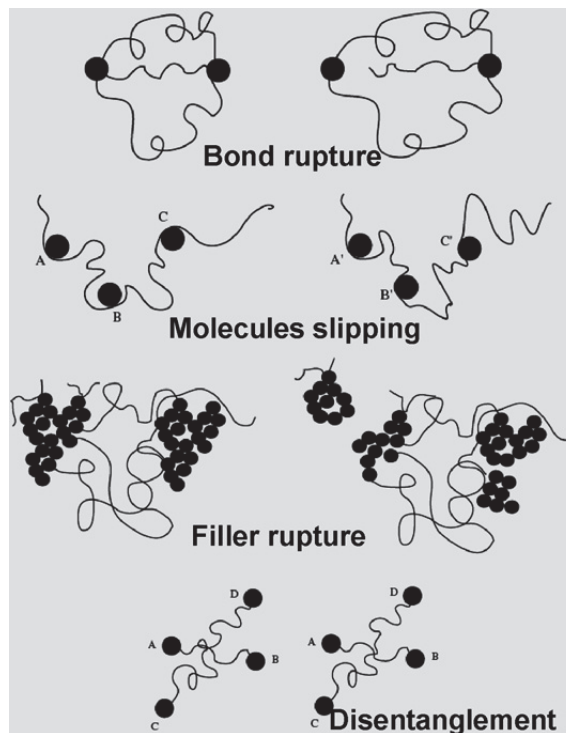


Figure 1.27: Schematic of physical explanations of the Mullins effect [25].

of chains, as shown in Fig 1.27. The bond rupture leads to break liaisons between polymer chains and the filler surface, and it decreases the polymer-filler interaction surface. The molecules slipping may change the anchoring point of a polymer chain on a filler surface and like the chain disentanglements, it may reduce the polymer-filler interactions and the local dynamics of polymer chains. The filler rupture represents the breakdown of the large filler structure which is the same in the Payne effect.

1.5 Motivations and objectives of the present work

Polymer nanocomposites systems have been studied in the past decades owing to their remarkable mechanical properties, including reinforcement and dissipation, which makes them valuable as compared to pure polymer matrix. Their phenomenology is rich, and

as regards their mechanical properties, they are characterized by reinforcement for moderate volume fractions, and non linear effects-including Payne and Mullins effects, for small deformation levels. Despite decades of investigation, the microscopic origin of these effects remains unclear, and several mechanisms are still highly debated in the literature. Yet, it is clear from the experimental side that the existence and the mesoscopic structure of filler aggregates have a strong effect on the rheological response of the composite systems. Unfortunately, describing these mesoscopic length scales using an atomistic simulation seems completely out of reach, given the disparity of length scales ranging from the polymer Kuhn length to the aggregate or agglomerate size.

The objective of this work is therefore to build a mesoscopic model to simulate and analyze the rheological response of polymer nanocomposite. In experiment, the filler morphology, including the existence of aggregates, or the agglomerates of filler are considered to be the major cause of reinforcement and the Payne effect. Here, we intend to build a model apt to simulate a polymer nanocomposite containing filler aggregates. To reach this goal, we build a coarse-grained description, where we concentrate on the filler degrees of freedom, and we "average out" the polymer chains dynamics through the consideration of a velocity kernel in a generalized Langevin equation. This latter kernel is constructed so as to account for the viscoelasticity of the polymer melt surrounding the fillers (this will be explained in chapter 2).

The model here permits to tackle mesoscopic length scales, and describe the dynamics of an assembly of small non-compact aggregates, surrounded by either unentangled or an entangled polymer matrix. With this model, we have systematically measured the rheological response of the model composites, in the linear and non-linear regime of deformation. One of the advantage of this coarse-grained model is to relate systematically the state and configuration of the aggregate to the global stress response of the composite.

1.6 Appendix: Rheology and viscoelasticity

Stress and strain

The stress σ is defined as the ratio between the force F and the cross-sectional area A

$$\sigma = \frac{F}{A}. \quad (1.13)$$

The unit of stress is N m^{-2} or Pa, same as pressure. As shown in Fig 1.28a, the shear strain is associated to the deformation of the top plate Δx relative to the thickness of the sample h ,

$$\gamma = \frac{\Delta x}{h}. \quad (1.14)$$

The stress relaxation modulus $G(t)$ can be written as follows:

$$G = \frac{\sigma}{\gamma}, \quad (1.15)$$

where γ is the applied strain [77, 78].

A step strain is deformation applied instantaneously and maintained constant afterwards

$$\gamma(t) = \gamma\Theta(t), \quad (1.16)$$

where Θ is a Heaviside step function, where $\Theta(t > 0) = 1$ and $\Theta(t \leq 0) = 0$. If a step strain with a magnitude γ is imposed on an elastic and solid material, the stress σ follow the Hooke's law,

$$\sigma = E\gamma, \quad (1.17)$$

where E is the elastic modulus.

A steady shear constantly deform the material with a fixed shear rate, as shown in Fig 1.28b, where the material is set between two plates, the top plate moves towards x direction while the bottom plate is immobile. If the material is purely viscous, the shear stress undergo the Newton's law:

$$\sigma = \eta \dot{\gamma}, \quad (1.18)$$

where η is the viscosity and $\dot{\gamma}$ is the shear rate. Moreover, the material will exhibit a velocity profile in the shear direction (x direction) and proportional to the amplitude (y direction) and the shear rate ($\dot{\gamma}$).

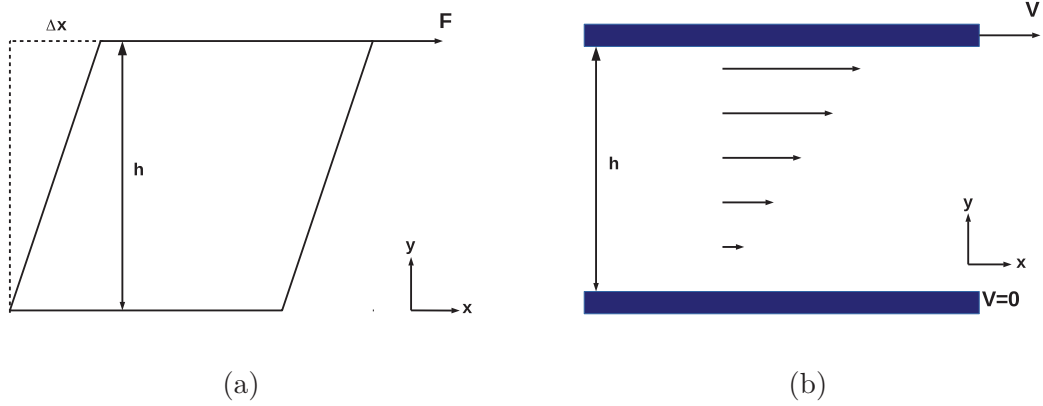


Figure 1.28: (a) Step strain. (b) Steady shear strain.

Maxwell model

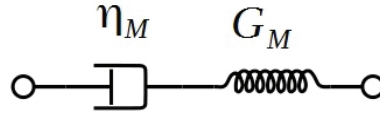


Figure 1.29: Maxwell model of viscoelastic material.

The Maxwell model is a simple illustration of viscoelastic material, which is constituted by an elastic part and a viscous part, as shown in Fig 1.29, such as the polymers. The total shear strain γ accumulates the contributions from both the elastic and the viscous parts,

$$\gamma = \gamma_e + \gamma_v, \quad (1.19)$$

where γ_e and γ_v are the shear strains in the elastic part and the viscous part, respectively. The shear stress σ should be equal at each part

$$\sigma = G_M \gamma_e = \eta_M \dot{\gamma}_v, \quad (1.20)$$

where G_M is the effective modulus and the η_M is the effective viscosity.

Step strain If a viscoelastic material is submitted a step strain, the shear stress $\sigma(t)$ can be time-dependent. Taking into account Eq 1.19 and Eq 1.20, the shear strain can be written as

$$\tau_M \frac{d\gamma_v(t)}{dt} = \gamma - \gamma_v(t), \quad (1.21)$$

where $\tau_M = \eta_M/G_M$ is the Maxwell relaxation time. Hence, the shear strain in the elastic part can be written as

$$\gamma_e(t) = \gamma - \gamma_v(t) = \gamma \cdot \exp(-t/\tau_M). \quad (1.22)$$

This indicates that the Maxwell relaxation time τ_M is the critical time scale to separate two behavior regimes: elastic regime ($t < \tau_M$), corresponding to a solid behavior, and viscous regime ($t > \tau_M$), corresponding to a liquid behavior. Furthermore, the shear stress can be related to $\gamma_e(t)$ as follows:

$$\sigma(t) = G_M \gamma_e(t) = G_M \gamma \cdot \exp(-t/\tau_M). \quad (1.23)$$

Thence, the stress relaxation modulus $G(t)$ decreases exponentially in time

$$G(t) = \frac{\sigma(t)}{\gamma} = G_M \cdot \exp(-t/\tau_M). \quad (1.24)$$

Rheology and strain

Generally, if the applied strain is small enough, the material, including Maxwell material, should be in the linear response regime, where the stress relaxation modulus $G(t)$ is independent of the strain γ and the Boltzmann superposition principle is valid [77]. Then the shear stress $\sigma(t)$ at time t can be history-dependent as a linear combination of the stress of each individual shear step $\delta\gamma_i$ at time t_i ,

$$\sigma(t) = \sum_i G(t - t_i) \delta\gamma_i, \quad (t_i < t), \quad (1.25)$$

where the applied strain $\delta\gamma_i$ at time t_i is independent from the other applied strains apart from time t_i . In the continuum limit, the sum in the shear stress can be replaced by the integration

$$\sigma(t) = \int_{-\infty}^t G(t - t') \dot{\gamma}(t') dt'. \quad (1.26)$$

Steady shear strain

If a viscoelastic material is subject to a steady shear strain with a constant shear rate $\dot{\gamma}$, as shown in Fig 1.28b, the shear stress should be

$$\sigma(t) = \dot{\gamma} \int_{-\infty}^t G(t - t') dt' = \dot{\gamma} \int_0^{\infty} G(t') dt'. \quad (1.27)$$

Thence, the shear viscosity η can be expressed as follows

$$\eta = \frac{\sigma}{\dot{\gamma}} = \int_0^{\infty} G(t') dt'. \quad (1.28)$$

In particular, for the Maxwell model,

$$\eta = G_M \int_0^{\infty} \exp(-t/\tau_M) dt' = G_M \tau_M = \eta_M. \quad (1.29)$$

The effective viscosity η_M is just the shear viscosity η in this case.

Oscillatory shear strain

An oscillatory shear strain follows a sinusoidal signal with a given strain amplitude as $\gamma(t) = \gamma_0 \sin(\omega t)$ with the angular frequency ω . If the material is purely elastic, the shear stress is

$$\sigma(t) = E\gamma_0 \sin(\omega t). \quad (1.30)$$

If the material is purely viscous, the shear stress is

$$\sigma(t) = \eta\gamma_0\omega \cos(\omega t) = \eta\gamma_0\omega \sin(\omega t + \pi/2). \quad (1.31)$$

In the material is viscoelastic, for instance, a Maxwell material, and the strain is small enough to keep the material in the linear region, the shear stress should be proportional to the magnitude σ_0 and a phase angle $\omega t + \delta$ as follows:

$$\sigma(t) = \sigma_0 \sin(\omega t + \delta). \quad (1.32)$$

where δ is the phase shift. Therefore, the shear stress can be decomposed into two orthogonal terms with the same frequency [78],

$$\sigma(t) = \gamma_0 (G'(\omega) \sin(\omega t) + G''(\omega) \cos(\omega t)), \quad (1.33)$$

where $G'(\omega)$ and $G''(\omega)$ are the storage modulus and the loss modulus, respectively. Taking into account Eq 1.32 and Eq 1.33, the storage and the loss moduli can be written as

$$G'(\omega) = \frac{\sigma_0}{\gamma_0} \cos \delta, \quad (1.34)$$

$$G''(\omega) = \frac{\sigma_0}{\gamma_0} \sin \delta. \quad (1.35)$$

In the linear response region, the shear stress can be written in continuum formula with shear rate $\dot{\gamma} = \omega\gamma_0 \cos(\omega t)$,

$$\begin{aligned} \sigma(t) &= \int_{-\infty}^t G(t-t')\omega\gamma_0 \cos(\omega t') dt', \\ &= \omega\gamma_0 \cdot \text{Re} \left[\int_{-\infty}^t G(t-t') \exp(i\omega t') dt' \right], \\ &= \omega\gamma_0 \cdot \text{Re} \left[\exp(i\omega t) \int_{-\infty}^t G(t-t') \exp(-i\omega(t-t')) dt' \right], \\ &= \omega\gamma_0 \cdot \text{Re} \left[\exp(i\omega t) \int_0^{\infty} G(t') \exp(-i\omega t') dt' \right], \\ &= \omega\gamma_0 \cdot \text{Re} \left[(\cos(\omega t) + i \sin(\omega t)) \cdot \int_0^{\infty} (G(t') \cos(\omega t') - iG(t') \sin(\omega t')) dt' \right] \\ &= \omega\gamma_0 \cdot \left[\sin(\omega t) \int_0^{\infty} G(t') \sin(\omega t') dt' + \cos(\omega t) \int_0^{\infty} G(t') \cos(\omega t') dt' \right]. \end{aligned} \quad (1.36)$$

Therefore, the storage modulus $G'(\omega)$ and the loss modulus $G''(\omega)$ can be related to the stress relaxation modulus $G(t)$,

$$G'(\omega) = \omega \int_0^{\infty} G(t') \sin(\omega t') dt', \quad (1.37)$$

$$G''(\omega) = \omega \int_0^{\infty} G(t') \cos(\omega t') dt'. \quad (1.38)$$

The two dynamic modulus can be combined into a complex modulus $G^*(\omega)$,

$$G^*(\omega) = G'(\omega) + iG''(\omega) = i\omega \int_0^{\infty} G(t) \exp(-i\omega t) dt. \quad (1.39)$$

Furthermore, the shear stress can be also written in terms of the complex modulus $G^*(\omega)$

$$\sigma(t) = \gamma_0 \text{Re} [\exp(i\omega t) G^*(\omega) / i]. \quad (1.40)$$

Contents

2.1 Filler types	32
2.1.1 Individual nanoparticles	32
2.1.2 Aggregates	32
2.2 Simulation method	36
2.2.1 Interparticle potential	36
2.2.2 Brownian dynamics	37
2.2.3 Generalized Langevin dynamics (GLE)	38
2.2.4 Application of the GLE to entangled polymer dynamics	41
2.2.5 System units	42
2.2.6 Initial configurations	42

Introduction

The modeling of polymer nanocomposites leads to great challenges because it is a multiscale problem [79, 57]. There is a gap between the size of a monomer and the size of an aggregate. Moreover, a faithful representation of nanocomposites also requires that many aggregates be included, so that structures appearing at a scale larger than a single aggregate, such as a network, can also be described. An explicit, molecular simulation of chains and aggregate is therefore impossible. When the medium surrounding particles is a simple liquid, a traditional approach is to rely on an implicit description of the solvent. Its effect is taken into account with a viscous friction and a noise term, as done in Brownian dynamics. In this chapter, we explain how this approach can be extended to particles in a viscoelastic medium. We rely on a method developed recently in a different context [80].

In contrast with the surrounding medium, the fillers are represented explicitly in our simulation. We are thus free to choose their size, shape and rigidity. We first present the three types of filler that will be considered: the individual nanoparticles, the flexible aggregates and the rigid aggregates. The last type is the most relevant to polymer nanocomposites whereas the two other types provide useful comparison point to interpret the results.

2.1 Filler types

2.1.1 Individual nanoparticles

The individual nanoparticles are supposed to be spherical and solid, and they are not allowed to aggregate between each other by introducing a repulsive interaction potential between nanoparticles. They are referred to the well-dispersed nanoparticles in colloidal suspension. A simple illustration and a snapshot in a corresponding simulation are shown in Fig 2.1.

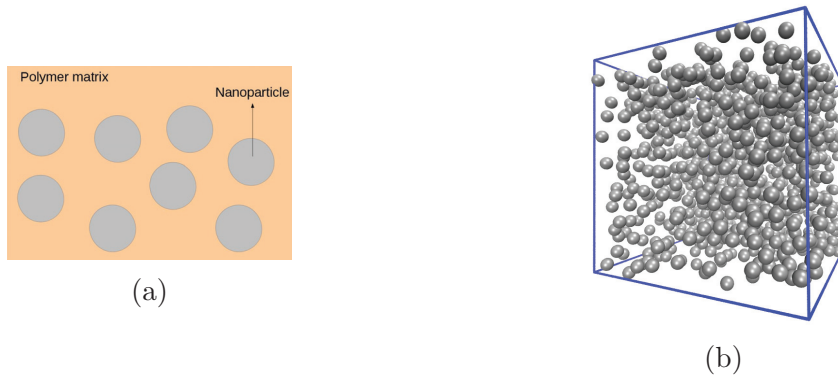


Figure 2.1: (a) 2D schematic of a polymer nanocomposites filled by the individual nanoparticles and (b) a snapshot in a simulation for the model composites filled with the individual nanoparticles.

2.1.2 Aggregates

In our modeling, an aggregate is a group of N_{agg} primary nanoparticles connected by a spring network that ensures the aggregates integrity. In the following, we will consider two kinds of aggregates: flexible and rigid aggregates. The former maintains only the connectivity between neighboring particles and is reminiscent of a star polymer, while the latter is supposed to model undeformable object. Considering these two types of aggregates permit to assess the role of aggregates rigidity in the rheology of the model composites system.

Flexible aggregates

In the flexible aggregates, only the nearest neighbors particles are linked with springs, as shown in Fig 2.2a (which particles are nearest neighbours depends on the structure of the aggregate and will be explained below). The springs used here are linear, with a potential $k(l - l_0)^2/2$, where k is the stiffness coefficient, l are the spring length, l_0 is the equilibrium length. We see the primary particle as spheres of diameter d touching each other, and want to keep constant the distance between neighboring particles. For this reason, the equilibrium length of the spring is chosen so that the short-range interaction force is balanced by spring force. For instance, if the spring stiffness is fixed to $k = 100$ force/length unit, and the short-range repulsive interaction is described by a truncated-shifted Lennard-Jones potential with $\epsilon = 1$ energy unit, one finds that the free length should be set to 0.76 length unit.

Rigid aggregates

In the rigid aggregates, the connectivity network is supplemented with virtual springs, as shown in Fig 2.3a, that are intended to preserve the aggregate geometrical structure.

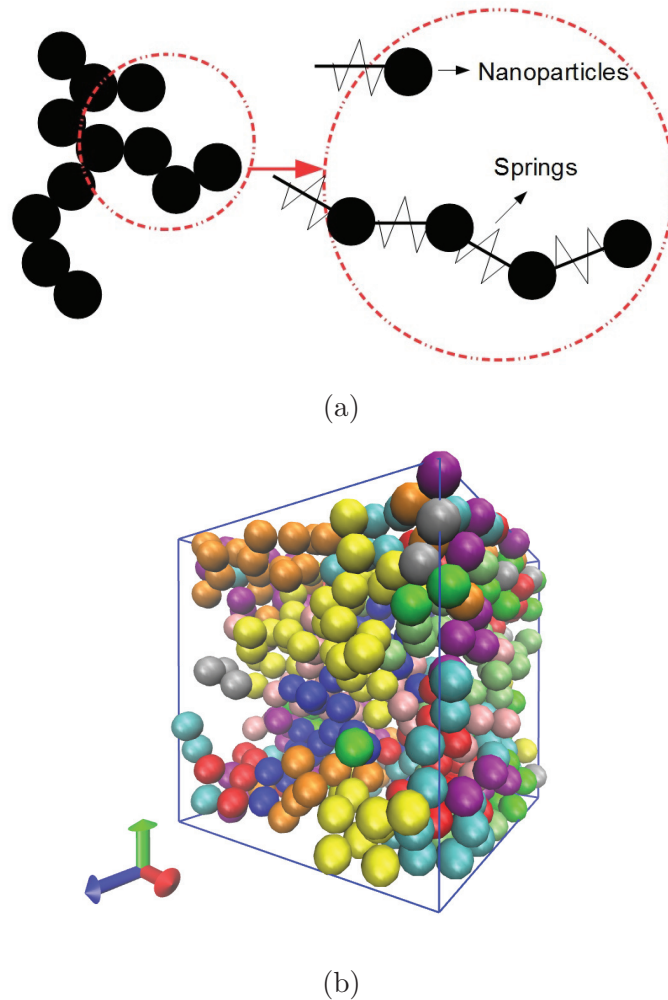


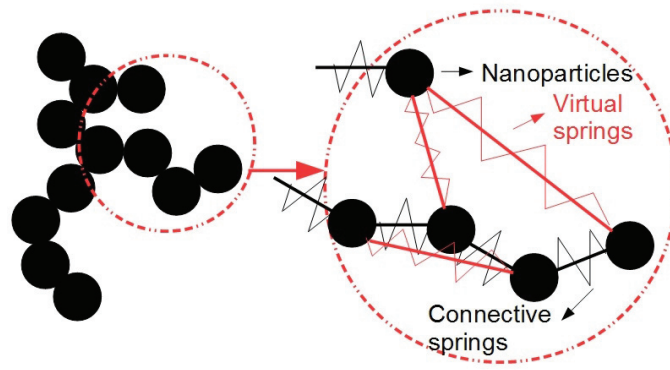
Figure 2.2: (a) 2D schematic of a flexible aggregate. The black lines correspond to the springs and the grey spheres are the primary particles of aggregate. (b) A snapshot in a simulation with monodisperse flexible aggregates.

In our model, each primary particle is linked to three non-neighboring primary particles belonging to the same aggregate, which are chosen at random. The virtual springs have stiffness k and their equilibrium length is the distance between particles for the original structure of the aggregates ¹.

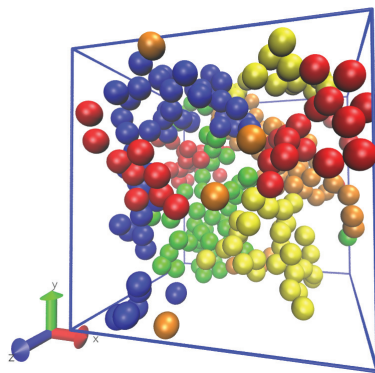
Generation of aggregates

As discussed in section 1.1.3, the aggregates generally have a branching, disordered structure. While others choice could have been possible, we have chosen to consider aggregates generated by the diffusion-limited aggregation (DLA) algorithm [81]. A schematic of this algorithm is shown in Fig 2.4. One nanoparticle is released randomly on the appearance sphere with a radius R_p larger than the minimum bounding sphere of radius R_b , which is the actual size of aggregate. The nanoparticle performs a Brownian motion and may attach the aggregate, which occurs if the distance between the diffusing particle and at least one nanoparticle of the aggregate is smaller than a critical distance taken to be equal to the particle diameter d . The process ends if the particle contacts the aggregate or the particle

¹Very often, the distance between particles linked by a virtual spring is larger than the cut-off in the repulsive interaction. We neglect the small changes in structure that may happen when this is not the case.



(a)



(b)

Figure 2.3: (a) 2D schematic of the rigid aggregate. The black lines are the real springs and the dotted red lines are the virtual springs, the grey spheres are the primary particles. (b) A snapshot in a simulation with monodisperse rigid aggregates.

reached the external boundary sphere of radius R_e . Once a particle has joined the aggregate, the aggregate size of radius R_b and the related parameters, such as the appearance sphere of radius R_p and the external boundary sphere of radius R_e , are updated for the next particle. The process ends when the aggregate reaches the desired size.

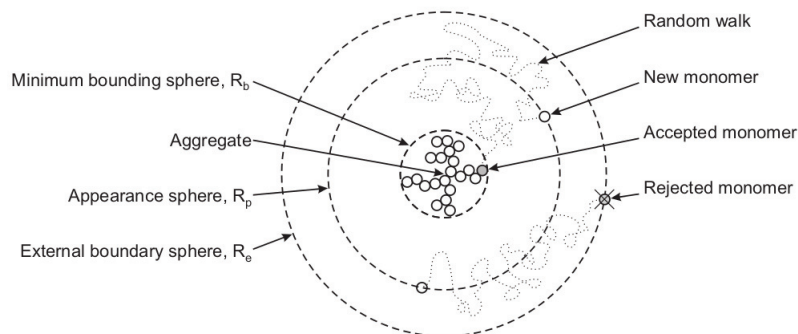


Figure 2.4: 2D schematic of the DLA algorithm.

Size distribution of aggregates

In this work, we have considered either monodisperse or polydisperse aggregates. Monodisperse aggregates are characterized by a unique aggregate size, equal to the number of primary particles N_{agg} contained in an aggregate. Polydisperse aggregates exhibit a distribution of aggregate size $P(N_{agg})$, which follows typically a log-normal distribution. For instance, the aggregate size measured for a silica filled SBR polymer nanocomposites follows a log-normal distribution with silica volume fraction $\phi_{si} = 8.4\%$, as shown in Fig 2.5a, where the most aggregates have a small aggregation number $N_{agg} = 15$ and a relatively large average aggregate size $\langle N_{agg} \rangle = 51$ with the standard deviation $\Delta N_{agg} = 53$, due to a few big aggregates [7].

In practice, we have used the following (gamma) distribution to generate the aggregate size distribution,

$$P(N_{agg}) = AN_{agg}^a \exp\left(-\frac{N_{agg}}{b}\right), \quad (2.1)$$

where $A = 1/(ab^{a+1})$ is a normalization factor, a and b are the free parameters. Then the most frequent aggregate size is $N_{agg,c} = ab$ and the mean aggregate size is $\langle N_{agg} \rangle = (a+1)b$. For example, an aggregate size distribution calculated from Eq 2.1 is shown in Fig 2.5b, with parameters $a = 2$ and $b = 10$, for which the mean aggregate size is $\langle N_{agg} \rangle = 30$ and the most probable aggregate size is $N_{agg,max} = 20$. The aggregate sizes range from $N_{agg} = 1$ to 100, which yields an aggregate size polydispersity $\sigma \simeq 30\%$. For the sake of simplicity of the model, the polydisperse aggregates in this work will be following the size distribution defined from the empirical formula in Eq 2.1.

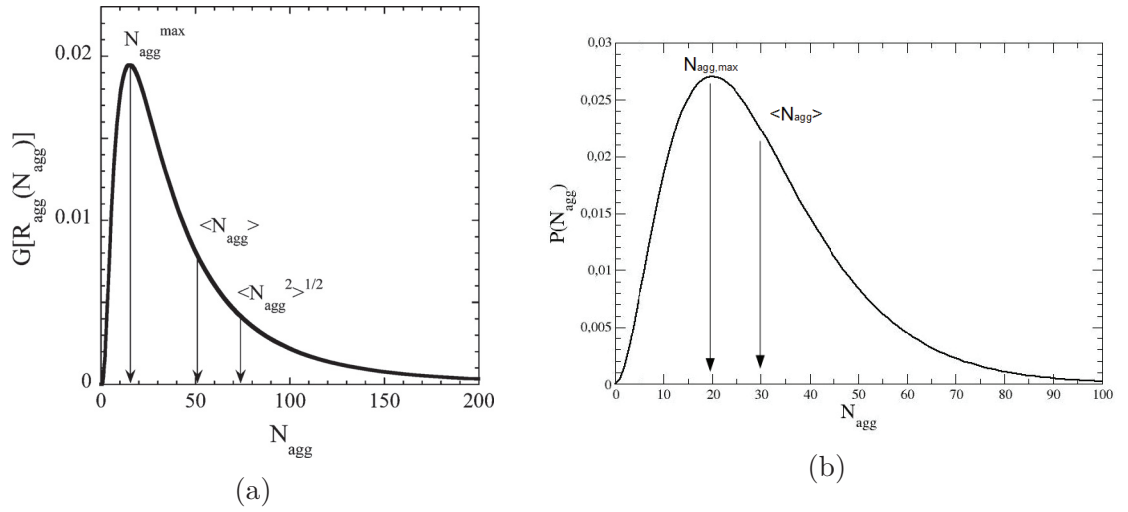


Figure 2.5: (a) Aggregate size distribution derived from the log-normal distribution of radius of aggregates [7]. N_{agg} is the number of primary silica particles in an aggregate and $G[R_{agg}(N_{agg})]$ is the corresponding normalized probability. (b) Aggregate size distribution deduced from the empirical formula in Eq 2.1 with $a = 2$ and $b = 10$.

Morphology of aggregates

The spatial extent of an aggregate can be characterized by the radius of gyration R_g ,

$$R_g^2 = \frac{1}{N_{agg}} \sum_{k=1}^{N_{agg}} (\mathbf{r}_k - \mathbf{r}_{c.m.})^2 = \frac{1}{2N_{agg}} \sum_{i,j=1}^{N_{agg}} (\mathbf{r}_i - \mathbf{r}_j)^2,$$

where \mathbf{r}_k is the position vector of particle k and $\mathbf{r}_{c.m.}$ is that of the center of mass [82]. The radius of gyration as a function of aggregate size N_{agg} are shown in Fig 2.6a, where each point is the average value from 500 aggregates generated via the DLA algorithm. The normalized distribution of the radius of gyration R_g from these 500 aggregates is shown in Fig 2.6b, where it is seen that most of the aggregates share a size close to the mean value. The fractal nature of DLA aggregates can only be seen for large aggregates. In our model, the aggregates are relatively small ($N_{agg} \leq 100$). They are not compact but are not sufficiently large to be called fractal.

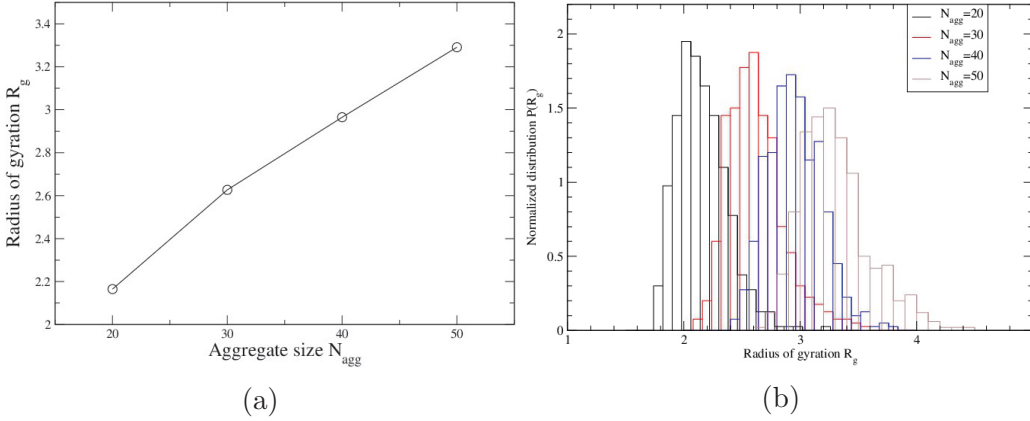


Figure 2.6: (a) Radius of gyration of aggregates generated via DLA. (b) Normalized distribution of radius of gyration from the same aggregates.

The complex structure of aggregates may not be accurately described solely by the radius of gyration. More detailed morphological information can be unveiled by the gyration tensor $\overline{\overline{S}}$, defined as follows:

$$\overline{\overline{S}} = \frac{1}{N_{agg}} \sum_{i=1}^N \mathbf{r}_i \mathbf{r}_i^T = \frac{1}{N_{agg}} \begin{bmatrix} \sum x_i^2 & \sum x_i y_i & \sum x_i z_i \\ \sum x_i y_i & \sum y_i^2 & \sum y_i z_i \\ \sum x_i z_i & \sum y_i z_i & \sum z_i^2 \end{bmatrix}, \quad (2.2)$$

where $\mathbf{r}_i = [x_i, y_i, z_i]$ is the position vector of particle i and \mathbf{r}_i^T is its transpose. The eigenvectors and the eigenvalues of the gyration tensor can provide more information of the morphology of the aggregate than the conventional method, this will be discuss in detail in section 4.4.1.

2.2 Simulation method

2.2.1 Interparticle potential

To represent the repulsive interaction between fillers, the Lennard-Jones potential (LJ potential) has been used as a standard choice, which includes a short-range repulsion and a long-distance attraction, and it is defined as follows:

$$U_{LJ}(r) = 4\epsilon \left[\left(\frac{\sigma}{r} \right)^{12} - \left(\frac{\sigma}{r} \right)^6 \right], \quad (2.3)$$

where ϵ is the depth of the potential, σ is the distance at which the potential is zero and r is the distance between the particles.

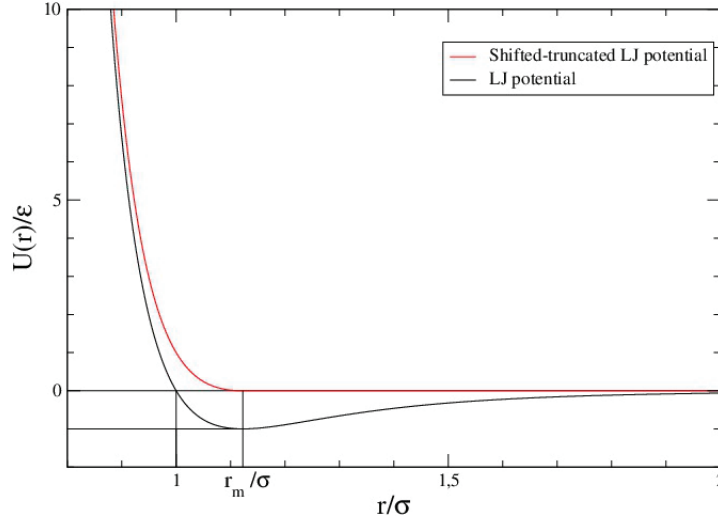


Figure 2.7: The black curve is the original Lennard-Jones potential, Eq. 2.3, and the red one is the shifted-truncated Lennard-Jones potential, in Eq. 2.4, and it turns to zero once the distance passes the minimum potential point $r_m = 2^{1/6}\sigma$.

In practice, the LJ potential has been modified and truncated to keep only the repulsive part of the potential. This truncation is done to avoid filler agglomeration as may be observed at low temperature. The truncated potential can be written as follows:

$$U_R(r) = \begin{cases} U_{LJ}(r) - U_{LJ}(r_m), & \text{if } r \leq r_m \\ 0, & \text{otherwise} \end{cases} \quad (2.4)$$

where $r_m = 2^{1/6}\sigma$ is the distance at which the LJ potential reaches its minimum value. As a result, the interaction force between two fillers is

$$\mathbf{F}_R(\mathbf{r}) = -\frac{dU_{int}(r)}{d\mathbf{r}} = \begin{cases} 24\epsilon \left[2 \left(\frac{\sigma}{r}\right)^{12} - \left(\frac{\sigma}{r}\right)^6 \right] \frac{\mathbf{r}}{r^2}, & \text{if } \|\mathbf{r}\| \leq r_m, \\ \mathbf{0}, & \text{otherwise.} \end{cases} \quad (2.5)$$

2.2.2 Brownian dynamics

We use Brownian dynamics to simulate nanoparticles in a simple viscous fluid. This is a limit case reached in the limit of very short matrix chains. In the Langevin dynamics, the motion equation for a particle can be written as follows:

$$M \frac{d\mathbf{V}(t)}{dt} = \mathbf{F}_c(t) + \mathbf{F}_d(t) + \mathbf{F}_r(t), \quad (2.6)$$

where M is the mass, $\mathbf{V}(t)$ is the velocity, $\mathbf{F}_c(t)$, $\mathbf{F}_d(t)$ and $\mathbf{F}_r(t)$ are the conservative force, the drag force and the random force. The drag force is an instantaneous force which includes the effect of solvent on fillers. The random force is delta-correlated and is related to the temperature of system. In a simple viscous liquid, the drag force is proportional to the velocity and viscosity η . For a spherical particle of radius a ,

$$\mathbf{F}_d(t) = -\zeta \mathbf{V}(t), \quad (2.7)$$

where $\zeta = 3\pi d\eta$ is the drag coefficient given by the Stokes-Einstein relation.

To model the rheology of filler particles in a simple fluid, we will consider that the nanoparticles obey overdamped Langevin dynamics. Indeed, for small particles, inertial

effects are negligible. For such Brownian dynamics, the equation of motion for particle n can be written as:

$$\frac{d\mathbf{R}_n}{dt} = \frac{1}{\zeta}\mathbf{F}_{n,c} + \mathbf{g}_n, \quad (n = 1, 2 \dots N), \quad (2.8)$$

where $\zeta = 3\pi d\eta$ is the friction coefficient, $\mathbf{F}_{n,c}$ is the conservative force for the particle n applied from the other particles, respectively, and \mathbf{g}_n is a random force which follows the Gaussian distribution with $\langle \mathbf{g}_n \rangle = \mathbf{0}$ and $\langle \mathbf{g}_{m,\alpha}(t)\mathbf{g}_{n,\beta}(t') \rangle = 2D\delta_{mn}\delta_{\alpha\beta}\delta(t-t')$, with the diffusion coefficient $D = k_B T/\zeta$. In practice, Eq. 2.8 is discretized as follows:

$$R_{n,\alpha}(t + \Delta t) - R_{n,\alpha}(t) = F_{n,\alpha} \frac{\Delta t}{\zeta} + \sqrt{2D\Delta t} \times f_G, \quad (\alpha = x, y, z) \quad (2.9)$$

where $R_{n,\alpha}(t)$ is the position of particle n in α direction at time t , $F_{n,\alpha}$ is the component of total interaction force for particle n in α direction, $\sqrt{2D\Delta t} \times f_G$ is the Brownian displacement from the random force in one time step, and f_G is a normally distributed random variable with zero mean and a unit standard deviation, i.e. whose probability distribution is the Gaussian

$$P(f_G) = \frac{1}{\sqrt{2\pi}} e^{-\frac{f_G^2}{2}}. \quad (2.10)$$

2.2.3 Generalized Langevin dynamics (GLE)

The generalized Langevin equation (GLE) is an extension of the Langevin equation to simulate the motion of massive fillers in a viscoelastic medium, such as an entangled polymer matrix. The viscoelasticity of the medium surrounding the nanoparticle is taken into account through the consideration of a memory kernel which represents physically a drag force which is non-local in time and a random force with non-trivial correlations. The equation of motion can be written as follows:

$$M \frac{dV(t)}{dt} = F_c(x(t)) - \int_0^t \Gamma(t-s)V(s)ds + F_r(t), \quad (2.11)$$

where M is an effective mass of the nanoparticle, $V(t)$ and $x(t)$ are the velocity and the position of the nanoparticle at time t , respectively. The first term F_c in the right-hand of equation is the conservative force, as described before. The second term $\int_0^t \Gamma(t-s)V(s)ds$ is the drag force. It does not only depends on the instantaneous velocity. Instead, it is non-local in time, as it involves all velocities in the past, through the memory kernel $\Gamma(t)$. The last term F_r is the random force, and is now time-correlated. Specifically, the time correlation function is related with the kernel $\Gamma(t)$ by the fluctuation-dissipation theorem,

$$\langle F_{r,i}(t+s)F_{r,j}(t) \rangle = k_B T \Gamma(s) \delta_{ij}, \quad \forall s \geq 0, \quad (2.12)$$

where δ_{ij} is the Kronecker delta, i, j denote the particle indices, and k_B is Boltzmann's constant. The influence of the matrix is encoded in memory kernel $\Gamma(t)$, which can be seen as a generalized drag coefficient:

$$\Gamma(t) = 3\pi d G_p(t), \quad (2.13)$$

where $G_p(t)$ is the stress relaxation modulus of the polymer matrix [80, 83, 84]. The particular case of a simple viscous medium is recovered if we make the memory kernel instantaneous in time $\Gamma(t) = 3\pi d \eta \delta(t)$.

Baczewski and Bond method

The time convolution in the drag force requires to know not only the instantaneous velocity but also all values in the past. If the simulated system involves many particles,

storing all velocity history would demand enormous memory resources. Baczewski and Bond propose a method to circumvent this issue [80]. One develops the memory kernel $\Gamma(t)$ and the stress relaxation of the entangled polymer matrix $G_p(t)$ via a Prony series:

$$G_p(t) = \sum_{k=1}^{N_P} G_{p,k} \exp\left(-\frac{t}{\tau_k}\right), \quad (2.14)$$

$$\Gamma(t) = \sum_{k=1}^{N_P} \frac{c_k}{\tau_k} \exp\left(-\frac{t}{\tau_k}\right) = 3\pi d \sum_{k=1}^{N_P} G_{p,k} \exp\left(-\frac{t}{\tau_k}\right), \quad (2.15)$$

where c_k , τ_k and $G_{p,k}$ are the coefficients of the Prony series (with $c_k/\tau_k = 3\pi d G_{p,k}$), which can be determined through nonlinear fitting the reference G_p describing the matrix with Eq 2.14, and N_P is the number of modes in a Prony series. They define the intermediate variables Z_k , $F_{r,k}$ and S_k related to the Prony component k :

$$Z_k(t) = - \int_0^t \frac{c_k}{\tau_k} \exp\left(-\frac{t-s}{\tau_k}\right) V(s) ds, \quad (2.16)$$

$$F_r(t) = \sum_{k=1}^{N_P} F_{r,k}(t), \quad (2.17)$$

$$S_k(t) = Z_k(t) + F_{r,k}(t), \quad (2.18)$$

where $F_{r,k}$ is the component of random force on mode k . Rather than integrating Eq 2.17 and Eq 2.18, they write the total differential of Z_k and $F_{r,k}$ in order to generate equations of motion having a similar form of a simple stochastic differential equation,

$$dZ_k(t) = -\frac{1}{\tau_k} Z_k(t) dt - \frac{c_k}{\tau_k} V(t) dt, \quad (2.19)$$

$$dF_{r,k}(t) = -\frac{1}{\tau_k} F_{r,k}(t) dt + \frac{1}{\tau_k} \sqrt{2k_B T c_k} dW_k(t), \quad (2.20)$$

where $W_k(t)$ represents a standard Wiener process. Thus, all the parameters here are instantaneous in time and the equations no longer involve time convolutions [80]:

$$M \frac{dV(t)}{dt} = F_c(x(t)) + \sum_k S_k(t), \quad (2.21)$$

$$dS_k(t) = -\frac{1}{\tau_k} S_k(t) dt - \frac{c_k}{\tau_k} V(t) dt + \frac{1}{\tau_k} \sqrt{2k_B T c_k} dW_k(t). \quad (2.22)$$

Simulation in practice

Original method Baczewski and Bond consider a system in simulation which is undergoing the GLE as given by Eqs 2.21 and 2.22 and show an example of how to integrate from step n to step $n+1$ by the rectangle method.

1. Advance V by a half step

$$V^{n+1/2} = V^n + \frac{\Delta t}{2M} F_c(x^n) + \frac{\Delta t}{2M} \sum_{k=1}^{N_P} S_k^n. \quad (2.23)$$

2. Advance x by a full step

$$x^{n+1} = x^n + V^{n+1/2} \Delta t. \quad (2.24)$$

3. Advance S_k by a full step

$$S_k^{n+1} = \theta_k S_k^n - (1 - \theta_k) c_k V^{n+1/2} + \alpha_k \sqrt{2k_B T c_k} B_k. \quad (2.25)$$

4. Advance V by another half step

$$V^{n+1} = V^{n+1/2} + \frac{\Delta t}{2M} F_c(x^{n+1}) + \frac{\Delta t}{2M} \sum_{k=1}^{N_P} S_k^{n+1}. \quad (2.26)$$

Here, B_k is drawn from an independent Gaussian distribution with mean zero and variance unity. The real-valued θ_k and α_k should satisfy the consistency conditions in Eq 2.22. Three methods may be considered for different choices of θ_k and α_k .

Method 1:

$$\theta_k = 1 - \frac{\Delta t}{\tau_k}, \alpha_k = \frac{\sqrt{\Delta t}}{\tau_k}. \quad (2.27)$$

Method 2:

$$\theta_k = \exp(-\Delta t/\tau_k), \alpha_k = \sqrt{\frac{(1-\theta_k^2)}{2\tau_k}}. \quad (2.28)$$

Method 3:

$$\theta_k = \exp(-\Delta t/\tau_k), \alpha_k = \sqrt{\frac{(1-\theta_k)^2}{\Delta t}}. \quad (2.29)$$

All the three methods satisfy the consistency conditions, $\theta_k = 1 - \Delta t/\tau_k + O(\Delta t^2)$ and $\alpha_k = \sqrt{\Delta t}/\tau_k + O(\Delta t)$. In addition, the third one provides the good stability when τ_k is small and it is favorable to choose a relatively large time step Δt in the simulation [80]. This is the method chosen for the following simulations.

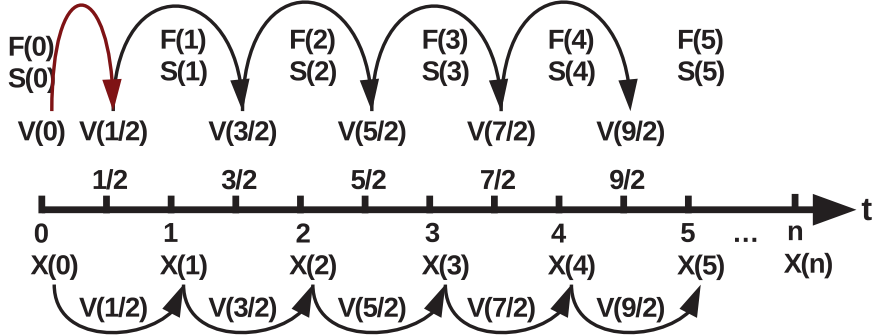


Figure 2.8: The mid-point method in practice.

Alternative method The original mid-point method cited requires to calculate the velocity value at integer moment $n + 1$, in which it requires two half step integrations via the calculation of the force F_c and the intermediate variable S_k at moment n and $n + 1$, which could double the computation time. If we focus on the mid-point velocity at a half time step, $V^{n+1/2}$ at time $t = n + 1/2$, which is integrated with a full time step from the previous mid-time-point velocity $V^{n-1/2}$ via the force F_c and the intermediate variable S_k at the integer moment n . Meanwhile, the integration of the position x , the force F_c and the intermediate variable S_k from moment n to the moment $n + 1$ are calculated from the velocity at the related half time step $V^{n+1/2}$, as shown in Fig. 2.8. Therefore, we propose the alternative mid-point method in the following:

1. If $t = 0$ ($n = 0$), advance V by a half step

$$V^{1/2} = V^0 + \frac{\Delta t}{2M} F_c(x^0) + \frac{\Delta t}{2M} \sum_{k=1}^{N_P} S_k^0, \quad (2.30)$$

where the initial velocity is $V^0 = 0$ in the simulations. If $t > 0$ ($n > 0$), advance V by a full step

$$V^{n+1/2} = V^{n-1/2} + \frac{\Delta t}{M} F_c(x^n) + \frac{\Delta t}{M} \sum_{k=1}^{N_P} S_k^n. \quad (2.31)$$

2. Advance x by a full step

$$x^{n+1} = x^n + V^{n+1/2} \Delta t. \quad (2.32)$$

3. Advance S_k by a full step

$$S_k^{n+1} = \theta_k S_k^n - (1 - \theta_k) c_k V^{n+1/2} + \alpha_k \sqrt{2k_B T c_k} B_k. \quad (2.33)$$

This alternative simulation method will produce the result identical to that from the original method and the computation time is divided by a factor two.

2.2.4 Application of the GLE to entangled polymer dynamics

In the original paper [80], the GLE methodology was rather general and did not describe the dynamics of entangled polymer melts. We discuss here the relevance of this approach to represent the polymer melt surrounding fillers. First, we should say that the reptation model predicts that the $G(t)$ of an entangled polymer melt may be written as a Prony series :

$$G_p(t) = \sum_{k=1}^{N_P} G_{p,k} \exp\left(-\frac{t}{\tau_k}\right) \quad (2.34)$$

where the longest relaxation times $\max \tau_{p,k}$ identifies with the terminal time, and the corresponding amplitude $G_{p,k}$ is the plateau modulus, on the order 0.5 – 1 Mpa for common polymer melts. Several strategies may be considered then in order to set the values of the coefficients $G_{p,k}$ and $\tau_{p,k}$ appearing in the Prony series. One possibility is to use values predicted by an analytical model, for instance the reptation model. Another possibility is to extract the coefficients after fitting the $G(t)$ of a specific polymer melt, obtained for instance by rheometry. A third possibility would consist in bridging the scales and compute the $G_p(t)$ using simulations where the polymer chains are represented explicitly. Candidates include molecular dynamics, dissipative particle dynamics or slip links simulations. The connection between the velocity kernel to be used in the GLE dynamics and the simulations with explicit polymer chains may be found in the fluctuation dissipation theorem, which relates the correlation of the random force $F_r(t)$ felt by the filler to the stress relaxation modulus $G_p(t)$, as described in eq. 2.12. Therefore, computing $\langle F_r(t+s)F_r(t) \rangle$ in an explicit simulation and fitting the result with a Prony series can feed the GLE with the associated $G_p(t)$ is clearly a bottom-up approach, for which local polymer dynamics information may pass to mesoscopic length scales.

In this manuscript, we will not build such a connection, but we leave this multiscale strategy for future work. We just wanted to emphasize that averaged polymer degrees of freedom may be described in a coarse grained manner within the GLE framework. Finally, we should give some practical considerations regarding the implementation of the Prony series in our GLE code. We did some tests so as to conclude how many modes k are necessary to represent the rheology of a polymer melt, and we saw that working with a single mode or using multiple modes yields no significant difference regarding the $G(t)$ of the model composites, for times t longer than the terminal time. Therefore, unless explicitly specified, we will work in the so-called single mode representation in the following, and describe the rheology of the polymer melt surrounding the nanofillers with a single exponential. The considerations discussed so far concern the representation of entangled polymer dynamics.

2.2.5 System units

In what follows, the energy unit is defined as $k_B T$, where k_B is the Boltzmann constant and T is the temperature. In the Brownian dynamics, the time unit τ_0 is associated to the viscosity of polymers, which is included in the friction of particles. In the generalized Langevin dynamics, the time unit τ_0 is related to the terminal relaxation time of the entangled polymer matrix. In both dynamics above, the unit of length is fixed by the nanoparticles diameter d .

It is important at this point to stress that the mass m is introduced in the generalized Langevin equation for mathematical convenience and thus does not represent necessarily the physical mass of nanoparticles. If it were to represent the physical mass of nanoparticles, the resulting time scale $d/\sqrt{k_B T/m}$ would be very short, as the case in molecular dynamics. Here, we are primarily interested in the viscoelastic properties of the model polymer nanocomposites at low frequency, where inertia does not play a role. Therefore, in the following we will not discuss the effect of the mass and consider that its value in the simulation serves only to set the value of the time step, from which the measured observables in simulations are independent.

To make the correspondence between our units and real system, let's take a typical example where the (longest) relaxation time of the polymer matrix is $\tau_{p,ref} = 1$ ms and the plateau stress relaxation modulus is $G_{p,ref} = 0.5$ MPa. With the units chosen above, the unit pressure (or stress) is $G_0 = k_B T/d^3$. For $d = 2.02$ nm, this corresponds to $G_{p,ref} = G_0$. For $d = 9.39$ nm, this corresponds to $G_{p,ref} = 100G_0$. Conversely, a given simulation can be interpreted as corresponding to several real systems, as long as they have the same value of the unit stress $k_B T/d^3$. The choice of units, and some typical parameters, are summarized in Table 2.1.

Quantity	Symbol	Simulation value	Realistic value
Energy	$k_B T$	1	4.1×10^{-21} J
Length	d	1	2.02 – 9.39 nm
Time	$\tau_{p,ref}$	1	1 ms
Stress	$G_{p,ref}$	1 – 100	0.5 MPa

Table 2.1: Correspondence between the values of the parameters in the simulations and for a real polymer nanocomposite. Note that the temperature is always the room temperature.

In this work, the volume fraction ϕ of filler is defined as the ratio between the volume of filler V_{fil} and the volume of the whole system V_{sys} ,

$$\phi = \frac{V_{fil}}{V_{sys}}, \quad (2.35)$$

where V_{fil} is the total volume occupied by filler particles and V_{sys} is the volume of simulation box. The number of individual nanoparticles or aggregates is noted as N , the aggregate size is represented by the number of primary particles contained in an aggregate, noted as N_{agg} , and the total number of aggregates is denoted as N_a .

2.2.6 Initial configurations

Now that we have explained how aggregates interact, we can come back to the process used to generate the initial configuration with a given volume fraction. We used two methods: the insertion method and the compression method. The insertion method consists in

placing the fillers in the simulation box one after another at a random position. As shown in Fig 2.9, the filler will be removed and replaced if superposition between two aggregates occurs. The compression method will stochastically place each fillers in a separated isolated box to avoid any contact between them at the very beginning of the process, as shown in Fig 2.10a. Then, all the unit boxes will be merged to form a unique large box which will start to progressively decrease its size in order to compress the fillers and produce a configuration with a given filler volume fraction, as shown in Fig 2.10b. During the compression process, the fillers are treated as solid objects, undergoing the rigid motion characterized by translation of the center of mass and rotation around the center of mass. Hence, the springs in the aggregate are not taken in account during the compression process. For the preparation step, we used the Brownian dynamic combining the inertial terms which may not have a realistic physical meaning. The torque of the aggregate, containing the mass, is an instantaneous terms which is related to the rotation of the aggregate through its center of mass in one time step. All the forces felt by the primary particles of an aggregate are summarized through its center of mass and this corresponds to the translation motion of an aggregate. One compression step occurs when the current system does not have the superposition of particles. Hence, the system is not fully relaxed in each compression step for sake of speeding up the generating process of the initial configuration of system. Once the system reached the defined volume fraction of fillers, a relaxation process will occur with the Brownian dynamics discussed above.

After the initialization process, a relaxation process will occur during which the fillers obey overdamped Brownian dynamics. The relaxation stops when both the global energy and the pressure of the system converge towards constant values. This indicates that the system is well relaxed. When convergence is observed, and if the subsequent dynamics is supposed to be the generalized Langevin dynamics, we need to impose initial random velocities. This is done by adding a random velocity $V = \pm\sqrt{k_B T/m}$ in all directions (see [80] for details).

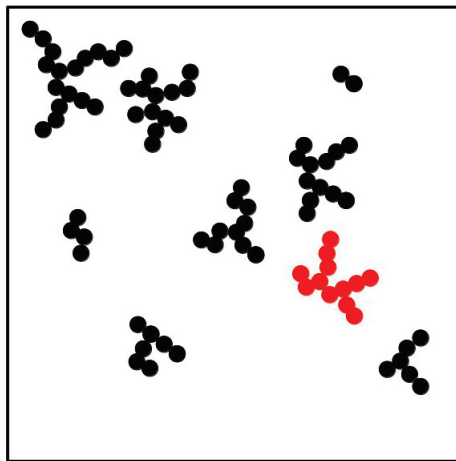


Figure 2.9: Schematic of the insertion method. The black aggregates are already placed while the red one is the newly inserted aggregate.

The individual nanoparticles and the flexible aggregates can easily move away from each other, even at high volume fraction. Hence, the insertion method has been used to generate the initial configurations in these cases. For the rigid aggregates (either mono- or polydisperse), we used a compression method. One advantage is that that it avoids non-physical situations, such as the superposition of fillers, that could occur with insertion method. This method has often proved capable to generate an initial configuration of monodisperse rigid aggregates but less satisfactory for polydisperse rigid aggregates. In particular, the compression method runs into difficulties at high filler volume fraction, which

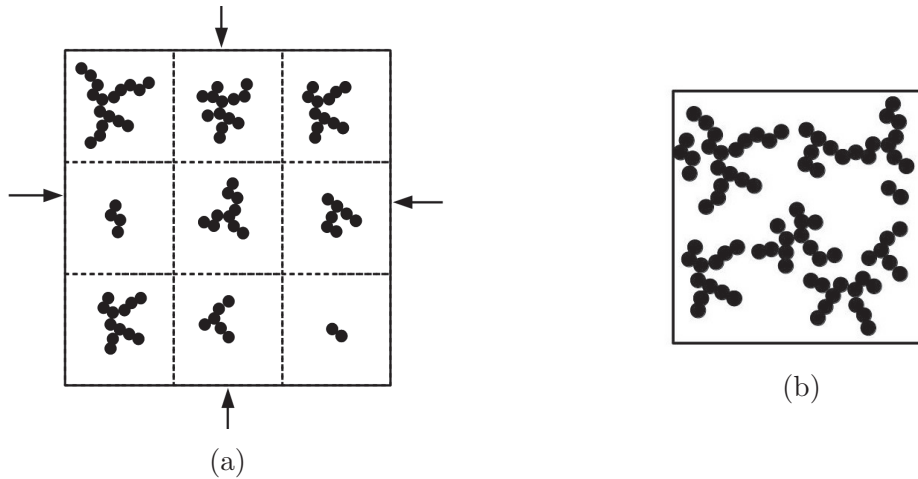


Figure 2.10: Schematic of the compression method. (a) Initial box with unit box of aggregate and (b) final box after compression.

may be due to the fractal morphology of rigid aggregates. Hence, regardless of the possible entanglement between rigid aggregates, the configuration for polydisperse aggregates at high volume fraction (near $\phi_{agg} = 18\%$) were reached with the insertion method, in which the rigid aggregates are placed in order of aggregate size, the large aggregates are inserted before the small one.

The available initial configurations of rigid aggregates are shown in Fig 2.11. The monodisperse rigid aggregates can reach a relatively high filler volume fraction $\phi = 17\%$ with a small unique aggregates size $N_{agg} = 20$ by the compression method, as shown in Fig 2.11a. Nonetheless, the accessible filler volume fractions decrease dramatically when increasing aggregate size. For instance, with a large aggregate size $N_{agg} = 50$, the highest achievable filler volume fraction in a small box containing $N = 30$ aggregates, is $\phi = 12\%$. The situation is much harsher for the polydisperse rigid aggregates, which is not displayed here. Hence, the insertion method has been employed to form the initial configuration of poly-disperse rigid aggregates and the feasible filler volume fractions are shown in Fig 2.11b, where the aggregate size distribution follows the log-normal law deduced from the empirical formula (Eq 2.1) with parameters $a = 2$ and $b = 10$. The highest accessible filler volume fraction can attain 18% with maximum 200 aggregates in box. Despite of the potential artificial entanglement between aggregates, the insertion method appears convenient to generate initial configurations, the poly-disperse rigid aggregates system can reach a relatively high filler volume fraction $\phi = 15\%$ with a large box containing 1000 aggregates.

Conclusion

We have presented the basis of a mesoscopic model aimed at describing the dynamics and the rheology of polymer composites containing small non-compact aggregates. The description of the relevant mesoscale structures is computationally expensive using standard atomistic simulations, such as molecular dynamics. Therefore, we followed an alternative strategy and coarse-grained the composite at the scale of the nanofillers. The polymer degrees of freedom have been averaged out, and represented by a velocity kernel which accounts for the viscoelasticity of the entangled polymer. Note that the polymer matrix is represented in the present model by using its rheological data from relevant experiment or simulation, for which the polymeric degrees of freedom are explicitly represented. These parameters entering the velocity kernel can be characterized by using the data from relevant experiment or simulation of a polymer matrix, and one can target then a specific model

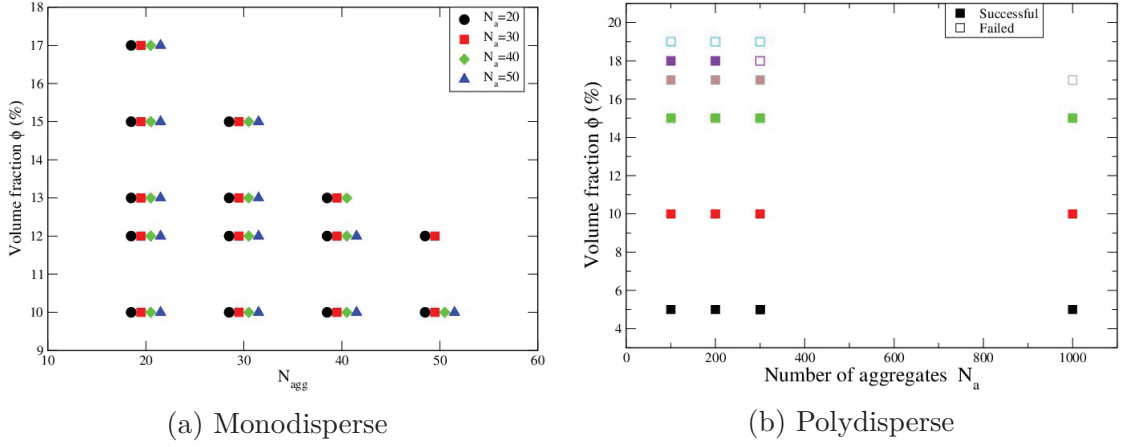


Figure 2.11: Volume fractions of available configurations for (a) mono-disperse and (b) poly-disperse rigid aggregates, in terms of aggregates size N_{agg} and number of aggregates N_a , by (a) the compression method and (b) the insertion method, respectively. The hollow and solid symbols are the impossible and the available filler volume fractions, respectively.

composite.

With this model in hand, we expect to quantitatively measure the influences of the filler type, the filler volume fraction and the filler size on the rheology of the model composite, and also the morphology of fillers in simulations, especially under shear deformation. However, the effect of the polymer chain bridging is not included in the present model yet. Therefore, the possibility of the polymer chains to transmit stress between neighboring fillers is not taken into account. An additional interaction force between fillers or a semi-empirical potential may be considered to account for the contribution of the polymer-filler interface. This extension is left for future work.

 Linear rheology: simulations and results

 Contents

3.1	Stress relaxation modulus	48
3.1.1	Microscopic view of stress tensor	48
3.1.2	Green-Kubo approach	49
3.1.3	Diagonal and cross contributions to the stress	49
3.1.4	Harmonic zone	50
3.2	Influence of filler and matrix parameters	51
3.2.1	Effect of filler type	52
3.2.2	Effect of filler volume fraction	53
3.2.3	Effect of aggregate size	55
3.2.4	Effect of primary particle size	56
3.2.5	Effect of polymer matrix relaxation time	57
3.2.6	Effect of aggregates polydispersity	58
3.2.7	Summary: Reinforcement	58
3.3	Slow dynamics	59
3.3.1	Diffusion coefficient	60
3.3.2	Orientation of aggregates	61
3.3.3	Dynamic structure factor	62

Introduction

When the deformation is small enough, the system exhibits a linear response. In this chapter, we probe the linear regime using a Green-Kubo approach [85]. No deformation is imposed on the system. Rather, the stress relaxation modulus is calculated from the time correlation of the stress in the system at equilibrium. The storage and the loss moduli can subsequently be obtained from the stress relaxation modulus by Fourier transform.

We investigate in a systematic manner how the linear rheology depends on the aggregates properties: the type and volume fraction of filler, the aggregate size and their mono- or polydispersity. We use the two methods presented in the Chapter 2: the Brownian dynamics to describe a simple viscous fluid, which is considered here a unentangled polymers matrix, and the generalized Langevin dynamics (GLD) to model a viscoelastic entangled polymers matrix. For simplicity, the memory kernel is characterized by a single plateau modulus and a single relaxation time. The goal of this exhaustive exploration is to identify the key parameters affecting the linear rheology of the model composites. While we essentially focus on the stress relaxation modulus, we also consider the dynamics of individual aggregate and the dynamic structure factors.

3.1 Stress relaxation modulus

3.1.1 Microscopic view of stress tensor

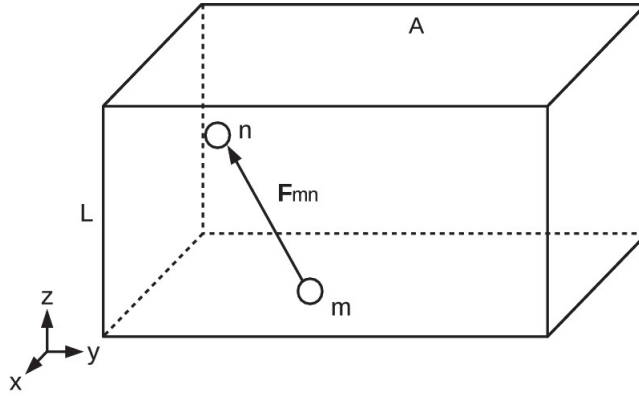


Figure 3.1: Microscopic view of stress [86].

We first explain how we compute the stress tensor in simulations [86]. The starting point is Eq 1.13, where the stress is defined as the ratio between the applied force and the cross-sectional area,

$$\sigma_{\alpha z} = \frac{\langle F_{\alpha} \rangle}{A_z}, \quad (\alpha = x, y, z). \quad (3.1)$$

Here $\sigma_{\alpha\beta}$ is the component $\alpha\beta$ of the stress, A_z is the area perpendicular to the z direction and $\langle F_{\alpha} \rangle$ is the average interaction force along direction α . $\langle \dots \rangle$ denotes an average over the canonical ensemble. More explicitly, for a dynamical quantity $A(t)$, the canonical ensemble average can be written as an integral over phase space [85],

$$\langle A(t) \rangle = \frac{\int d\mathbf{r}^N d\mathbf{p}^N \exp(-H(\mathbf{r}^N, \mathbf{p}^N)/k_B T) A(t; \mathbf{r}^N, \mathbf{p}^N)}{\int d\mathbf{r}^N d\mathbf{p}^N \exp(-H(\mathbf{r}^N, \mathbf{p}^N)/k_B T)}, \quad (3.2)$$

where \mathbf{r}^N and \mathbf{p}^N denote the positions and momenta of the N particles and H the Hamiltonian of the system.

In a system of pairwise interacting particles, the interaction force on a the cross-section at height h includes the contributions from all pairs having one particle on each side:

$$F_{\alpha} = \sum_{m,n} F_{mn,\alpha} \Theta(h - R_{mz}) \Theta(R_{nz} - h). \quad (3.3)$$

Here, R_{mz} is the z coordinate of particle m , $F_{mn,\alpha}$ is the α component of the interaction force applied on particle n by particle m . Θ is the Heaviside function: $\Theta(x) = 0$ if $x < 0$,

$\Theta(x) = 1$ if $x > 0$. In a homogeneous fluid, the average interaction force $\langle F_\alpha \rangle$ is independent from the height h of the cross section, thus it can be written as follows:

$$\langle F_\alpha \rangle = \frac{1}{L} \int_0^L \left\langle \sum_{m,n} F_{mn,\alpha} \Theta(h - R_{mz}) \Theta(R_{nz} - h) \right\rangle dh, \quad (3.4)$$

where L is the thickness of system. Introducing $R_{mn,z} = R_{mz} - R_{nz}$ as the relative distance from particle m to n in the z direction, and using $F_{mn,\alpha} = -F_{nm,\alpha}$, the average interaction force is

$$\langle F_\alpha \rangle = -\frac{1}{L} \left\langle \sum_{m < n} F_{mn,\alpha} R_{mn,z} \right\rangle. \quad (3.5)$$

Hence, the stress of system in the αz direction can be finally written as a function of the relative force and relative distance between the pairs,

$$\sigma_{\alpha z} = -\frac{1}{V} \sum_{m < n} \langle F_{mn,\alpha} R_{mn,z} \rangle, \quad (3.6)$$

where $V = AL$ is the volume of the system.

3.1.2 Green-Kubo approach

In the linear regime, the stress relaxation modulus $G(t)$ can be obtained from the time correlation of the shear stress, via the linear response theory [85, 49, 87],

$$G(t) = \frac{V}{k_B T} \frac{1}{3} \left\langle \sum_{\alpha=1}^3 \sum_{\beta>\alpha}^3 \sigma_{\alpha\beta}(t) \sigma_{\alpha\beta}(0) \right\rangle, \quad (3.7)$$

where V is the volume of system, k_B is the Boltzmann constant, T is the system temperature, $\sigma_{\alpha\beta}$ is the non-diagonal stress element and $\langle \dots \rangle$ denotes an ensemble average. Since the stress tensor is symmetric, $\sigma_{\alpha\beta} = \sigma_{\beta\alpha}$, the stress relaxation modulus can be considered as the mean value of its three non-diagonal components, G_{xy} , G_{xz} and G_{yz} , which are related to the time correlation of shear stress along the corresponding direction.

The complex modulus $G^*(\omega) = G'(\omega) + iG''(\omega)$, where $G'(\omega)$ is the storage modulus and $G''(\omega)$ is the loss modulus, can be calculated from the stress relaxation modulus $G(t)$ by the Fourier transform expressed in Eq 1.39,

$$G^*(\omega) = G'(\omega) + iG''(\omega) = i\omega \int_0^\infty G(t) \exp(-i\omega t) dt.$$

Then the storage and the loss moduli can be separately calculated as the real and the imaginary parts of the complex modulus G^* expressed in Eq 1.37 and 1.38,

$$G'(\omega) = \omega \int_0^\infty G(t') \sin(\omega t') dt',$$

$$G''(\omega) = \omega \int_0^\infty G(t') \cos(\omega t') dt'.$$

3.1.3 Diagonal and cross contributions to the stress

Here we examine the various contributions to the stress tensor. As expressed in Eq 3.6, the stress involves the product of the interaction force and the relative distance between a pair of particles. Hence, the stress includes the different contributions from the various interaction forces. For individual nanoparticles, there is only one contribution to

the stress, which is coming from the Lennard-Jones interaction. In flexible aggregates, connective springs add a new term σ_{CS} , while in rigid aggregate, virtual springs yields another contribution σ_{VS} . In short,

$$\sigma_{IndNano} = \sigma_{LJ}, \quad (3.8)$$

$$\sigma_{FlexAgg} = \sigma_{LJ} + \sigma_{CS}, \quad (3.9)$$

$$\sigma_{RigAgg} = \sigma_{LJ} + \sigma_{CS} + \sigma_{VS}. \quad (3.10)$$

The stress relaxation modulus $G(t)$ can be calculated via the auto-correlation of the shear stress, as expressed in Eq 3.27. The individual nanoparticles are the simplest case since there is only one component in the shear stress, as shown in Eq 3.8. The aggregates contains multiple components in the stress, thereupon the relevant stress relaxation modulus contains cross-terms, which are the time correlation between different components of the stress. For instance, the stress relaxation modulus $G(t)$ of the flexible aggregates can be written as follows:

$$\begin{aligned} G_{FlexAgg}(t) &= \frac{V}{k_B T} \langle \sigma_{FlexAgg}(t) \sigma_{FlexAgg}(0) \rangle \\ &= \frac{V}{k_B T} \langle \sigma_{LJ}(t) \sigma_{LJ}(0) + \sigma_{CS}(t) \sigma_{CS}(0) \rangle + \frac{V}{k_B T} \langle \sigma_{LJ}(t) \sigma_{CS}(0) + \sigma_{CS}(t) \sigma_{LJ}(0) \rangle, \end{aligned}$$

where the terms in the second bracket on the right hand are the cross-terms between the components of the stress from the LJ potential and the connective springs. Similarly, for the rigid aggregates,

$$\begin{aligned} G_{RigAgg}(t) &= \frac{V}{k_B T} \langle \sigma_{RigAgg}(t) \sigma_{RigAgg}(0) \rangle \\ &= \frac{V}{k_B T} \langle \sigma_{LJ}(t) \sigma_{LJ}(0) + \sigma_{CS}(t) \sigma_{CS}(0) + \sigma_{VS}(t) \sigma_{VS}(0) \rangle \\ &\quad + \frac{V}{k_B T} \langle \sigma_{LJ}(t) \sigma_{CS}(0) + \sigma_{LJ}(t) \sigma_{CS}(0) + \sigma_{CS}(t) \sigma_{VS}(0) + \dots \rangle, \end{aligned} \quad (3.11)$$

where the last term in the right-hand side is obtained by interversion of indices in the second bracket.

The cross correlation of the stress are generally negative, hence the total correlation of stress is smaller than the sum of the non-cross terms [87]. The effect of the cross-terms is shown in Fig 3.2. Obviously, the total $G(t)$ is smaller than the sum from the components apart from the cross-terms, which indicates that the cross-terms are negative as expected [87]. In the flexible aggregates, we observe that both diagonal term σ_{LJ} and σ_{CS} display a slow dynamics along the whole time range considered here. This is also true for the rigid aggregates, for which the stress relaxation modulus includes the third diagonal term σ_{VS} . In this case, we see also that the contribution of virtual springs is dominated by the other two diagonal terms. The long relaxation time, evidenced here for all the diagonal contributions to $G(t)$, points to the existence of the slow degree of freedom in the system of aggregates, which will be discussed in section 3.3.

3.1.4 Harmonic zone

As shown in Fig 3.3b, the short time rheological response of the aggregates may display an oscillatory response. In this section, we discuss the origin and significance of this "harmonic zone".

We first observe that this oscillatory behavior appears only in the simulations of entangled polymer matrix, i.e. with the generalized Langevin equation that includes the inertial term and the polymer matrix is described as viscoelastic. Oscillations are absent, as the

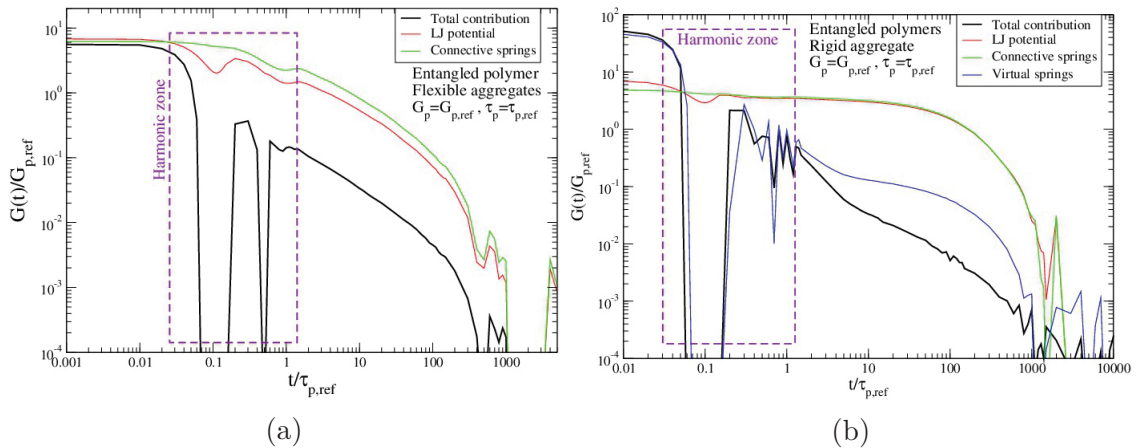


Figure 3.2: Comparison between the components of the stress relaxation modulus $G(t)$ for (a) flexible aggregates and (b) rigid aggregates with entangled polymer matrix ($G_p = G_{p,ref}$ and $\tau_p = \tau_{p,ref}$). Both the flexible and the rigid aggregates have the unique aggregate size $N_{agg} = 20$ and the same volume fraction $\phi = 10\%$.

Brownian dynamics neglects inertia and the polymer matrix is considered to be purely viscous. This suggests that oscillations result from an interplay between the effective elasticity, from both the springs (real or virtual) and the polymer matrix, and inertia. The typical period of oscillation is not simple and related to all the three elements noted above. Among them, the period of oscillation from the springs is related to the spring stiffness k and the mass m of the nanoparticles through $\tau_{harm} = 2\pi\sqrt{k/m} \simeq 0.628$ time unit, if $k = 100$ force/distance unit and $m = 1$ mass unit. Note that the elasticity of the polymer matrix appears to give rise to oscillation in the stress relaxation modulus $G(t)$ by the interplay with the springs, and display a typical period of oscillation different from that of the springs, but the effect appears to be relatively small, as can be readily proven by comparing the harmonic zones in the individual nanoparticles system (without springs) and the aggregates system (containing spring network). Thus, the main origin of the oscillations in the short time stress response comes from the spring network.

The oscillatory behavior of $G(t)$ at short times occurs in a frequency range where the inertia of the nanoparticles is not negligible, corresponding to $\omega \simeq 2\pi/\tau_{harm} \simeq 6.28$ frequency unit with the harmonic period $\tau_{harm} \simeq 1$ time unit. However, we are primarily interested in studying reinforcement as occurring in frequency range where the nanoparticle dynamics is overdamped, that is to say $\omega \ll 2\pi/\tau_{harm}$. Therefore, we believe the oscillations do not provide really useful information on the stress relaxation modulus $G(t)$ and it may only affect the corresponding storage and the loss moduli at high frequency $\omega \sim 2\pi/\tau_{harm} \gg \tau_{p,ref}^{-1}$, which is not of interest throughout this work. For these reasons, the harmonic zone will be masked in the future figures and only be indicated by a box with dashed lines. This only serves to put the emphasis on the really significant part of the data.

3.2 Influence of filler and matrix parameters

In this section, we will examine how the linear rheology is influenced by the filler and matrix parameters. We first briefly describe our reference system and how the results were obtained.

Representing the viscoelastic kernel of a realistic polymer matrix usually involves multiple modes in the Prony series. This approach, would allow us to examine a specific nanocomposite. Here, our goal is to understand, generically, the role of the polymer matrix/viscoelasticity and the interplay with filler characteristics. We thus start with a much

simpler situation: the matrix kernel is assumed mono-mode, that is with a single plateau $G_{p,0}$ and a single relaxation time $\tau_{p,0}$,

$$G_p(t) = G_{p,0} \exp\left(-\frac{t}{\tau_{p,0}}\right). \quad (3.12)$$

This is the default case, unless otherwise mentioned. The typical physical values are taken to be $G_{p,0} = 0.5$ MPa and $\tau_{p,0} = 1$ ms. These values correspond to a polybutadiene matrix having a molecular weight $M_W = 40$ K [67]. As discussed in the previous section, $G_{p,0}$ and $\tau_{p,0}$ set the unit of stress and time, respectively.

Two others remarks apply to all the data shown below. i) The stress relaxation modulus $G(t)$ and other computed quantities all results from an average over at least 10 independent simulations. This serves to improve the statistics of the parameters of interest, especially for the behavior of the observables at long times. ii) In all curves, including the stress relaxation modulus or the dynamic moduli, only the contribution of the filler is shown. Unless otherwise stated, the contribution of the polymer matrix is not taken into account.

3.2.1 Effect of filler type

The reinforcement on the stress relaxation modulus $G(t)$ from three different types of fillers has been studied in both a simple viscous fluid and an entangled polymer matrix, as shown in Fig 3.3. All the systems share the same filler volume fraction $\phi = 10\%$ and the aggregates are monodisperse with a uniform size $N_{agg} = 50$.

For the individual nanoparticles system, the stress relaxation modulus $G(t)$ decreases within a very short time period and it vanishes at long times both for a simple viscous fluid and an entangled polymer matrix. Both the flexible and the rigid aggregates exhibit a reinforcement near one and two order of magnitude on $G(t)$ at short times and they exhibit a slow-down dynamics at long times, regardless of the nature of the polymer matrix. The rigidity of the aggregates has a significant influence on the reinforcement, the rigid aggregates exhibit a $G(t)$ at short times which is one order of magnitude higher than the flexible aggregates.

Long relaxation times have been observed experimentally in the stress relaxation modulus of filled polybutadienes, see Fig. 2 of [67]. Our simulations show that long relaxation times appear only for aggregates systems, whether flexible or rigid. Therefore, we interpret the long time relaxation of $G(t)$ as seen in experiments, as an evidence of the existence of partial aggregation. Clearly also, long relaxation is not necessarily associated with the existence of polymer bridging between nanoparticles.

As mentioned before, the storage modulus $G'(\omega)$ and the loss modulus $G''(\omega)$ can be obtained from the stress relaxation modulus $G(t)$ via Fourier transform¹. The results for the system of Fig 3.3b is shown in Fig 3.4, where the different filler types lead to reinforcement on both the storage and the loss moduli. Knowledge of the dynamic moduli (G' and G'') in the linear regime may help in the choice of the shear frequency in the studies of the nonlinear shear phenomenon, such as the Payne effect, that we will analyze in the next chapter.

For the individual nanoparticles system, the storage modulus G' and the loss modulus G'' in both a simple viscous fluid and an entangled polymer matrix exhibit power law dependence with frequency ω^2 and ω^1 at low frequency, respectively, as predicted for a Maxwell model in Eq 1.37 and 1.38. This may indicate that the individual nanoparticles does not play a major role in the rheological reinforcement of a filled polymer matrix in spite of their good dispersion, which may be due to the lack of attractive interaction between the nanoparticles. Hence, they may display a rheological behavior similar to those characterizing

¹ Both the storage modulus G' and the loss modulus G'' are in unit of $G_{p,ref}$ and the frequency ω is in unit of $\tau_{p,ref}$.

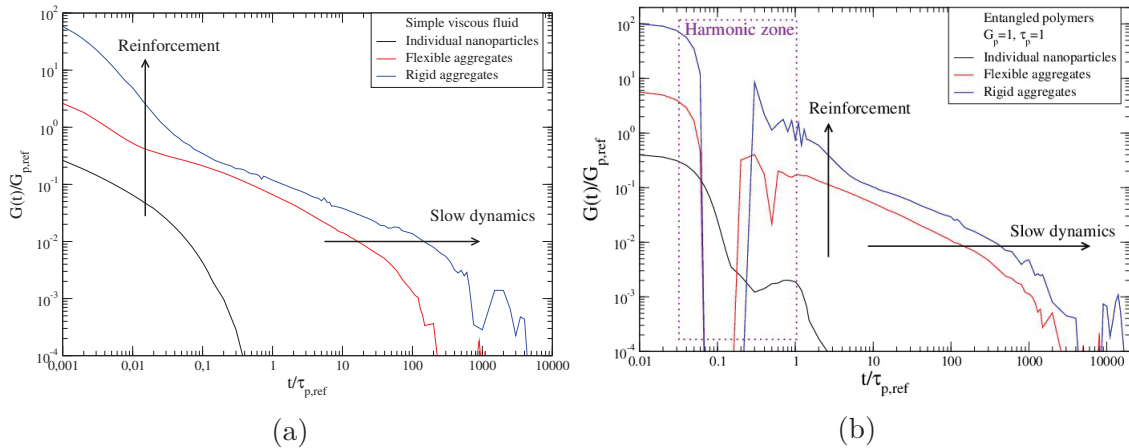


Figure 3.3: Effect of the filler type on the stress relaxation modulus $G(t)$ with (a) a simple viscous fluid and (b) an entangled polymers matrix, with a fixed volume fraction $\phi = 10\%$ and the unique aggregate size $N_{agg} = 50$.

a polymer melt, for which, the stress relaxation modulus $G(t)$ decreases exponentially and the storage and the loss moduli display the same frequency behavior: $G' \sim \omega^2$ and $G'' \sim \omega$ at low frequency.

In contrast, for the flexible aggregates system, the storage modulus G' approaches the power law $G' \sim \omega^2$ only at very low frequency and the rigid aggregates do not exhibit the same tendency on the storage modulus G' . This indicates that the morphology of the aggregates, even for the flexible aggregates, and the rigidity of the aggregates are both important factors in the reinforcement of filled polymer matrix system, which can be seen in the slow dynamics observed at long times in the stress relaxation modulus $G(t)$. Nonetheless, the loss modulus G'' of both the flexible and the rigid aggregates obeys the power law ω^1 over a large range of frequency, which may be due to the weak volume fraction of the aggregates, $\phi = 10\%$ here. Note also that the existence of the harmonic zone is clearly shown at high frequency, but our discussion concerns primarily the rheological behavior at lower frequencies where inertia plays no role.

All three types of filled polymers systems exhibit liquid-like behavior at low frequency and solid-like behavior at high frequency. For the individual nanoparticle system, one can identify a clear single gel point, where $G' \approx G''$ in both a simple viscous fluid and an entangled polymers matrix. For the aggregates systems, there can be one or two gel points. The flexible aggregates systems display a gel state, where $G' \simeq G''$, in the intermediate frequency regime and there are more than two gel points along the whole range of frequency.

The individual nanoparticles will not be considered in the following owing to their low rheological response, as quantified by the stress relaxation modulus $G(t)$ (Fig. 3.3), and the dynamic moduli (Fig 3.4). From now on, the aggregates, including both the flexible and the rigid aggregates, will be the essential systems considered to characterize the effect of a series of parameters describing the fillers, such as the volume fraction and the aggregates size, on the rheology of the model nanocomposites.

3.2.2 Effect of filler volume fraction

The filler volume fraction is generally considered to have a major effect on the mechanical and rheological properties of polymer nanocomposites [76, 19, 7]. Furthermore, at the high volume fraction of filler, the mechanism which induces reinforcement may change as illustrated in Fig 1.9.

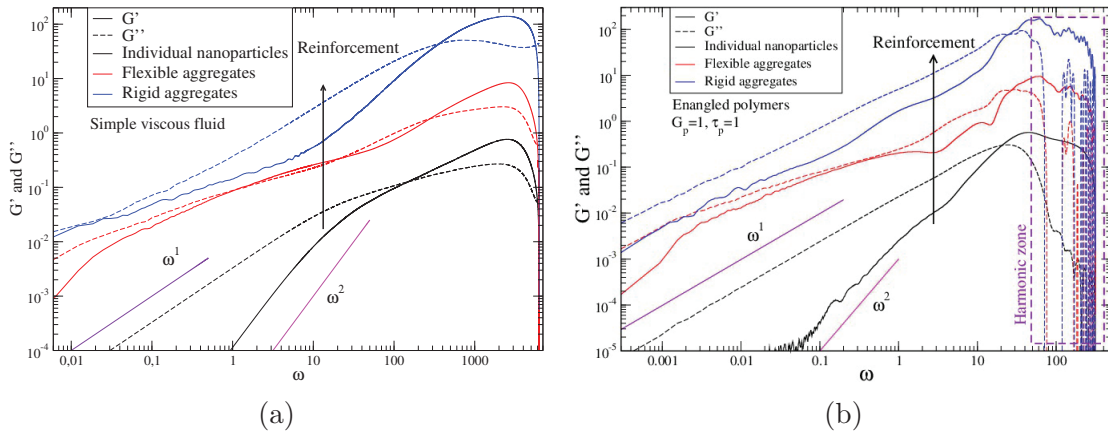


Figure 3.4: Effect of filler types on the storage modulus $G'(\omega)$ (solid lines) and the loss modulus $G''(\omega)$ (dashed lines) for the systems shown in Fig 3.3.

Simple viscous fluid In the case with a simple viscous fluid, both the flexible and the rigid aggregates exhibit a reinforcement level which increases with the volume fraction of aggregates, as shown in Fig 3.5. In this latter figure, a series of volume fraction from 10% to 40% with a fixed aggregate size $N_{agg} = 50$ is presented and for the rigid aggregates system, we present volume fractions ranging from 10% to 17% with a fixed aggregate size $N_{agg} = 20$. The stress relaxation modulus $G(t)$ of the rigid aggregates is enhanced by more than one order of magnitude compared to the flexible aggregates at short times, even though the rigid aggregates have a small size. This can be related to the effect of filler rigidity discussed before. Furthermore, the flexible aggregates system exhibits a linear relationship between the reinforcement and the volume fraction of aggregates, at moderate volume fractions $\phi \leq 30\%$ as can be appreciated if we rescale the $G(t)$ curves by the volume fraction, as one can see via the effective viscosity in section 3.2.7. This may indicate that the reinforcement mechanism in flexible systems remains the same as that in a dilute system, probably due to the repulsive nature of the interaction between nanoparticles. For all the volume fractions analyzed, the flexible aggregates system undergoes the same relaxation dynamics, and from this perspective the flexible aggregates system can be considered similar to a big soft colloid or to a star polymer. For rigid aggregates, the range of volume fraction can not be varied beyond 17% for the small aggregate size $N_{agg} = 20$ due to the difficulty in generating high volume fraction configurations, as mentioned in the previous section 2.2.6. Obviously, the volume fraction 17% is not enough to change significantly the relaxation dynamics.

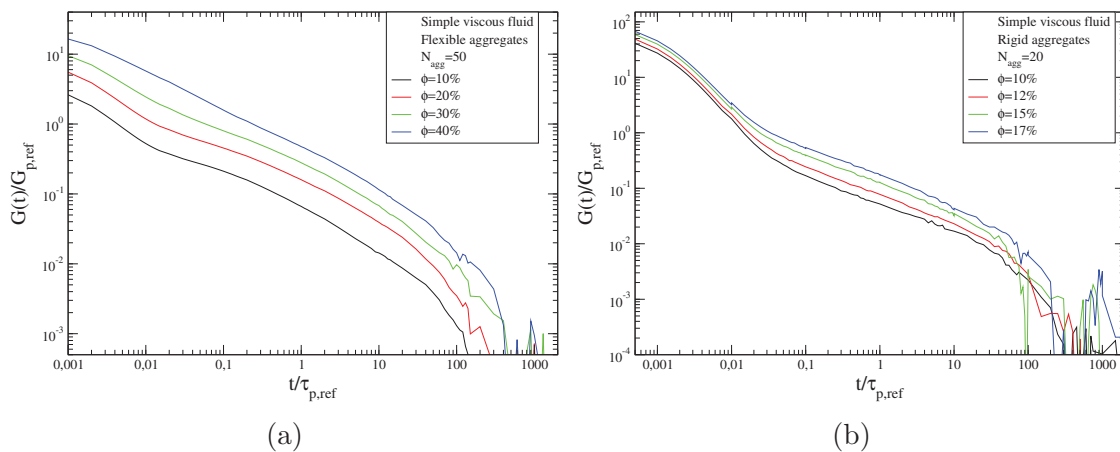


Figure 3.5: Effect of volume fraction for (a) flexible aggregates ($N_{agg} = 50$) and (b) rigid aggregates ($N_{agg} = 20$) in a simple viscous fluid.

Entangled polymer Both the flexible and rigid aggregates, with a fixed aggregate size $N_{agg} = 20$, exhibit reinforcement increasing with the volume fraction of aggregates, as shown in Fig 3.6, in which the volume fraction of aggregates varies from 10% to 40% for the flexible aggregates systems and from 10% to 17% for the rigid aggregates systems. At short times, the stress relaxation of rigid aggregates is 1 order of magnitude higher than that of flexible aggregates, at a common value of the volume fraction $\phi = 10\%$. Again, both the flexible and the rigid aggregates exhibit a similar relaxation mechanism for the range of volume fractions analyzed, even with entangled polymer matrix, since the stress relaxation modulus $G(t)$ shows a quasi-linear relationship with the volume fraction of aggregates Φ , as can be appreciated if the $G(t)$ curves are scaled by Φ . Such linearity stems probably from the repulsive nature of contacts between aggregates.

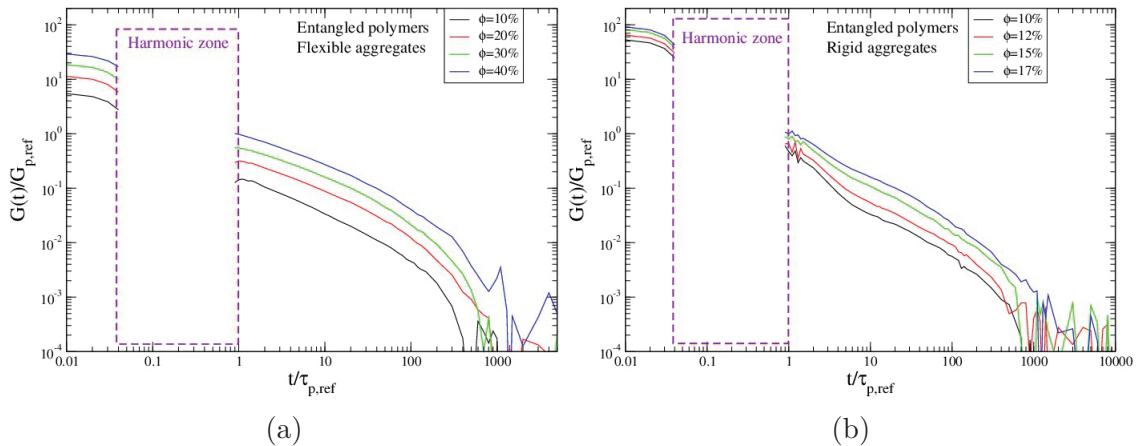


Figure 3.6: Effect of volume fraction of (a) flexible aggregates and (b) rigid aggregates in an entangled polymers matrix with a unique aggregate size $N_{agg} = 20$.

3.2.3 Effect of aggregate size

The aggregates size is fully characterized by the number of primary particles in an aggregate, N_{agg} . As shown in Fig 2.6, the radius of gyration of aggregate varies as a function of aggregate size N_{agg} and the distribution of aggregates size broadens when the aggregates are big. Here, we study how the aggregate size affects the reinforcement and the rheological properties of the model composites.

Simple viscous fluid In the case with a simple viscous fluid, the flexible aggregates exhibit a reinforcement on the stress relaxation modulus $G(t)$ increasing with the aggregate size only at long times, as shown in Fig 3.7a. In this latter figure, the aggregates sizes has been varied from $N_{agg} = 20$ to 50 with a fixed volume fraction $\phi = 10\%$. The effect also occurs for the rigid aggregates and can be described as a reinforcement along the whole range of time, as shown in Fig 3.7b, where the aggregate sizes varies from $N_{agg} = 20$ to 50 with a constant volume fraction $\phi = 10\%$. The rigid aggregates size is limited to $N_{agg} = 50$ owing to the difficulties to generate large rigid aggregates $N_{agg} > 50$. As expected, the large aggregates can lead to the slowing down of the dynamics when compared to small aggregates. However, for the flexible aggregates system, no change occurs in the relaxation dynamics at short times, which may be related to the soft nature of the aggregates, while the rigid aggregates exhibit the reinforcement effect in the whole range of time, which may be owing to their solid spatial structure.

Entangled polymer The flexible aggregates exhibit a similar size effect like that highlighted previously with a simple viscous fluid. This is shown in Fig 3.8a, where the volume

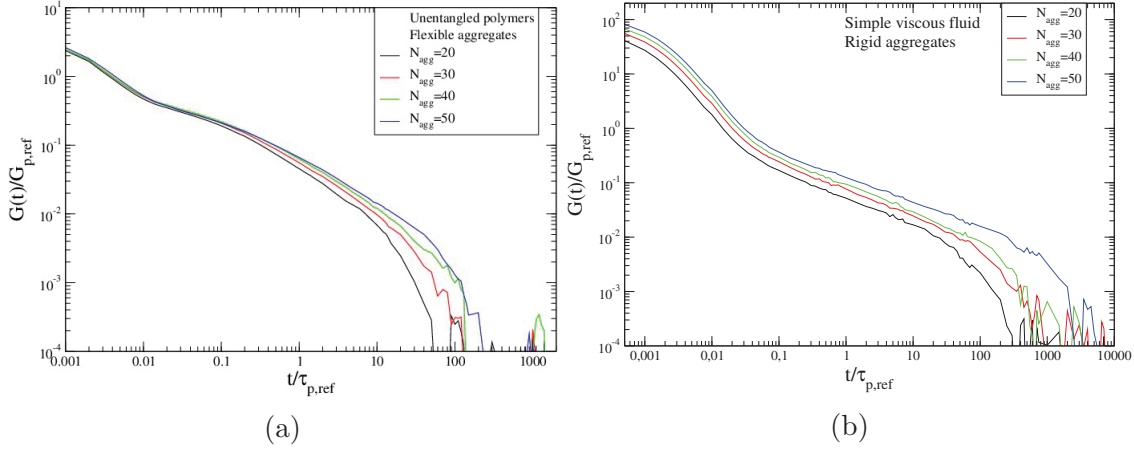


Figure 3.7: Effect of aggregate size N_{agg} of (a) flexible aggregates and (b) rigid aggregates in a simple viscous fluid, with a fixed volume fraction $\phi = 10\%$.

fraction of aggregates is fixed to 10% and the aggregate sizes N_{agg} vary from 20 to 50. For the rigid aggregates, reinforcement occurs on the stress relaxation modulus $G(t)$ along the whole range of time, as shown in Fig 3.8b, where the volume fraction and the polymer matrix are the same as these for the flexible aggregates. The reinforcement for the rigid aggregates can be described as an increasing plateau of the stress relaxation modulus $G(t)$ at short times and the slow dynamics at long times, which is more pronounced than for the flexible aggregates. The reinforcement is affected by the aggregate size N_{agg} but the effect may not be strong enough to change the reinforcement mechanism, at least within the limit of $N_{agg} \leq 50$ and with volume fraction 10%.

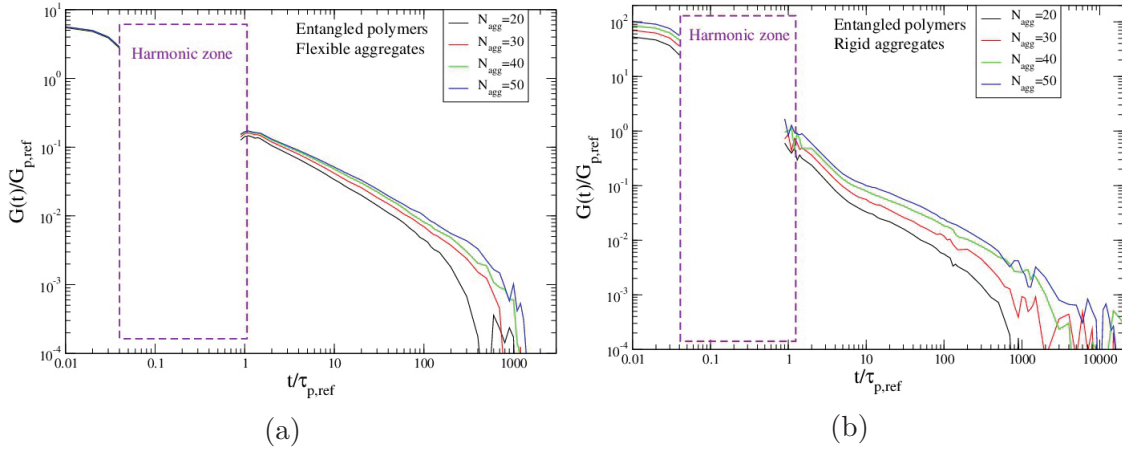


Figure 3.8: Effect of the aggregate size N_{agg} of (a) flexible aggregates and (b) rigid aggregates in an entangled polymer matrix ($G_p = G_{p,ref}$ and $\tau_p = \tau_{p,ref}$), with a fixed volume fraction $\phi = 10\%$.

3.2.4 Effect of primary particle size

As mentioned in the section 2.2.5, the value of the primary particle size d enters the stress units in simulations. This results from the fact that the unit of pressure in the simulation is related to the particle diameter d , which sets also the unit of length, and can be written as $k_B T/d^3$. In practice, this amounts to change the value of the plateau modulus $G_{p,0}$ appearing in the relaxation modulus of the polymer matrix, see Eq 3.12. Obviously,

$G_{p,0}$ corresponds physically to a fixed value 0.5 MPa, specific to our choice of the polymer matrix. In the simulation, however, the reduced plateau modulus $G_{p,0}$ is expressed in units of $k_B T/d^3$, and consequently may be different from 1. Hence, to change the value of d , we change the reduced value of $G_{p,0}$.

To illustrate this, consider the conversion between the pressure unit in simulations and in experiments as follows:

$$G_{p,0} = 1 k_B T/d^3 \sim G_{p,ref} = 0.5 \text{ MPa}. \quad (3.13)$$

Here, k_B is the Boltzmann constant and the temperature is fixed to the room temperature $T = 300 \text{ K}$, the reference unit of stress of the polymer matrix can be 0.5 MPa, which is typical value for polybutadiene matrix. It is readily to show that the effective particle diameter in simulations d corresponds then to 2.02 nm in experiments. If we redefine this conversion relationship between:

$$G_{p,0} = 1000 k_B T/d^{*3} \sim G_{p,ref} = 0.5 \text{ MPa}. \quad (3.14)$$

Hence, when all the other parameters are fixed, the pressure unit should be 1000 times smaller than before to maintain the conversion, which leads to a 10 times larger particle diameter $d^* = 10d \sim 20.2 \text{ nm}$.

We have used this strategy to evidence the effect of the primary particle size for the rigid aggregates in an entangled polymer matrix, as shown in Fig 3.9a. The plateau value $G_{p,0}$ varies from $G_{p,0} = G_{p,ref}$ to $G_{p,0} = 100G_0 = G_{p,ref}$, where $G_0 = k_B T/d^3$ is the pressure unit in simulations. This leads to the various particle diameters ranging from 2.02 nm, 4.36 nm to 9.39 nm. When the particle diameter increases, there is a clear decrease of the stress relaxation modulus $G(t)$ at short times and a slight shortening of the slow relaxation at long times. We can include that reinforcement increases for small particles, which may originate from the fact that the large particles diameter may reduce the interface between the polymer and the filler. The same trend has been observed in the ref [40], where the reinforcement decreases with increasing particle diameter.

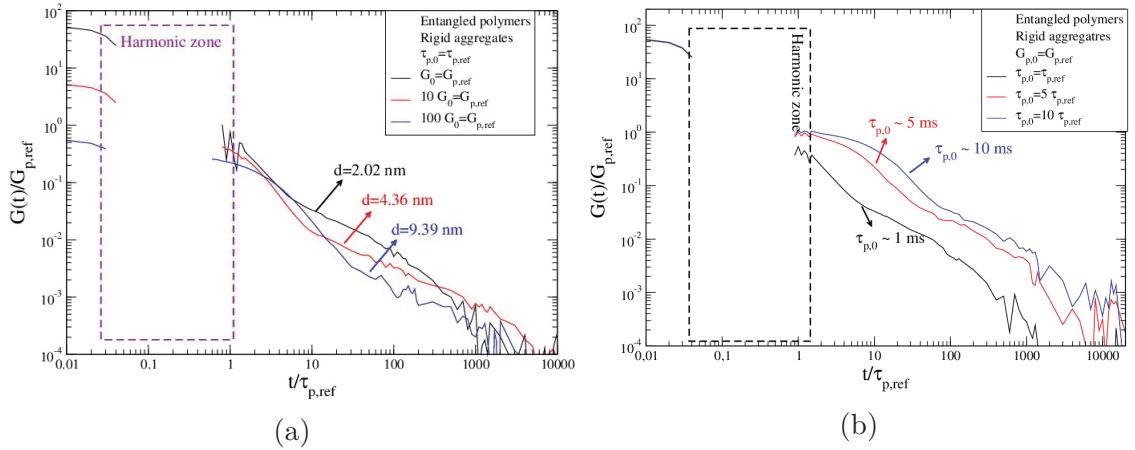


Figure 3.9: Effect of (a) particle size d and of (b) the relaxation time τ_p for rigid aggregates in entangled polymer matrix, with aggregate size $N_{agg} = 20$ and a volume fraction 10%.

3.2.5 Effect of polymer matrix relaxation time

Since the polymer matrix has a viscoelastic kernel which is mono-mode in the present model (see Eq 3.12), the polymer matrix can influence the rheology of the composites

through two parameters, namely the plateau modulus $G_{p,0}$ and the terminal relaxation time $\tau_{p,0}$.

We have studied the effect of the polymer matrix relaxation time τ_p on the stress relaxation modulus $G(t)$ of rigid aggregates systems in entangled polymer matrix, as shown in Fig 3.9b. The relaxation time τ_p varies from $\tau_{p,0} = \tau_{p,ref}$ to $\tau_{p,0} = 10\tau_{p,ref}$ and the plateau modulus $G_{p,0}$ is a constant, for rigid aggregates system with aggregate size $N_{agg} = 20$ and volume fraction 10%. $\tau_{p,ref}$ is the reference relaxation time of the polymer matrix, which is considered to be 1 ms in a real system. We conclude that the polymer relaxation time τ_p show influence on the stress relaxation modulus $G(t)$ at intermediate and long times via the slow relaxation dynamics. Therefore, reinforcement in these systems should also depend on the terminal relaxation time of the polymer matrix.

3.2.6 Effect of aggregates polydispersity

Finally, we discuss here the effect of the aggregates polydispersity on the rheological properties of the model composites. Note that, as shown in Fig 2.11, the highest attainable volume fraction of monodisperse rigid aggregates is 17% with small aggregates $N_{agg} = 20$ and for polydisperse rigid aggregates, one can reach 18% with small aggregates number in system containing $N_a = 100$ and 200 aggregates.

As mentioned before, the distribution of size of polydisperse aggregates can be generated via the empirical formula, expressed in Eq 2.1, here, we have fixed the parameters as $a = 2$ and $b = 10$. Then, the corresponding mean aggregate size and the most frequent aggregate size should be $\langle N_{agg} \rangle = 30$ and $N_{agg,max} = 20$, respectively. This corresponds to a size polydispersity around 30%.

The comparison of the stress relaxation modulus $G(t)$ of the monodisperse and the polydisperse rigid aggregates with entangled polymer matrix, $G_{p,0} = 100G_0 = G_{p,ref}$ corresponding to particle diameter $d = 9.39$ nm and $G_{p,0} = G_0 = G_{p,ref}$ corresponding to particle diameter $d = 2.02$ nm, both with $\tau_{p,0} = \tau_{p,ref}$, is shown in Fig 3.10, where all the systems share a constant volume fraction of aggregates $\phi = 10\%$ and the monodisperse systems have an aggregate size $N_{agg} = 20$ and 30, which corresponds respectively to the mean aggregate size and the most probable aggregate size in the polydisperse system. We can see that the $G(t)$ of the polydisperse system is slightly higher than both $G(t)$ characterizing the monodisperse systems having respectively the aggregate size 20 and 30. Thus, reinforcement in the polydisperse system should be higher as compared to the monodisperse systems having either the mean aggregate size or the most probable size of the polydisperse system. This may be caused by a few large aggregates ($N_{agg} > 30$) in the polydisperse system, which can enhance the $G(t)$ at intermediate times and slow-down the dynamics at long times, thus contributing to increase the reinforcement.

3.2.7 Summary: Reinforcement

Stress relaxation modulus

As shown in Fig 3.9, the fillers in entangled polymer matrix exhibit reinforcement evidenced here by the stress relaxation modulus $G(t)$, especially at long times, when compared to the implemented polymer matrix here. This is mostly due to the slow relaxation dynamics at long times for rigid aggregates.

Effective viscosity

The reinforcement on the stress relaxation modulus $G(t)$ depends on the nature of fillers, the volume fraction of filler and the aggregate size has been investigated in the previous sections. As well as the stress relaxation modulus, the viscosity of system can also disclose

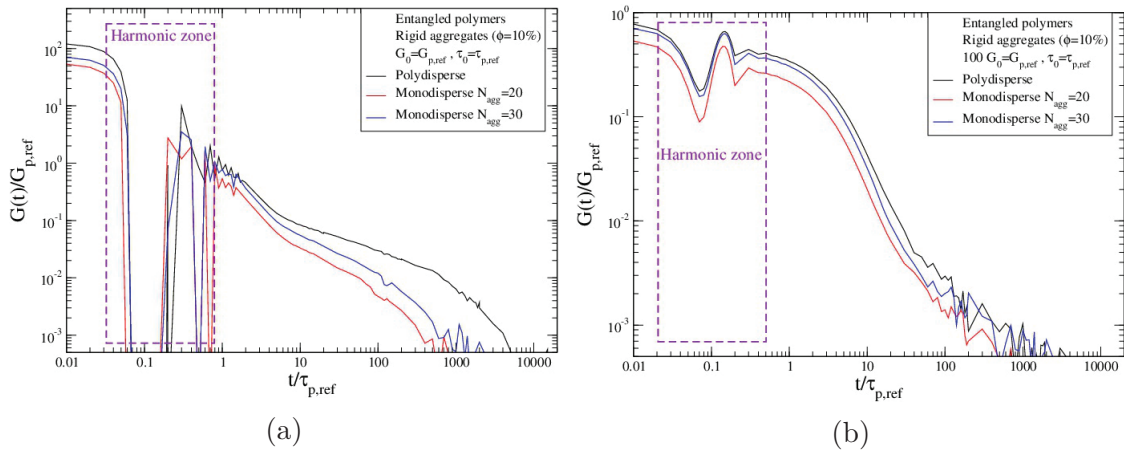


Figure 3.10: Comparison between the monodisperse and the polydisperse rigid aggregates systems with entangled polymers (a) $d = 2.02$ nm and (b) $d = 9.39$ nm at a fixed volume fraction $\phi = 10\%$.

the reinforcement effect on the rheological properties. As defined in Eq 1.29, the shear viscosity η of filled polymer matrix can be written as the integration of the stress relaxation modulus $G(t)$ over time,

$$\eta = \int_0^{\infty} G(t) dt. \quad (3.15)$$

In practice, the relaxation function $G(t)$ has been integrated over the whole range of time, [except the harmonic zone](#). We have, however, discarded the noise part at long times and the harmonic zone at short times.

As shown in Fig 3.11a, the viscosity of aggregates-filled polymer matrix systems increases with the volume fraction of aggregates. Strikingly, the viscosity of the systems are orders of magnitude larger than predictions of the Einstein-Smallwood law in Eq 1.12. Both the flexible and the rigid aggregates in either a simple viscous fluid or an entangled polymers display a higher reinforcement factor. Furthermore, the rigid aggregates exhibit a more pronounced effect of reinforcement than flexible aggregates.

As well as the volume fraction of aggregates, we have investigated the viscosity of the composites as a function of the aggregate size N_{agg} , as shown in Fig 3.11b. The viscosity of composites exhibits a linear relationship on the aggregates size for the case of flexible aggregates with both an entangled polymers matrix and a simple viscous fluid, which is probably due to their soft nature, akin to star polymers. For rigid aggregates, we clearly see a change in the reinforcement regime when the aggregates increase their size, for instance, the viscosity increases substantially when $N_{agg} > 40$ with a simple viscous fluid and enhances slightly when $N_{agg} > 20$ with an entangled polymer matrix. These results, confirm again the huge increase in reinforcement for aggregates having large size. Also, it is clear that rigid aggregates display higher levels of reinforcement than flexible aggregates.

3.3 Slow dynamics

In the previous section 3.2.1, the effect of filler type on the stress relaxation modulus $G(t)$ has been examined for the individual nanoparticles and for both the flexible and the rigid aggregates in entangled polymers, as shown in Fig 3.3b. All three types of fillers share the same volume fraction $\phi = 10\%$ and both the flexible and the rigid aggregates have the same aggregate size $N_{agg} = 50$. Both types of aggregates exhibit reinforcement on the stress relaxation modulus at long times, and we have evidenced a slow dynamics, as compared to individual nanoparticles.

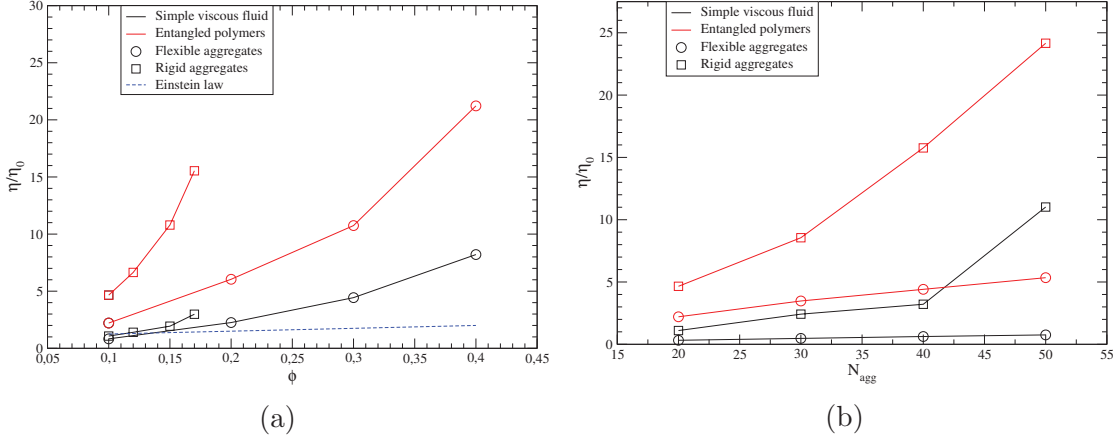


Figure 3.11: Viscosity of aggregates-filled polymer matrix as a function of (a) the volume fraction of aggregates ϕ (with a constant aggregate size $N_{agg} = 20$) and (b) the aggregate size N_{agg} (with a constant volume fraction $\phi = 10\%$), in both a simple viscous fluid and an entangled polymer matrix. The dashed line represents the Einstein-Smallwood law Eq 1.7.

In this section, the slow filler dynamics has been investigated via several physical observables, including the mean-square displacement, the dynamic structure factor and the orientation autocorrelation function, which are intended to understand the link between the microscopic motion at the scale of the nanoparticles and macroscopic mechanical reinforcement. For the sake of focusing on the motion of the aggregates, small aggregates have been studied here which may reduce the influence of the aggregate size. As shown in Fig 3.12a, both the flexible and the rigid aggregates display reinforcement on the stress relaxation modulus $G(t)$ when compared to the individual nanoparticles, and the aggregate size here is unique $N_{agg} = 20$ and the volume fraction of fillers is fixed as $\phi = 10\%$ with an entangled polymer matrix. We remark that the long time relaxation dynamics is almost the same for the two types of aggregates. The rigidity of the aggregates does not play an important role here probably because the aggregates are small, $N_{agg} = 20$.

3.3.1 Diffusion coefficient

The mean-square displacement (MSD) is a useful quantity to characterize the motion of the particles and is defined as follows:

$$MSD(t) = \langle (\mathbf{R}(t) - \mathbf{R}(0))^2 \rangle = \frac{1}{N} \sum_{n=1}^N (\mathbf{R}_n(t) - \mathbf{R}_n(0))^2, \quad (3.16)$$

where N is the total number of particles and $\mathbf{R}_n(t)$ is the position vector of particle n at time t . The diffusion coefficient D in 3D is related to the mean-square displacement as follows [86],

$$\lim_{t \rightarrow \infty} MSD(t) = 6Dt. \quad (3.17)$$

We have quantified the long time dynamics through the diffusion coefficient for all three types of fillers, as shown in Fig 3.12b. The slopes of curves represent the diffusion coefficient of particles and the data have been collected from the same simulations shown in Fig 3.12a. It is important to notice that the mean-square displacement of the aggregates here are not that of the mass center of aggregates but [the average value of all the nanoparticles in an aggregate](#). Owing to the presence of the harmonic zone and the transition state at short and intermediate times, the diffusion coefficient should only be computed from long times,

$t > 1000$ in Fig 3.12b. The diffusion coefficient for the individual nanoparticles at long times ($t > 1000\tau_{p,ref}$) is near 0.0909 and these for the flexible and the rigid aggregates are 0.00324 and 0.00266 (in units of $d^2/\tau_{p,ref}$), respectively. Obviously, the individual nanoparticles have a much larger diffusion coefficient when compared to both types of aggregates, which is a sign of the emergence of slow dynamics for the two types of aggregates considered.

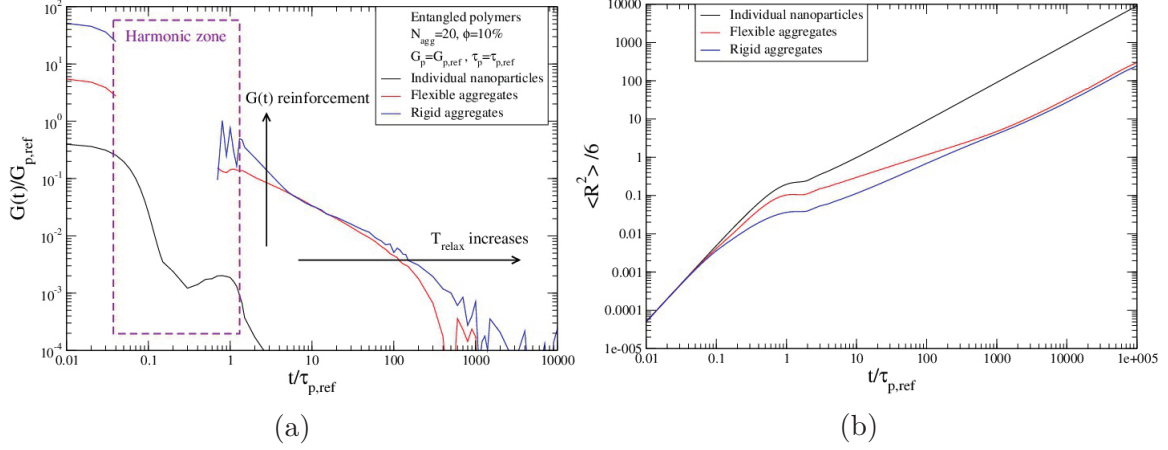


Figure 3.12: (a) Stress relaxation modulus $G(t)$ of aggregates compared to individual nanoparticles. All the systems have the same volume fraction of filler, $\phi = 10\%$, and the aggregates have the unique size $N_{agg} = 20$. (b) The mean-square displacement (MSD) calculated for the systems shown in the left figure.

3.3.2 Orientation of aggregates

The orientation of the aggregates may disclose the slow dynamics at long times since the aggregates consist of primary particles and their motions may be decomposed in the diffusion of the center of mass, rotation around the center of mass and deformation, the latter one being relevant only for the flexible aggregates system. In the linear regime that we have discussed up to now, simulations occur at equilibrium. Hence, the evolution of the orientation of aggregates may be measured by the time correlation of the orientation vector of the aggregates. The orientation vector of an aggregate i can be defined in a simple way, as a vector joining the center of mass (position $\mathbf{R}_{i,c.m.}$) to the furthest particle from the mass center (position $\mathbf{R}_{i,fur}$)

$$\mathbf{u}_i(t) = \mathbf{R}_{i,fur}(t) - \mathbf{R}_{i,c.m.}(t). \quad (3.18)$$

Then the evolution of the orientation of the aggregates can be written as follows:

$$C_{i,or}(t) = \langle \mathbf{u}_i(t) \cdot \mathbf{u}_i(0) \rangle, \quad (3.19)$$

where $C_{i,or}(t)$ is the time correlation of the orientation vector of aggregate i at time t .

As shown in Fig 3.13a, the time correlations of the orientation vector of both the flexible and the rigid aggregates display a slow relaxation regime. More precisely, we can define a final relaxation times τ_{relax} for the flexible and the rigid aggregates, when the autocorrelation function has reached $1/e$ of its initial value. These times are found to be around $\tau_{relax} = 150$ and $580 \tau_{p,ref}$, respectively, which are the average value over all the aggregates in simulation. The data have been collected from the same simulations shown in Fig 3.12a. The long relaxation time of the orientation of the aggregates is comparable with the relaxation time corresponding to the long time decay of the stress relaxation modulus $G(t)$ shown before.

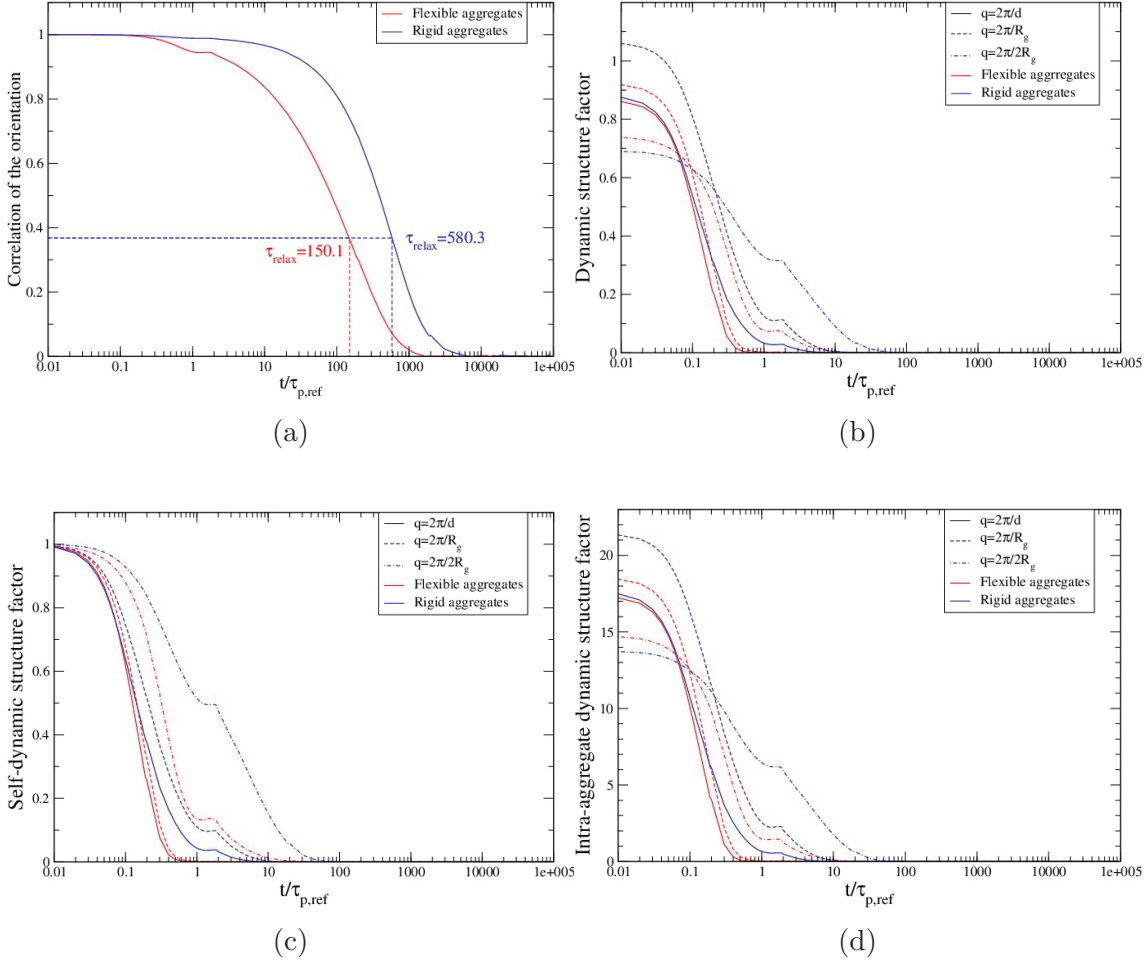


Figure 3.13: (a) Normalized time correlation of orientation vector, (b) Dynamic structure factor, (c) self dynamic structure factor and (d) intra-aggregates dynamic structure factor of both the flexible and the rigid aggregates with a series of wave vectors $q = 2\pi/d$, $2\pi/R_g$ and $2\pi/2R_g$, where R_g is the radius of gyration of the aggregates. The volume fraction is $\phi = 10\%$ and the aggregate size is $N_{agg} = 20$.

3.3.3 Dynamic structure factor

Dynamic structure factor The dynamic structure factor is an other observable that characterizes the microscopic dynamics of the nanoparticles. The dynamic structure factor is based on the density field of the whole system $\rho(\mathbf{q}, t) = \sum_{m=1}^N \exp(-i\mathbf{q} \cdot \mathbf{r}_m)$, where N is the total number of particles, \mathbf{q} and \mathbf{r}_m is the wave vector and the position vector of particle m , respectively, then it can be written as follows:

$$S_{dsf}(\mathbf{q}, t) = \frac{1}{N} \langle \rho(\mathbf{q}, t) \rho^*(\mathbf{q}, 0) \rangle. \quad (3.20)$$

Fig 3.13b shows that the dynamic structure factor of both the flexible and the rigid aggregates calculated for a series of wave vectors $|\mathbf{q}| = 2\pi/d$, $2\pi/R_g$ and $2\pi/2R_g$. It is obvious that the dynamic structure factor has a much smaller relaxation time than that of the stress relaxation modulus $G(t)$, in Fig 3.12a, or that of the orientation of aggregates, in Fig 3.13a. Since the dynamic structure factor is associated to the global density field, this rapid relaxation process may indicate that the global configuration of particles does not change slowly and the local dynamics of particles may be relatively faster than the rotation of the aggregates.

Self dynamic structure factor To subtract the contribution of collective particle motion in the dynamic structure factor, the self dynamic structure factor is intended to characterize the self motion of the nanoparticle. It can be defined as the time correlation of the local density as below,

$$S_{sdsf}(\mathbf{q}, t) = \frac{1}{N} \left\langle \sum_{m=1}^N \rho_m(\mathbf{q}, t) \rho_m^*(\mathbf{q}, 0) \right\rangle, \quad (3.21)$$

where $\rho_m(\mathbf{q}, t) = \exp(-i\mathbf{q} \cdot \mathbf{r}_m(t))$ is the local density of particle m at time t . Being different from the dynamic structure factor, the self dynamic structure factor represents the relaxation of the local density. As shown in Fig 3.13c, both the flexible and the rigid aggregates exhibit a rapid relaxation process for the series of wave vectors q .

Intra-aggregate dynamic structure factor Since the orientation of the aggregates displays a slow relaxation, the intra-aggregates dynamic structure factor may unveil the relationship between the local density field and the motion of the aggregates. The intra-aggregates dynamic structure factor is defined by the density field of single aggregate ρ_m ,

$$S_{iadsf}(\mathbf{q}, t) = \frac{1}{N_a} \left\langle \sum_{m=1}^{N_a} \rho_m(\mathbf{q}, t) \rho_m^*(\mathbf{q}, 0) \right\rangle, \quad (3.22)$$

where N_a is the total number of aggregates and $\rho_m(\mathbf{q}, t) = \sum_{n=1}^{N_{agg,m}} \exp(-i\mathbf{q} \cdot \mathbf{r}_n(t))$ is the local density of aggregate m at time t , $N_{agg,m}$ is the total number of particles contained in an aggregate m . This observable should indicate the change in the dynamics of the aggregates due to the interaction between the aggregates or the [interaction](#)/inneraction within an aggregate. As shown in Fig 3.13d, the intra-aggregates dynamic structure factor displays a rapid relaxation process even with a series of wave vectors, with relaxation times comparable to those computed from the other structure factors.

To conclude this section, the slow dynamics evidenced in the stress relaxation modulus for both the flexible and the rigid aggregates can be related to the slow rotation of the aggregates as probed in simulations at equilibrium. Moreover, we have seen that the global density field, the local particle density field and the local aggregate density field relax all relatively fast as compared to the aggregate rotation, as inferred from the three dynamic structure factors calculated. This indicates that the slow dynamics evidenced in the stress relaxation modulus $G(t)$, which can induce reinforcement at long times, for aggregates may occur when the local dynamics of the particles or aggregates are relaxing relatively fast.

Conclusion

We have characterized the rheological properties of polymer matrix filled by small fillers. The effect of the key parameters, including the filler volume fraction, the filler size and morphology and the rheology of the polymer matrix has been systematically analyzed. Both the flexible and the rigid aggregates exhibit a remarkable reinforcement in the stress relaxation modulus $G(t)$ as compared to the individual nanoparticles. This effect is evidenced for both simple viscous fluid and entangled polymer matrix. The same effect of filler type also appears on the dynamic moduli, the storage modulus $G'(\omega)$ and the loss modulus $G''(\omega)$. The volume fraction of fillers has been proven to be a key parameter in enhancement of the mechanical properties of filled hybrid system. The corresponding effect is displayed as a reinforcement linear proportional to the weak volume fractions of aggregates, this linearity may be caused by the weak volume fraction of filler and the repulsive interaction between fillers. When the volume fraction of aggregates is large, the aggregates system exhibits a change of reinforcement regime, this effect is more pronounced for the rigid aggregates

($\phi > 15\%$) than the flexible aggregates ($\phi > 30\%$), as shown in Fig 3.11a. The aggregate size can exhibit different reinforcement levels according to the nature of the aggregates. The effect on the stress relaxation modulus $G(t)$ occurs only at long times for the flexible aggregates and in the whole range of time for the rigid aggregates.

The rheology of the polymer matrix has two main parameters: the plateau modulus and the relaxation time. Large nanoparticles may reduce the reinforcement, which may decrease the effective effect of the polymer chains around the nanoparticles. This can be related to the phenomenon observed in ref [40], which is attributed to the reduction of the interface between the polymer and the interface for big nanoparticles. Meanwhile, the effect of relaxation time, related to the effect of the mass of polymer chain M_w , also play an important role in the reinforcement at long times.

In order to understand the reinforcement mechanisms on the stress relaxation modulus $G(t)$, displayed by the aggregates systems, the slow dynamics of aggregates at long times has been investigated. We have seen that the diffusion coefficient of the nanoparticles in both types of aggregates decreases significantly as compared to the diffusion coefficient of the individual nanoparticles. From a microscopic point of view, the aggregates in the simulations do not rotate rapidly, instead, the correlation of the orientation of the aggregates displays a slow relaxation process. Nonetheless, the local and collective dynamics of either the nanoparticles or the aggregates are orders of magnitude faster than rotational motion of the aggregates, as one can be inferred from the different structure factors studied here. This indicates that the global configuration of all aggregates may evolve slowly, specifically the translation and the rotation of aggregates.

The distribution of the aggregate size can have a relatively important effect in the mechanical reinforcement of filled polymer system. Polydisperse rigid aggregates systems exhibit reinforcement levels comparable to the reinforcement displayed by the monodisperse systems having the mean aggregate size and the most frequent aggregate size of the polydisperse systems. The comparable levels of reinforcement may be due to the relatively small volume fraction, and large nanoparticle diameter considered here. However, generating mono and polydisperse rigid aggregates with relatively high volume fraction is challenging.

We discuss finally briefly the experimental relevance of our simulation results. The existence of long relaxation times in the stress relaxation modulus of filled polybutadiene has been evidenced experimentally in [67]. We interpret the long times appearing in $G(t)$ as the existence of aggregates in the filled samples studied in [67]. Also, Figure 7 in [67] shows that for intermediate frequencies, reinforcement is almost independent on the molecular mass M_w of the polymer matrix. The mechanisms of reinforcement that we discuss here should be relevant to this regime. Conversely, at lower frequencies, reinforcement becomes dependent on M_w . We anticipate that in this latter regime, polymer bridging should control the rheological response of the system, leading to another relaxation mode with a M_w dependence. The possibility of the polymer chains to do some bridges between nanofillers should be considered in future extensions of the model.

Appendix: Computing the stress autocorrelation function in practice

The stress relaxation modulus $G(t)$ is defined as the time correlation of the shear stress, as presented in Eq 3.7. Here we discuss the different ways to calculate the time correlation functions in the simulations.

Basic method This method is based on the definition of the stress relaxation modulus by the Green-Kubo approach, in Eq 3.7. The simplest method is to keep in memory all the stress components at all times during the simulations. This requires an enormous

memory space for the storage, which may require enormous computation costs and slow-down computational performance.

FFT method The time correlation of an observable can be also called the auto-correlation, which can be calculated by Fourier transform, in practice, the fast Fourier transform (FFT) is a useful technique. For instance, the auto-correlation $S(t)$ of the function $f(t)$ can be defined as below,

$$S(t) = \langle f(t+s)f(s) \rangle, \quad (3.23)$$

where $\langle \dots \rangle$ is the ensemble average. The auto-correlation can be written in a simple formula in Fourier space,

$$FFT[S(t)] = FFT[\langle f(t+s)g(s) \rangle] = \tilde{F}(\omega)\tilde{F}^*(\omega), \quad (3.24)$$

where $\tilde{F}(\omega) = FFT[f(t)]$ is the Fourier transform of $f(t)$. Then it is readily to calculate the auto-correlation by the inverse Fourier transform (*IFFT*) of its corresponding value in Fourier space,

$$S(t) = IFFT[\tilde{F}(\omega)\tilde{F}^*(\omega)]. \quad (3.25)$$

Compared to the basic method, the FFT method is fast and there is almost no differences between the basic method and the FFT method [88]. However, the FFT method still requires to record the stress along the whole simulation, which may lead to some storage problems. This will be resolved in the following method.

Order-n algorithm The Order-n algorithm is intended to measure the correlations over different time scales [88]. In practice, there are several parameters: the block scale N_{scl} is the time scale to calculate an average value which is the new element at the following high level, N_{lv} is the maximum number of levels and N_{elem} is the maximum number of elements at one level.

At the base level 0, there are the original instantaneous data, for instance, the stress $\sigma(t)$ at time t . The j -th element $\sigma_j^{(i)}$ at level i ($i > 0$) represents the average value with time scale $\Delta t^{(i)} = N_{scl}^i \Delta t$ calculated from the j -th block of elements at level $i-1$, and so on, as shown in the equations below:

$$\sigma_j^{(i)} = \frac{1}{N_{scl}} \sum_{k=j}^{j+N_{scl}} \sigma_k^{(i-1)} = \frac{1}{N_{scl}^i} \sum_{k=(j-1)N_{scl}^i+j}^{jN_{scl}^i+j} \sigma_k^0, \quad (j = 1, 2, \dots, N_{elem} - N_{scl}) \quad (3.26)$$

where $\sigma_j^{(i)}$ is the j -th element in level i and σ_k^0 is the $(k - (j-1)N_{scl}^i)$ -th element at base level 0. A schematic illustration is shown in Fig 3.14, in which the new element at high level is the mean value of the newest N_{scl} elements at low level, such as the element $\sigma^{(1)}(n)$ at level 1 is the mean value of the elements from $\sigma((j-1)n+1)$ to $\sigma(jn)$, where n here is the block scale N_{scl} and jn represents the time. At each level, the elements will be transferred towards the left side if there is a new stress element generated and deployed from the right side. Once the new elements number reaches the block scale N_{scl} , a new element at the next higher level should be calculated.

The stress relaxation modulus $G(t)$ can be constructed in a similar table as the stress table, as shown in Fig 3.15, in which the elements at each level are no longer the average value from the elements at lower level. The j -th element $G_j^{(i)}$ at level i , which represents the $G(t)$ at time scale $j\Delta t^{(i)}$, can be calculated directly from the correlation of the corresponding stress elements at the same level, as shown in the equation below,

$$G_j^{(i)} = \frac{V}{k_B T} \times \left\langle \sum_{k=1}^{N_{elem}-j} \sigma_{k+j}^{(i)} \sigma_k^{(i)} \right\rangle, \quad (3.27)$$

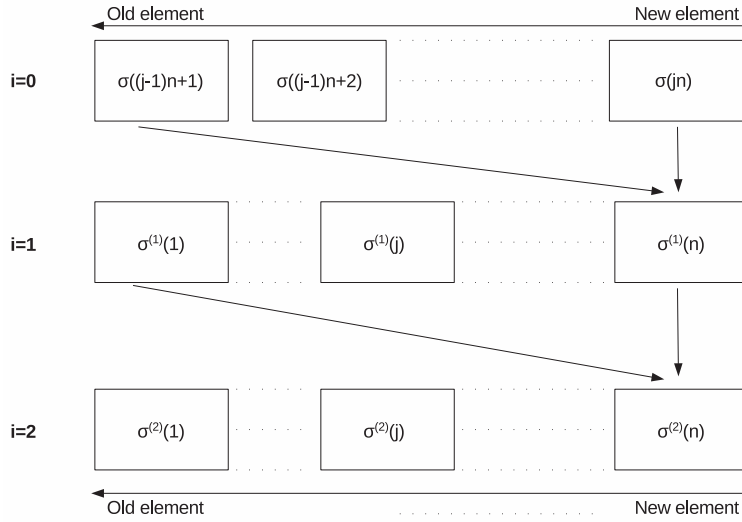
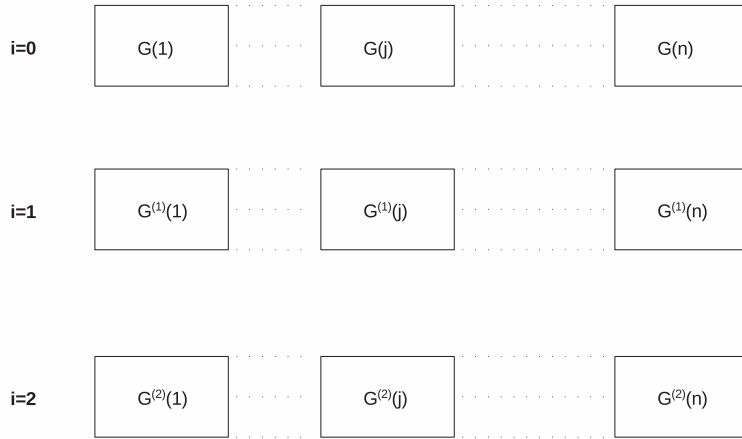


Figure 3.14: The stress table for the Order-n method.

Figure 3.15: $G(t)$ table for the Order-n method.

where $\sigma_k^{(i)}$ is the k -th element in the same level i and $\langle \dots \rangle$ is the average symbol over the number of stress correlations.

The Order-n algorithm is a fast and accurate technique to compute the auto-correlation and involves calculation time around $NN_{scl}/(N_{scl}-1)$, while the FFT method and the basic method may require a computation time near $N \log(N)$ and $O(n^2)$, respectively. Obviously, the advantage of the Order-n method is a technique to calculate the auto-correlation on-the-fly with reasonable memory resources [88].

Therefore, the Order-n method has been the principal technique to calculate the stress relaxation modulus $G(t)$. Due to the nature of the Order-n algorithm, the resulting data of the stress relaxation modulus $G(t)$ are not separated by the unique time delay between the elements at different levels. Thus, it requires to complete the data of $G(t)$ with a unique time scale in order to calculate the dynamic moduli $G'(\omega)$ and $G''(\omega)$, via the Fourier transform. To do so, we used linear interpolation in log-log scale.

 Nonlinear rheology: simulations and results

 Contents

4.1	Rheology in nonlinear regime	68
4.1.1	Method in practice	68
4.1.2	Storage and loss modulus	70
4.2	Influence of aggregates properties	71
4.2.1	Effect of filler type	71
4.2.2	Effect of filler volume fraction	72
4.2.3	Effect of aggregate size	73
4.2.4	Effect of polydispersity	74
4.3	High order harmonics	75
4.3.1	Dynamic moduli	75
4.3.2	Shear stress	76
4.4	Filler behavior under LAOS	77
4.4.1	Gyration tensor	77
4.4.2	Results	77
4.5	History-dependent LAOS	80
4.5.1	Single shear cycle	81
4.5.2	Long time relaxation	81
4.5.3	Multiple shear cycles	82
4.6	Aggregates with attractive interaction	83

Introduction

A system submitted to a large deformation will often exhibit a non-linear response. In this chapter, we study the non-linear rheology of our model composites. We use large

amplitude oscillatory shear (LAOS), where a sinusoidal deformation of fixed amplitude is imposed. We saw in section 1.2.3 that nonlinear behaviors can be classified into four types. We show below that our model composites pertain to the first type, where the dynamic moduli are constant in the linear regime and start decreasing monotonously with the shear deformation amplitude. We also study the history dependence of rheology by performing multiple cycles in which the shear amplitude is first increased step by step and then reduced back to its initial value. Both the storage and the loss modulus exhibit similar responses to these cycles, and we discuss how this behavior relates to the orientation of aggregates. Finally, we also present some preliminary results with attraction between aggregates, and show that they open interesting perspectives.

4.1 Rheology in nonlinear regime

4.1.1 Method in practice

Lees-Edwards boundary conditions

The Lees-Edwards boundary conditions are a widely used technique to generate the shear flow in molecular dynamics simulations [89, 88]. As shown in Fig 4.1, the simulation box is the grey middle one and is surrounded by its images via the periodic boundary conditions. The goal is to simulate a steady shear, in which the deformation amplitude varies with a constant shear rate and to generate a linear profile of velocity. The upper layer (box B, C, D) and the bottom layer (box F, G, H) displace towards opposite directions while the middle layer remains static.

This method can simulate the non-equilibrium process when implementing shear deformation, which requires a propagation time to establish the desirable velocity profile proportional to the shear rate and let the system reach a stationary state. However, this propagation time may cause problem in simulations under oscillatory shear, in which the shear deformation varies constantly and periodically, so does the velocity profile. This constraints also the maximal frequency ω to be considered in oscillatory shear, as it should be less than $2\pi/T_s$ where $T_s = L/2c_s$ is the time taken by sound waves to travel from the boundaries to the center of the simulation box of size L . We have done a number of tests with oscillatory shear using Lees-Edwards boundary conditions and found that none of them yield satisfactory results. Apparently, the sound velocity is too small to establish the instantaneous velocity profile at each time. As a result, we consider that the Lees-Edwards boundary conditions are not the proper algorithm to compute the shear deformation in the present model.

SLLOD algorithm We have implemented the SLLOD algorithm, which is useful to simulate homogeneous shear flow [90], in which the transient process to establish the linear velocity profile is considered to occur only on a very short time scale. This algorithm contains the periodic boundary conditions and the instantaneous velocity profile, as shown in Fig 4.2. An additional velocity, \mathbf{u}_{ext} , is implemented directly upon particle according to the shear velocity profile that we want to establish. The additional velocity is $u_{ext}(y) = \dot{\gamma}y$ in case of a steady shear with a given shear rate $\dot{\gamma}$. The equation of motion in the SLLOD algorithm can be written as follows:

$$\dot{\mathbf{q}} = \frac{\mathbf{p}}{m} + \mathbf{q} \cdot \nabla \mathbf{u}_{ext}, \quad (4.1)$$

$$\dot{\mathbf{p}} = \mathbf{F} - \mathbf{p} \cdot \nabla \mathbf{u}_{ext}, \quad (4.2)$$

where \mathbf{q} is the position, $\dot{\mathbf{q}}$ and \mathbf{F} are the total velocity and the total force felt by the particle, \mathbf{p} and $\dot{\mathbf{p}}$ are the intrinsic momentum and the intrinsic force, and \mathbf{u}_{ext} is the external velocity

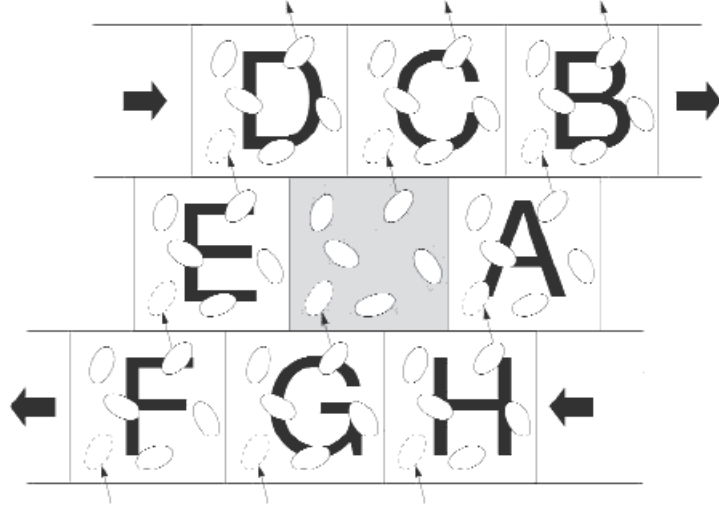


Figure 4.1: Schematic of the Lees-Edwards boundary conditions [88].

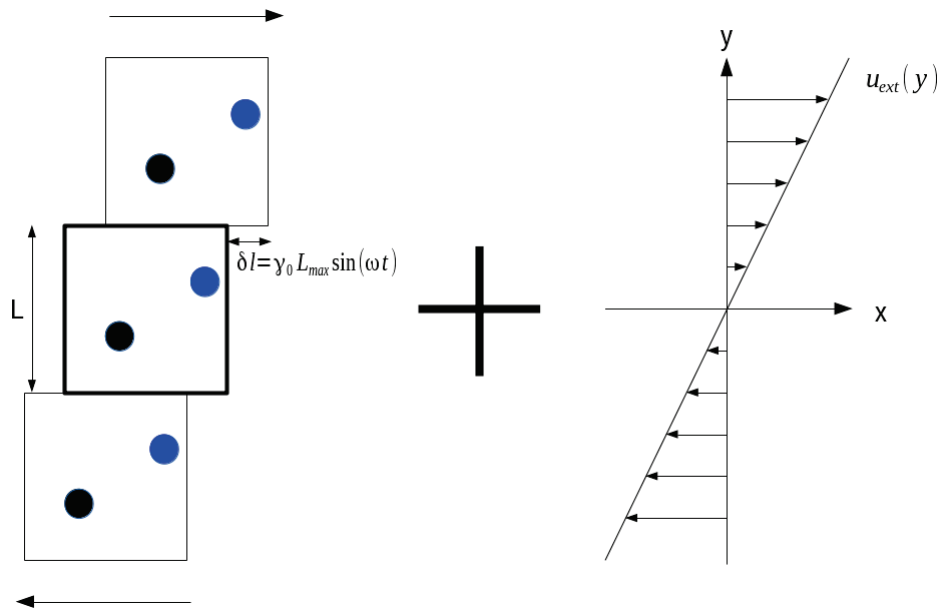


Figure 4.2: Schematic of the SLLOD algorithm.

applied on the particle [90, 91]. The external terms correspond to the external velocity which is added directly onto particle according to the instantaneous velocity profile. On the contrary, the intrinsic terms do not contain any part from the external velocity.

Thus, there are two contributions to the particle velocity, the intrinsic velocity and the external velocity. As shown in Fig 4.3, the total velocity in the x direction V_x consists of the intrinsic term $V_{intr,x}$ and the external term u_{ext} . Now, as we discuss in chapter 2, the motion of particles in an entangled polymer matrix is described by the generalized Langevin dynamics. The compatibility between the SLLOD algorithm and the generalized Langevin dynamics should therefore be discussed. The equation of motion of the generalized Langevin dynamics is expressed in Eq 2.11,

$$M \frac{dV(t)}{dt} = F_c(x(t)) - \int_0^t \Gamma(t-s)V(s)ds + F_r(t),$$

where the velocity term $V(s)$ is the relative velocity between the particle and the polymer matrix. The relative velocity here is considered to be the intrinsic velocity expressed in the

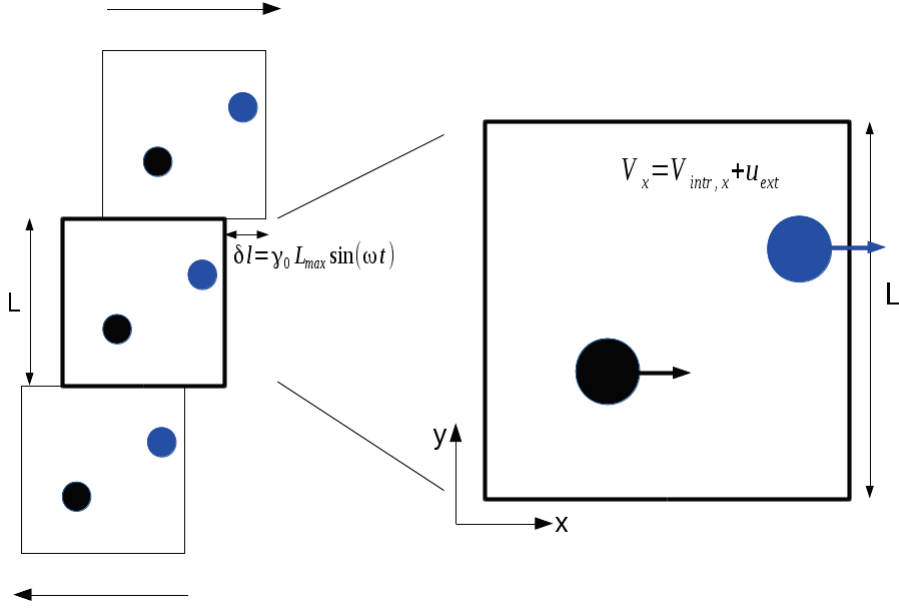


Figure 4.3: Intrinsic and external terms of velocity.

SLLOD algorithm. We consider that the polymer matrix has locally the same velocity than that of the nanoparticles. Hence, the SLLOD algorithm is compatible with the generalized Langevin dynamics, which will be applied to all the following simulations under shear.

4.1.2 Storage and loss modulus

The storage modulus G' and the loss modulus G'' in the nonlinear regime are no longer Fourier transformed from the stress relaxation modulus $G(t)$ since the Green-Kubo approach is not valid under a large shear. The alternative solution is to calculate them from the shear stress, as expressed in Eq 1.33, 1.34 and 1.35.

In an oscillatory shear, the deformation is sinusoidal with a fixed amplitude γ_0 , which induces the shear stress to be sinusoidal with a phase difference, as follows:

$$\gamma(t) = \gamma_0 \sin(\omega t), \quad (4.3)$$

$$\sigma(t) = \sum_{n \text{ odd}} \sigma_{n,0} \sin(n\omega t + \delta_n), \quad (4.4)$$

where $\gamma(t)$ and γ_0 are the shear deformation and the amplitude of shear deformation, $\sigma(t)$ and $\sigma_{n,0}$ are the shear stress and the amplitude of shear stress at n order, ω is the shear frequency and δ_n is the phase difference at n order. Note that the order number can only be odd because the stress response is assumed to be of odd symmetry [92, 93, 94]. In the linear regime, the high order harmonic terms ($n > 1$) are negligible, while they are not negligible and may influence the total shear stress when the system reaches stationary state in the nonlinear regime. The amplitudes and the phase differences in the shear stress, Eq 4.4, can be computed by the nonlinear fitting using higher order harmonic terms. The storage and the loss modulus of order n can be calculated as follows:

$$G'_n(\omega) = \frac{\sigma_{n,0}}{\gamma_0} \cos \delta_n, \quad (4.5)$$

$$G''_n(\omega) = \frac{\sigma_{n,0}}{\gamma_0} \sin \delta_n, \quad (4.6)$$

where G'_n and G''_n are the storage modulus and the loss modulus at order n . In the results shown below, all shear stresses are computed using three terms in Eq 4.4, that is $n = 1, 3$ and 5 .

The loss factor is another parameter to quantitatively determine the system responses under deformation, it is defined as the ratio between the loss modulus and the storage modulus, which is the tangent of the phase difference,

$$\tan(\delta_n) = \frac{G''_n}{G'_n}. \quad (4.7)$$

The loss factor compares the elastic and the viscous responses of the system, for instance, the system is more viscous than elastic if the loss factor is larger than 1, otherwise, the system is mostly elastic. The dependence of the loss factor on the shear amplitude can disclose the tendency of system evolution towards viscous behavior (with a positive slope) or to elastic behavior (with a negative phase), in most cases, the slope is constant in the linear regime.

4.2 Influence of aggregates properties

In this section, we describe how the nanocomposite non-linear rheology depends on the aggregates properties: filler type, volume fraction and the aggregate size. The system we consider is a nanocomposite whose matrix is always the same. It is an entangled polymer matrix whose stress relaxation modulus $G_{polymer}(t)$ can be developed in a mono-mode Prony series, as done in the previous chapter, with parameters $G_p = 100 G_0 = G_{p,ref}$ and $\tau_p = \tau_{p,ref}$. They correspond respectively to $G_p = 0.5$ Mpa and $\tau_p = 1$ ms. The primary particle diameter is set to 9.39 nm. Finally, we fix the frequency of oscillations to $\omega = \tau_{p,ref}^{-1}$, which is considered in the range of low frequency.

Note also that in the curves presented below, only the contribution from the filler is shown, the contribution from the polymer matrix is not displayed. The corresponding storage and loss moduli of the polymer matrix are readily calculated from Eq 1.39, giving $G'_p = 0.5 G_{p,ref}$ and $G''_p = 0.5 G_{p,ref}$ at the frequency ω .

4.2.1 Effect of filler type

The reinforcement effect on the dynamic moduli G' and G'' depends on the type of filler, shown in Fig 4.4a. First, we note that the results from the simulations undergoing oscillatory shear are consistent in the linear regime ($\gamma_0 < 0.1$)¹ with those calculated via the Fourier transform from the stress relaxation modulus $G(t)$ in equilibrium simulations (see chapter 3). Second, all fillers exhibit the Payne effect, where the storage and the loss moduli decrease when the shear deformation amplitude increases. For the individual nanoparticles, the reduction factor is around 2, and it appears that the storage and the loss modulus decrease simultaneously in all range of the shear deformation amplitude. This causes the corresponding loss factor to be constant with the shear deformation amplitude, as shown in Fig 4.4b. The flexible and the rigid aggregates exhibit a reduction factor around 2 and 3 on both dynamic moduli, respectively. Moreover, the loss factors of the aggregates systems present monotonous decreasing tendency with the shear deformation amplitude γ_0 , as shown in Fig 4.4b. No overshoot was seen.

Compared to the dynamic moduli of the pure polymer matrix, $G'_p = G''_p = 0.5 G_{p,ref}$, only those from the rigid aggregates present comparable values. Besides, the flexible and the rigid aggregates display substantial reinforcement on both the storage and the loss

¹Note that the loss factor of individual nanoparticles at $\gamma_0 = 0.1$ has been excluded owing to perturbation of noise occurring on the dynamic moduli.

modulus compared to the individual nanoparticles, which correspond to 1 order and 2 order of amplitude, respectively. The relatively low reinforcement factor may be due to the weak volume fraction of filler, $\phi = 10\%$ here, and the reinforcement effect should be more substantial when the volume fraction attains a relatively high value, typically $\Phi > 20\%$. Because they represent the most interesting and realistic case, we will focus on the rigid aggregates and consider them to be the primary filler in the all following sections.

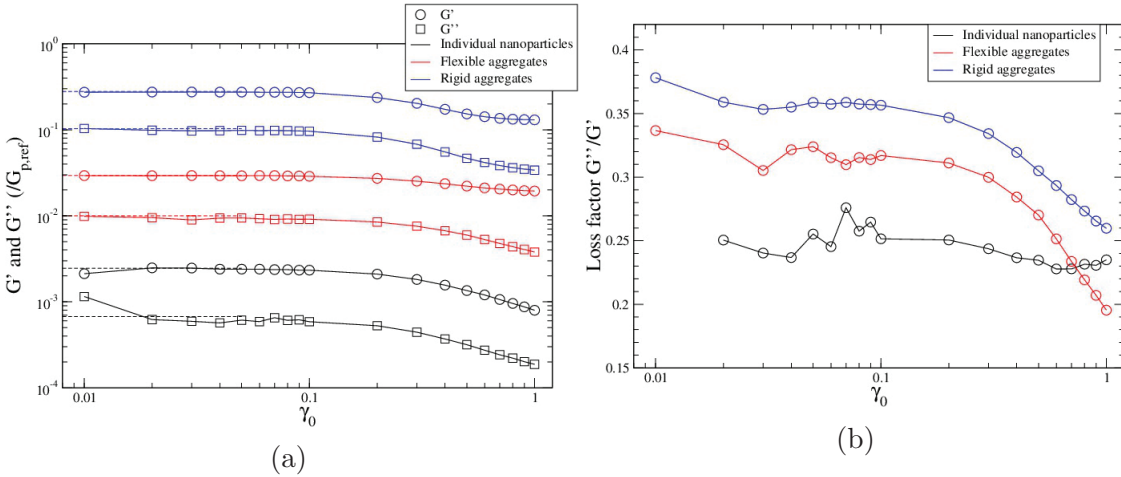


Figure 4.4: Effect of the filler types, the individual nanoparticles, the flexible and the rigid aggregates, on the stress relaxation modulus $G(t)$ with (a) a simple fluid and (b) an entangled polymers matrix, with a fixed volume fraction $\phi = 10\%$ and the unique aggregate size $N_{agg} = 50$.

4.2.2 Effect of filler volume fraction

Monodisperse rigid aggregates As shown in Fig 4.5a, the high volume fraction of monodisperse rigid aggregates (with unique aggregate size $N_{agg} = 20$) enhances reinforcement of both the storage and the loss modulus along the shear deformation amplitude γ_0 . Again, there is a good /perfect consistency between the dynamic moduli measured from the simulation at equilibrium and those from the simulations undergoing oscillatory shear.

The Payne effect occurs at all volume fractions investigated. As expected, both the storage and the loss modulus are constant in the linear regime ($\gamma_0 < 0.2$) and decrease in the nonlinear regime ($\gamma_0 \geq 0.2$). As before, there is not any overshoot even with a relatively high volume fraction $\phi = 15\%$. Finally, the corresponding loss factors are shown in Fig 4.5b, where all three systems display the same master curve which is monotonously decreasing along the shear deformation amplitude γ_0 despite of the statistical noise at small shear deformation amplitude ($\gamma_0 < 0.03$). This suggests that in the range of volume fraction, the dynamics of the aggregates remains qualitatively the same.

Polydisperse rigid aggregates Here we consider the polydisperse rigid aggregates systems considered before, with the mean aggregate size $\langle N_{agg} \rangle = 30$ and the most frequent aggregate size $N_{agg,max} = 20$, corresponding to a size polydispersity $\sigma \sim 30\%$. The effect of filler volume fraction is seen from $\phi = 10\%$ to 17% , as shown in Fig 4.6a. Both the storage and the loss modulus have been enhanced with increasing volume fraction of aggregates and it seems that the reinforcement ratio is proportional to the volume fraction of aggregates. This has been confirmed by the loss factor, as shown in Fig 4.6b. All three systems display the same master curve of the loss factor, which is monotonously decreasing along increasing shear deformation amplitude γ_0 . Again, this indicates that the polydisperse rigid aggregates

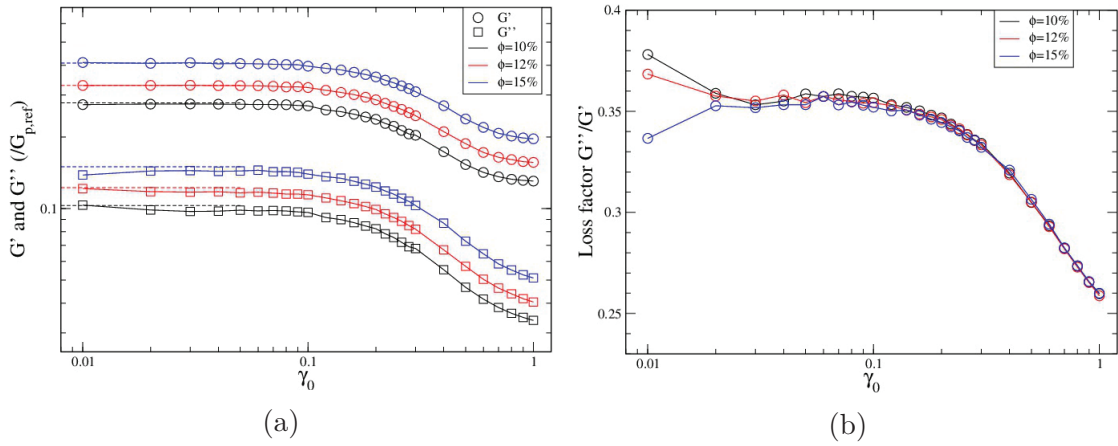


Figure 4.5: (a) Storage and loss modulus for monodisperse rigid aggregates with unique aggregate size $N_{agg} = 20$ in entangled polymer matrix. The volume fractions of aggregates varies from 10% to 15%. The dashed lines represent the dynamic moduli measured from the simulation at equilibrium in the previous chapter 3. (b) Corresponding loss factors.

systems exhibit the same dynamic regime under oscillatory shear, even with increasing volume fractions.

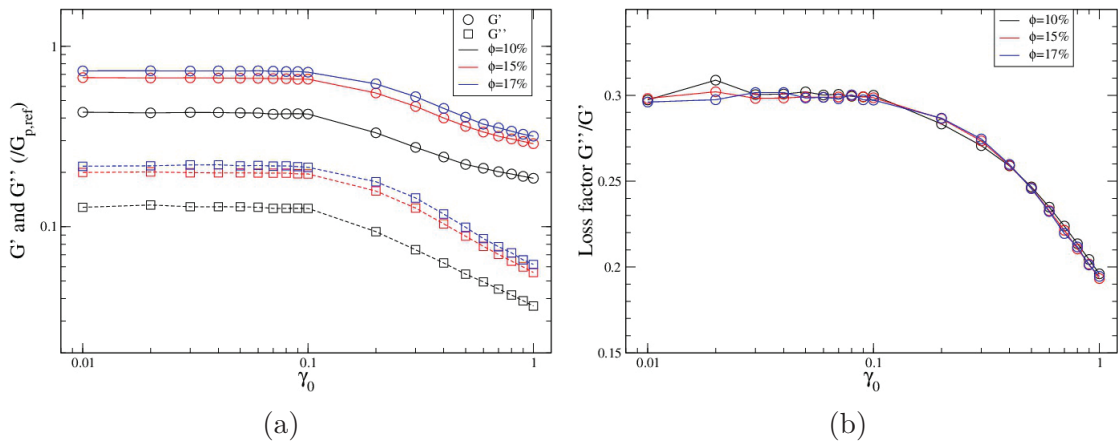


Figure 4.6: (a) Storage and loss modulus for polydisperse rigid aggregates as function of volume fractions from 10% to 17%, with entangled polymer matrix. (b) Corresponding loss factors.

4.2.3 Effect of aggregate size

The effect of aggregate size has been investigated for the monodisperse rigid aggregates with a fixed volume fraction $\phi = 10\%$ and the aggregate size varies from $N_{agg} = 20$ to 50, as shown in Fig 4.7a. The systems display reinforcement on both the storage and the loss modulus along the shear deformation amplitude. Again, the values of the dynamic modulus measured in simulation undergoing oscillatory shear display a good consistency to those measured from simulations at equilibrium.

Both the storage and the loss modulus exhibit nonlinear response in the nonlinear regime, decreasing with the shear deformation amplitude, which is referred to as the Payne effect. The values of the dynamic modulus for large deformation are nearly 2 times smaller

than those in the linear regime. Even with a relatively large aggregate size, the overshoot in G'' does not appear.

The corresponding loss factors of the two systems is shown in Fig 4.7b, where all of them decreases monotonously with increasing shear deformation amplitude γ_0 . This indicates that the dynamic regime for the polydisperse rigid aggregates systems slightly changes with the aggregate size. Small aggregates ($N_{agg} = 20$) presents a relatively higher value on the loss factor than that of the large aggregates system ($N_{agg} = 50$). This may indicate that the relative viscous dissipation, as measured by the loss factor, is enhanced by small aggregates.

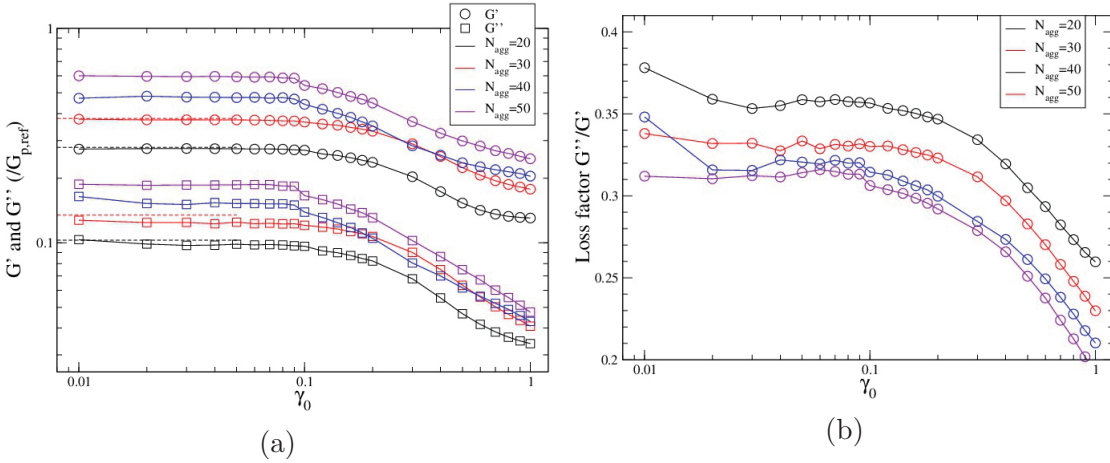


Figure 4.7: (a) Storage and loss modulus for monodisperse rigid aggregates with a unique volume fraction $\phi = 10\%$ and for different aggregate sizes from $N_{agg} = 20$ to 50. (b) Corresponding loss factors.

Due to the challenge in generating configurations of rigid aggregates, especially for the monodisperse system, we can only compare the aggregate size at relatively low volume fraction of aggregates. The monodisperse systems with large rigid aggregates suffer either from finite box size effect, where the measuring results could depend on the system size (number of aggregates), or the difficulty inherent to the generation method. Other comparison test for the effect of aggregate size has been done for the volume fraction $\phi = 12\%$ with aggregate size $N_{agg} = 20$ and 30. The corresponding figures, including the dynamic modulus and the loss factor as a function of shear deformation amplitude γ_0 , are similar to those presented before but with a slight reinforcement owing to the larger value of the volume fraction, as shown in Fig 4.8

4.2.4 Effect of polydispersity

The effect of the polydispersity of the rigid aggregates with a fixed volume fraction is shown in Fig 4.9. For comparison, we also plot the result for monodisperse aggregate with sizes $N_{agg} = 20$ and 30, which are the most frequent aggregate size and the mean size of the polydisperse system. The polydisperse system display reinforcement on both the dynamic moduli in the linear and the nonlinear regimes when compared to the monodisperse system with $N_{agg} = 20$. When the monodisperse rigid aggregates system has the mean size of the polydisperse system $N_{agg} = 30$, it seems that the reinforcement occurs only on the storage modulus in the linear regime and both the two systems exhibit similar behavior on the storage modulus in the nonlinear regime. Moreover, the polydispersity does not influence strongly the loss modulus in the linear regime and the monodisperse system shows a relatively high value on the loss modulus in the nonlinear regime when compared to those of the polydisperse system.

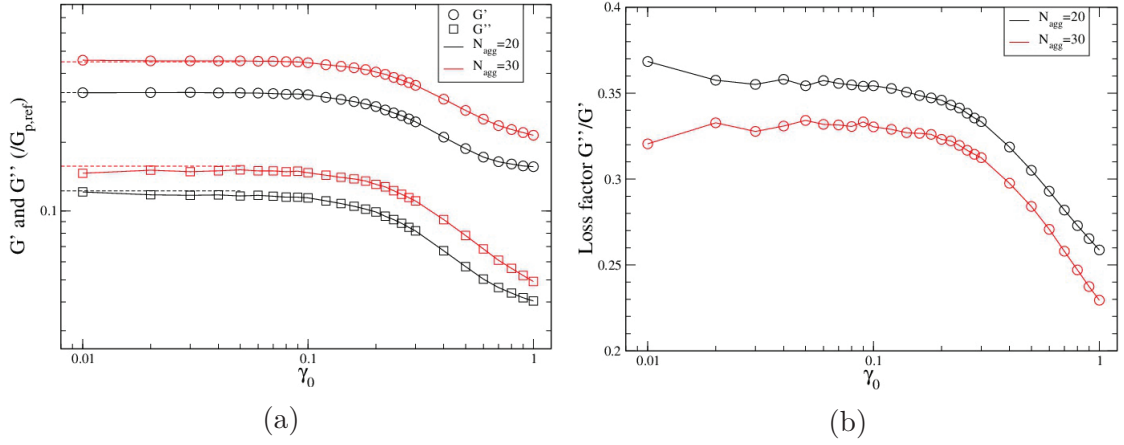


Figure 4.8: (a) Storage and loss modulus for monodisperse rigid aggregates with a unique volume fraction $\phi = 12\%$ and for different aggregate sizes from $N_{agg} = 20$ to 30. (b) Corresponding loss factors.

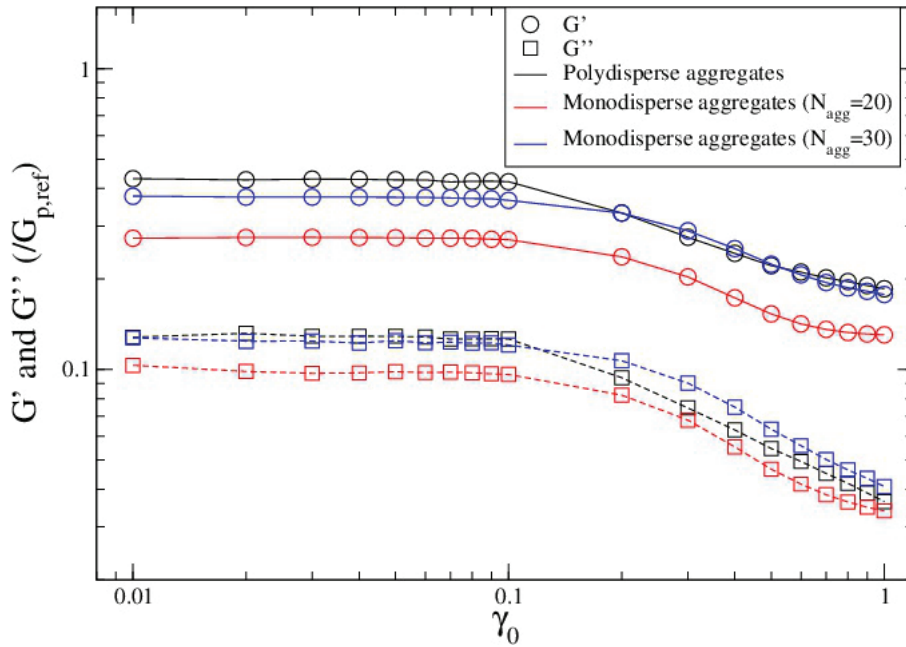


Figure 4.9: Comparison between the polydisperse and the monodisperse rigid aggregates with a fixed volume fraction $\phi = 10\%$.

4.3 High order harmonics

4.3.1 Dynamic moduli

As mentioned before, the dynamic moduli can be calculated from the shear stress at different harmonic orders and those at the first order are generally much larger than those at high order, as shown in Fig 4.10a. The ratios between the terms at high harmonic order ($n > 1$) and the primary term ($n = 1$) are shown in Fig 4.10b, it is readily seen that the dynamic modulus at high harmonic order are negligible in the linear regime ($\gamma_0 < 0.2$) and that they are essentially negative in the nonlinear regime ($\gamma_0 \geq 0.2$). Thus the storage and the loss moduli at the first harmonic order are considered as the principal modulus and are presented in all the figures in this chapter, if not otherwise mentioned.

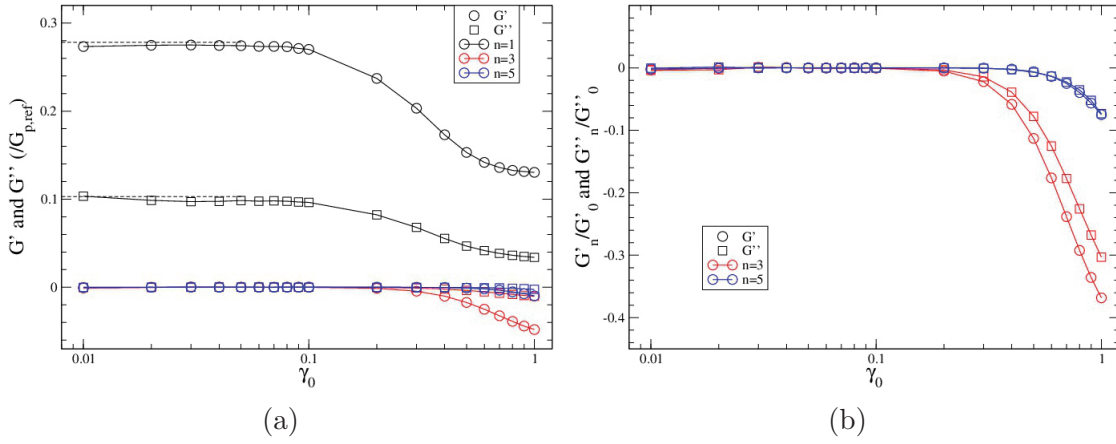


Figure 4.10: (a) Storage and loss modulus for harmonic order $n = 1, 3, 5$ and (b) the ratio of high order terms ($n > 1$) to the primary term ($n = 1$) for a monodisperse rigid aggregates system with unique aggregate size $N_{agg} = 20$ and volume fraction $\phi = 10\%$. n corresponds to the harmonic order number.

4.3.2 Shear stress

The shear stress is distorted by the high order harmonic terms. This effect can be seen via the Lissajous analysis, which displays the shear stress as a function of the shear deformation. For instance, the stress-strain Lissajous figures should be perfectly elliptical in the linear regime and be perturbed by the terms at high order in the nonlinear regime. As shown in Fig 4.11b, the stress-strain Lissajous varies as a function of shear deformation amplitudes γ_0 , for the dynamic moduli expressed in Fig 4.11a, where the nonlinear regime occurs when $\gamma_0 \geq 0.1$. The Lissajous figure of the shear stress is elliptical in the linear regime ($\gamma_0 = 0.05$), while it is perturbed for large deformation ($\gamma_0 \geq 0.1$).

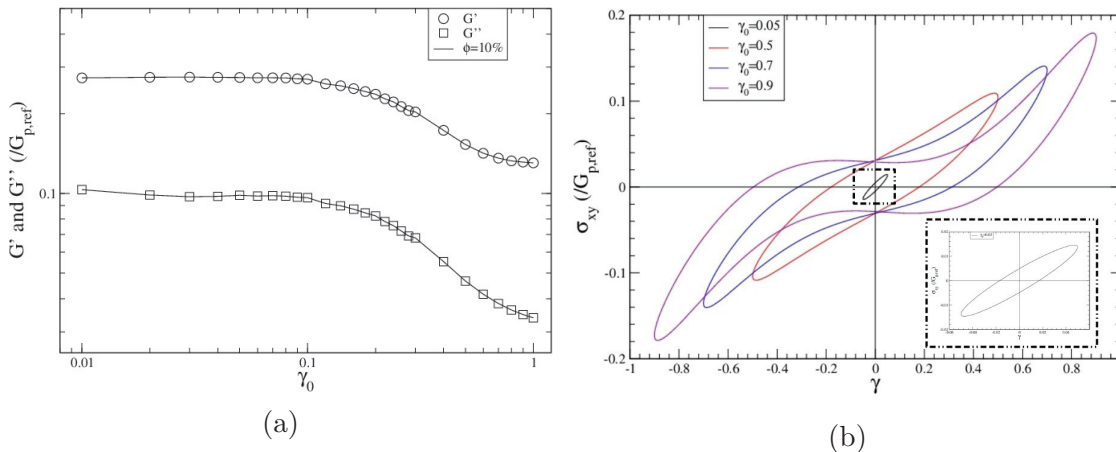


Figure 4.11: (a) Storage and loss moduli as a function of the shear deformation amplitude γ_0 for monodisperse rigid aggregates with unique aggregate size $N_{agg} = 20$ and volume fraction $\phi = 10\%$. (b) Stress-strain Lissajous figures for a series of shear deformation amplitudes in both the linear regime and the nonlinear regime, for the system shown in the left figure.

4.4 Filler behavior under LAOS

4.4.1 Gyration tensor



Figure 4.12: Schematic of the contour of a disordered polymer chain measured by (a) gyration tensor and (b) radius of gyration [95].

In contrast to the equilibrium simulations presented in chapter 3, the fillers are now subject to a finite shear deformation. Therefore, their orientation and shape may be modified by the deformation. Here we try to characterize the shape of aggregates under shear deformation. As seen in chapter 2, the gyration tensor is a useful tool to determine the conformation of filler [95], and provides more information than the radius of gyration of filler, as illustrated in Fig 4.12. As a real symmetrical matrix, \bar{S} can always be diagonalized. The eigenvectors indicate the orientation directions of the aggregates and the eigenvalues give the size of the aggregate in the corresponding directions. They can be used to quantify the deformation and orientation of the fillers under shear deformation.

One could define the orientation as the direction associated to the largest eigenvalue. However, because our aggregates are not perfectly rigid but can slightly deform, the largest eigenvalue can switch from one axis to the other between two successive time steps, as we have observed. To avoid such discontinuous change in orientation, we proceed as follows. At the beginning of the simulation, we define the orientation of a given aggregate from the eigenvector which has the largest eigenvalue. Then, we assume that the aggregates can not rotate by a large angle in one time step. Accordingly, the eigenvector in the later step is chosen to be the eigenvector which is the "nearest one" to the primary eigenvector in the previous step ². This method has been implemented following the orientation of the aggregates which will unveil the relationship between the microscopic behavior (orientation) of the aggregates and the macroscopic rheological response in the following sections.

4.4.2 Results

We have measured the orientation and the deformation ratio of monodisperse rigid aggregates under oscillatory shear, the corresponding dynamic moduli is shown in Fig 4.5a, where the system of interest has volume fraction $\phi = 10\%$ and an aggregate size $N_{agg} = 20$. The orientation angle is defined as the angle between the projection of the orientation vector in the velocity profile plane and the shear axis, as shown in Fig 4.13, where λ is the orientation vector, λ_{xy} is its projection on the xy plane, x direction is the shear direction and y direction is the vertical direction of the velocity profile. In the simulations, the shear axis is defined as the x direction and the velocity plan is the xy plane. The orientation of aggregates has been investigated as a function of time points in one sinusoidal shear period

²In practice, the nearest vector is the one that maximizes the absolute value of the scalar product.

at a given shear deformation amplitude. The different discrete values of time t_i correspond to different values of the instantaneous deformation $\gamma(t_i) = \gamma_0 \sin(t_i)$, for a given shear deformation amplitude γ_0 .

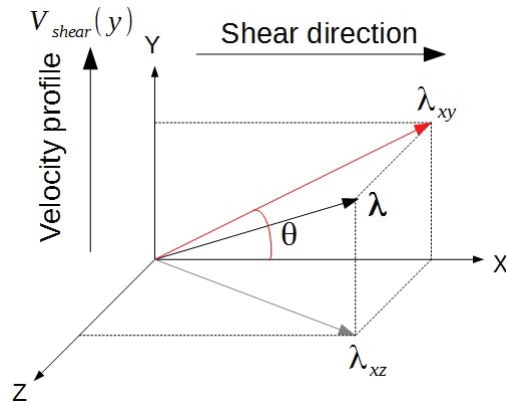


Figure 4.13: Schematic of the orientation vector of the aggregates.

Orientation

The orientation angles of the aggregates have been investigated at shear deformation amplitudes $\gamma_0 = 0.1$ and 0.5 , as shown in Fig 4.14a and Fig 4.14b, respectively, where the legends present the different time points during one shear period and all data are collected after the system reaches a steady state. The former amplitude corresponds to the linear regime while the latter is considered in the nonlinear regime.

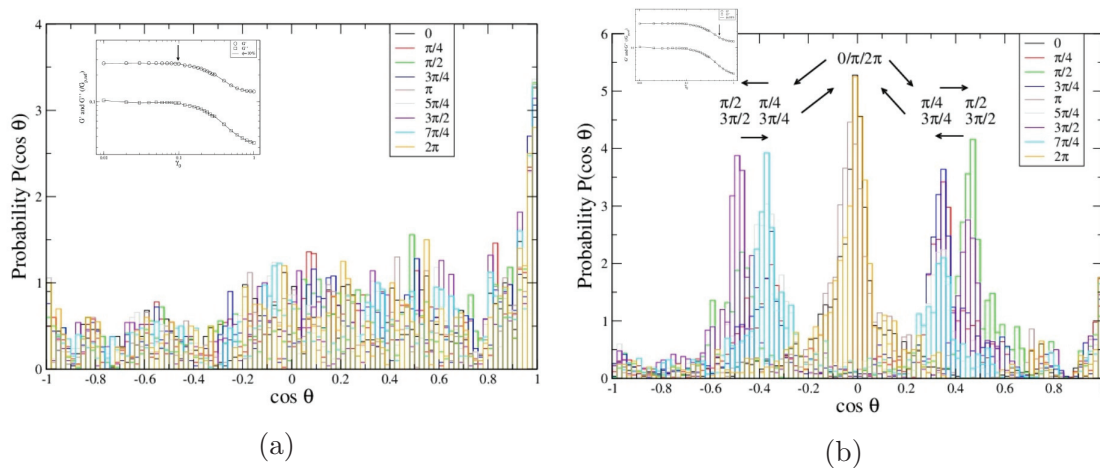


Figure 4.14: Normalized distribution of the orientation angle of monodisperse rigid aggregates ($N_{agg} = 20$ and $\phi = 10\%$) as function of time points in one sinusoidal shear period with shear deformation amplitude (a) $\gamma_0 = 0.1$ and (b) $\gamma_0 = 0.5$.

One can see that the aggregates do not exhibit any bias on the orientation when the system is in the linear regime ($\gamma_0 = 0.1$). In contrast, the orientation of the aggregates is strongly influenced by the shear deformation in the nonlinear regime ($\gamma_0 = 0.5$). This indicates that the system under large shear deformation reaches steady state different from the equilibrium state at the beginning. It suggests the following picture: as the drop on both the storage and the loss modulus occurs, the aggregates tend to align and rotate simultaneously. A simple 2D illustration is shown in Fig 4.15. In the linear regime, the

aggregates are not oriented by small shear deformation and the average orientation direction of aggregates is not observed, as shown in Fig 4.15a. When the system is under large shear deformation, the aggregates are forced to orient towards the shear direction at a given time and this leads to the alignment of the aggregates shown in Fig 4.15b.

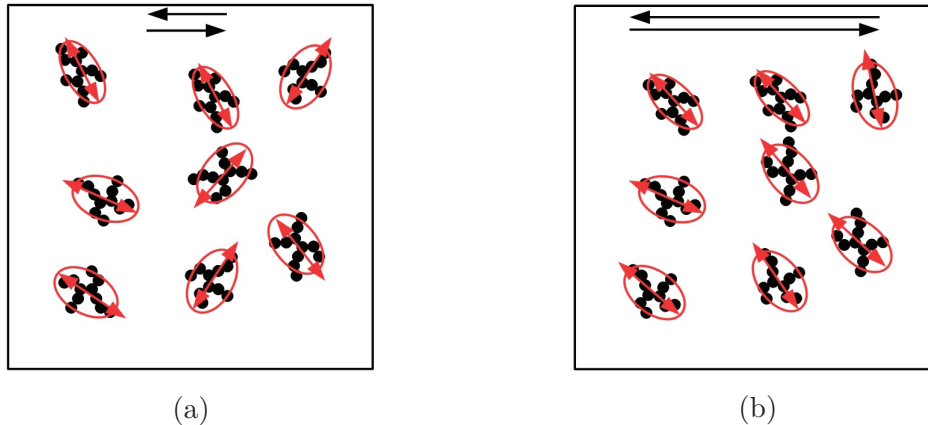


Figure 4.15: Schematic illustration of the aggregate orientation under shear (a) in the linear regime (small deformation) and (b) in the nonlinear regime (large deformation).

Effect of polydispersity The polydisperse rigid aggregates that we consider here are built following a distribution given by Eq 2.1. This disparity of aggregate size may affect the relative orientation of the aggregates, as compared to the monodisperse case.

The simulation results are shown in Fig 4.16, where the system consists of polydisperse rigid aggregates with volume fraction $\phi = 10\%$ and the mean aggregates size is $N_{agg,mean} = 30$. We have defined two classes of aggregates: small ones if $N_{agg} \leq 30$ and large otherwise. In the linear regime, the effect of shear flow on the orientation of aggregates is mostly negligible, as that shown in Fig 4.14a for the monodisperse case. Then, we have focused on the effect in the nonlinear regime and the following discussion will be around the phenomenon occurring at a fixed shear deformation amplitude $\gamma_0 = 0.5$.

As shown in Fig 4.16b, Fig 4.16c and Fig 4.16d, both the small and the large aggregates exhibit the same tendency at all three typical time points $\omega t = 0, \pi/4$ and $\pi/2$, corresponding to instantaneous deformations $\gamma(t) = 0; \gamma_0/2$ and γ_0 respectively. This may indicate that the aggregates are oriented by large shear deformation regardless their sizes. Hence, we can conclude that the polydispersity does not influence the orientation of aggregates under shear deformation.

Deformation ratio

The rigid aggregates modeled here are intended to be unbreakable and highly resistant to deformation, especially for the case under shear. To quantify the deformation, we introduce the deformation ratio as the quantity $\lambda(t)/\lambda(t=0)$ between the instantaneous largest eigenvalue and its initial value. The deformation ratio is shown in Fig 4.17, for the same systems as considered before and the same shear deformation amplitudes. The rigid aggregates maintain essentially the same structure in the linear regime ($\gamma_0 = 0.1$), with a variation in deformation ratio that does not exceed 10%. Under large shear deformation, the rigid aggregates are slightly deformed, and exhibit a periodic behavior in the nonlinear regime ($\gamma_0 = 0.5$), which follows the shear deformation. So it appears that the rigid aggregates are relatively stable even under large shear deformation.

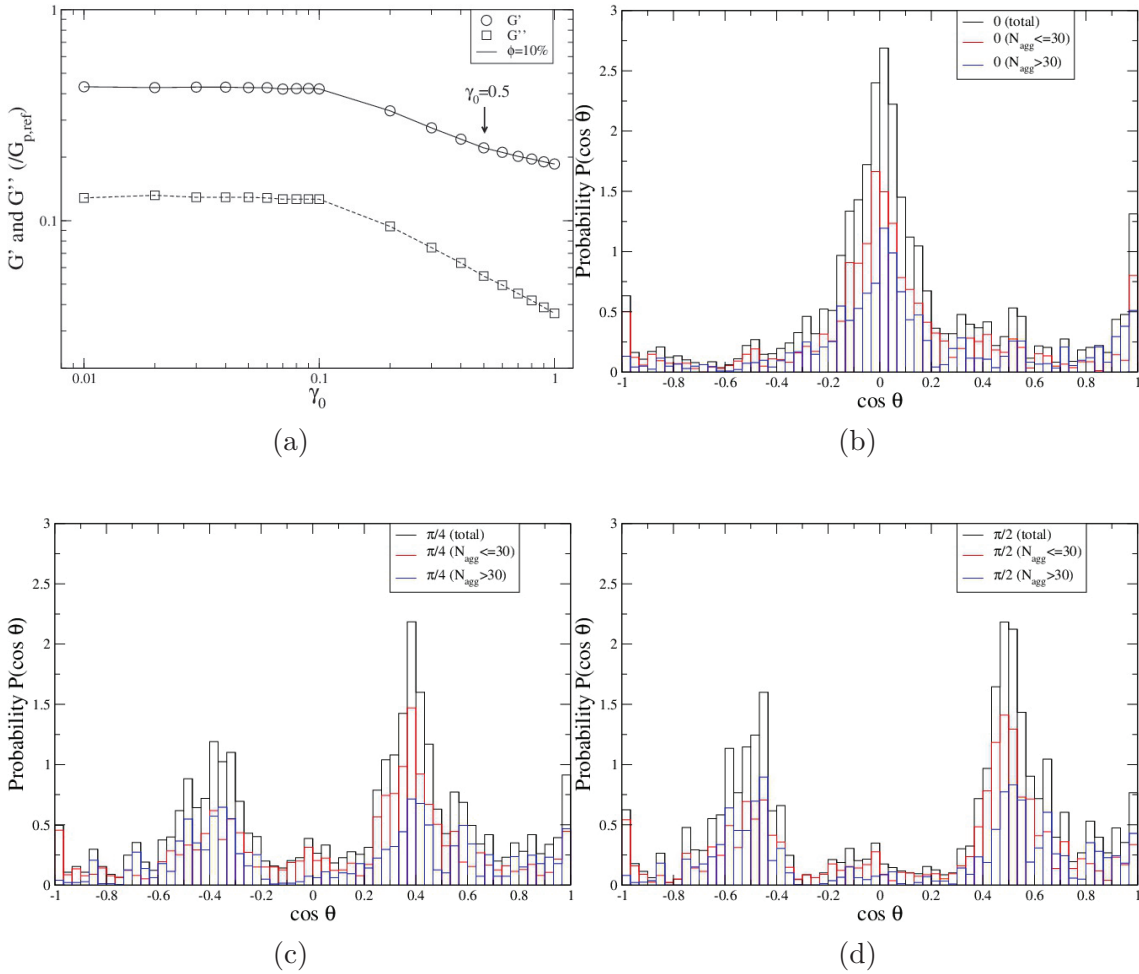


Figure 4.16: (a) Storage and loss moduli as a function of shear deformation amplitude γ_0 for a polydisperse rigid aggregates with volume fraction $\phi = 10\%$. The normalized probabilities of orientation angle of aggregates in terms of the time points in one shear period and the aggregate size, (b) $\omega t = 0$, (c) $\omega t = \pi/4$ and (d) $\omega t = \pi/2$, at $\gamma_0 = 0.5$ in the nonlinear regime. The total contribution and the partial contribution from the small and the large aggregates are displayed by distinct colors.

To conclude this part, we see that in the linear regime, the rigid aggregates do not display any preferred orientation and they are not deformed. In the nonlinear regime, the rigid aggregates are oriented by shear deformation and present a periodic rotation, as shown in Fig 4.14b. Meanwhile, the aggregates are slightly deformed with a large ratio more than 10% around $\gamma_0 = 0.5$. Such changes in the nanocomposite microstructure might be at the origin of the microscopic phenomena that plays a role in the Payne effect. Indeed, it is reasonable to relate the alignment and deformation of the aggregate to the stress softening, as seen in the drop of the storage moduli. More generally, our simulations show the connection between the nonlinear rheology of nanocomposites and the evolution of the aggregate degrees of freedom under shear.

4.5 History-dependent LAOS

The question we address now is the following: "does the bias of orientation of aggregates remain when the shear deformation amplitude decreases?". To answer this question, we will

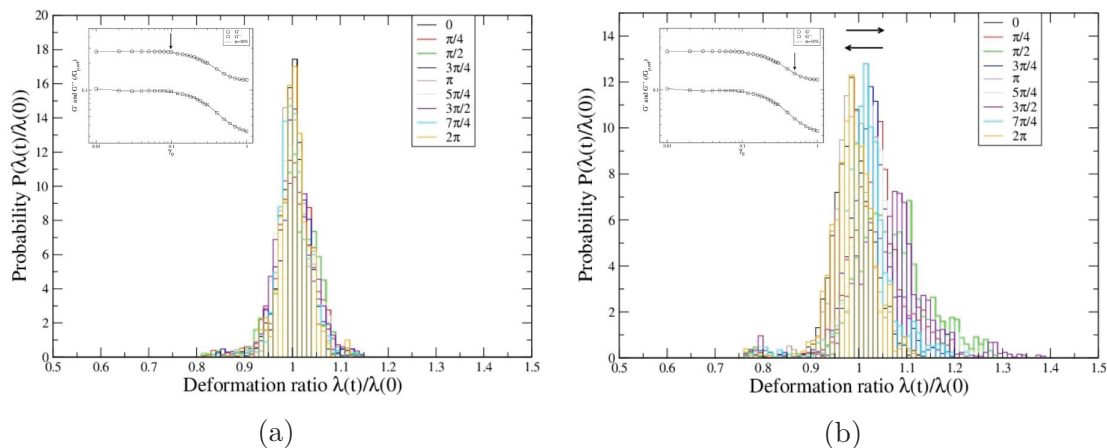


Figure 4.17: Deformation ratio of the same systems shown in Fig 4.14 with shear deformation amplitude (a) $\gamma_0 = 0.1$ and (b) $\gamma_0 = 0.5$.

submit the model system to non trivial deformation history, and concomitantly study the relative orientation of the aggregates during time. We describe below the history-dependent rheological phenomena that occur in the nonlinear regime.

4.5.1 Single shear cycle

We consider here an history dependent deformation involving a cycle of deformation amplitude increasing from $\gamma_0 = 0.1$ to 1 then back to 0.1, by finite step of 0.1. For every value of γ_0 , the system is left a long time (more than 600 cycles) that is generally sufficient to reach a steady state³. Shown in Fig 4.18a are the results for a polydisperse rigid aggregates system with volume fraction $\phi = 10\%$. The storage and the loss moduli exhibit the monotonous decreasing tendency along the loading process, during which the shear deformation amplitude increases, and they display different values in the unloading process, during which the shear deformation amplitude decreases. The evolution of the shear stress along the loading and the unloading process is shown in Fig 4.18b, where we can see the difference on the contour of shear stress in the two processes.

One can readily recognize the difference on the average shear stress over a number of loops as a given shear deformation amplitude γ_0 between the loading and the unloading process, as shown in Fig 4.19. The shear stress displays transient process in both the loading and the unloading process, however, the amplitude shrinks in the unloading process. This may be due to the alignment of the aggregates along the velocity axis under large shear deformation and it is too hard to relax from the biased stationary state even when the shear deformation amplitude reduces to a small value, like $\gamma_0 = 0.1$ in the unloading process.

4.5.2 Long time relaxation

As expressed in the previous section, the storage and the loss modulus drop after a single cycle of shear amplitudes from $\gamma_0 = 0.1$ to 1.0. A long time relaxation test has been simulated in which the system is sheared with a constant deformation amplitude $\gamma_0 = 0.1$ for a very long time in order to disclose whether or not the system can relax back to its initial stationary state.

We have tested both the mono- and the poly-disperse rigid aggregates systems. The storage and the loss modulus as a function of the shear deformation amplitude γ_0 is shown in Fig 4.20a. The systems remain under shear at the last deformation amplitude $\gamma_0 = 0.1$

³ Note that the steady state does not seem to be reached in the first two steps.

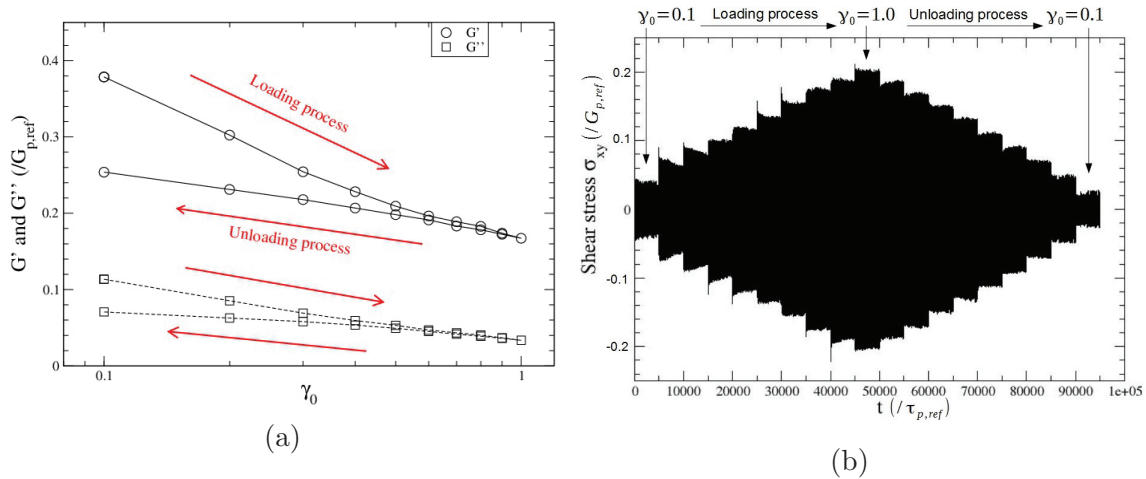


Figure 4.18: (a) Storage and loss moduli as a function of a series of shear deformation amplitude γ_0 , for a polydisperse rigid aggregates system with volume fraction $\phi = 10\%$. (b) The corresponding shear stress during the loading and the unloading process, as a function of time.

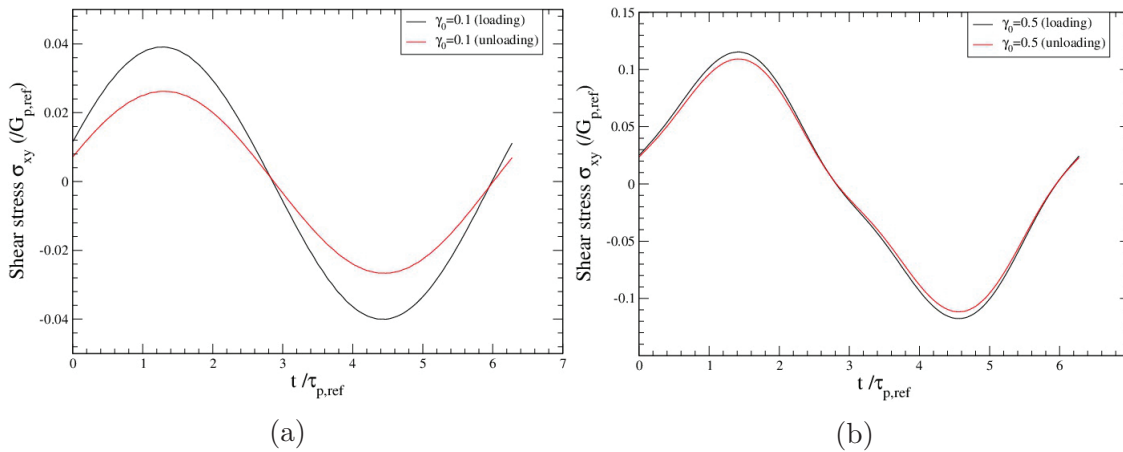


Figure 4.19: Average shear stress during one cycle with shear deformation amplitudes (a) $\gamma_0 = 0.1$ and (b) $\gamma_0 = 0.5$ in loading and unloading process.

here for 10 time much longer (more than 6000 cycles) than usual and neither the storage modulus nor the loss modulus display the similar values as those at the beginning of the loading process. It may be easier to observe this phenomenon in Fig 4.20b, where the dynamic moduli are displayed as a function of simulation time. The system seems to reach a quasi-stationary state distinct from the initial stationary state at the beginning of the loading process. This indicates that the global conformation of the aggregates is oriented strongly by large shear deformation and the system is "locked" in this oriented stationary state even after very long times.

4.5.3 Multiple shear cycles

In addition to the single cycle of shear, we have investigated the multiple cycles of shear under LAOS, for different rigid aggregates systems as shown in Fig 4.21, including both the mono- and the poly-disperse rigid aggregates systems for two values of the volume fraction. The systems have been undergoing 3 cycles. Despite some missing points at $\gamma_0 = 0.1$ in Fig 4.21c, it seems that the systems do not return to their initial stationary state once after

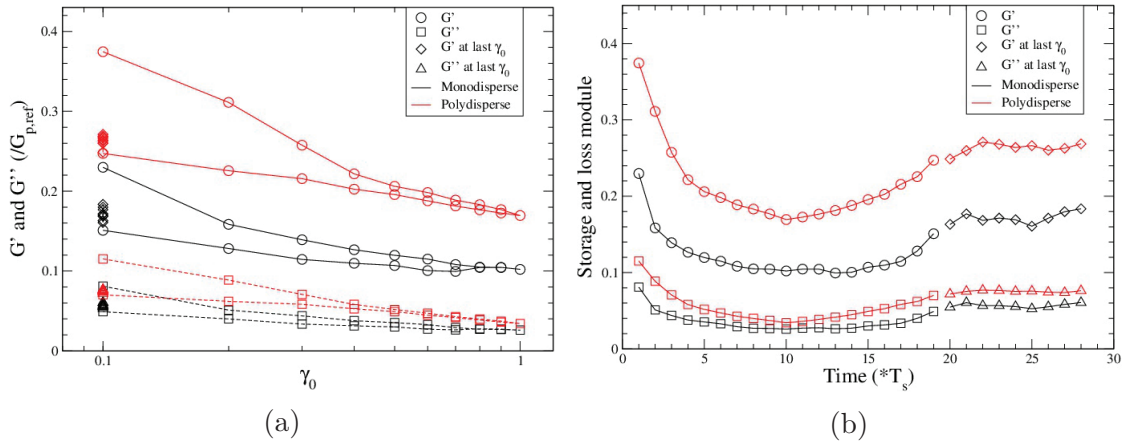


Figure 4.20: Storage and loss modulus as a function of (a) shear deformation amplitude γ_0 and (b) time, for poly- and mono-disperse rigid aggregates with fixed volume fraction $\phi = 10\%$ and unique aggregate size $N_{agg} = 20$ for the monodisperse system. $T_s \approx 800T_p$ is the simulation time used for one deformation amplitude and $T_p = 2\pi \approx 6.283 \tau_{p,ref}$ is the period of shear deformation.

the loading process in the first cycle and that in both dynamic moduli, the two subsequent cycles are very close to the unloading of the first cycle. This phenomenon appears to be independent of the polydispersity of the system or the volume fraction of filler. This may be related to the case investigated with long time relaxation in the previous section 4.5.2 and we may conclude that the history-dependent rheological responses under shear are strongly related to the highly oriented global conformation of filler which is mostly driven by the large shear deformation.

The distribution of orientation angles for a polydisperse rigid aggregates system, shown in Fig 4.22a. The rotation angles of aggregates are concentrated around $\cos(\theta) = 0$ and $\cos(\theta) = 1$ and this should not occur for a small shear deformation amplitude $\gamma_0 = 0.1$, as seen in previous Fig 4.17a. As shown in Fig 4.22b, the probability at $\cos(\theta) = 1$ in the loading process of the first cycle is relatively low and the others are generally 3 or 4 times higher. This points to a relationship between the microscopic global oriented conformation and the macroscopic rheological properties which has been discussed before. Moreover, it is consistent with the conclusion drawn from the case with long time relaxation, that the system can not return to its initial stationary state once it has been submitted to large deformation.

To conclude, the aggregates are oriented by the large shear deformation during the loading process corresponding to the first cycle. Afterwards, the system remains in the oriented state even though the shear deformation amplitude is reduced. As a result, the storage and the loss moduli in the second and the third cycles take the values of those in the unloading process of the first cycle.

4.6 Aggregates with attractive interaction

An overshoot on the loss modulus at large shear deformation amplitude is commonly seen in experiments, at least if the volume fraction of fillers is sufficiently high, as shown in Fig 1.13 for the carbon black-filled SSBR compounds. However, in the results presented so far, we saw that the rheological response of our model nanocomposite is always of type 1 (see Fig 1.11), meaning that the dynamic moduli decrease monotonously with shear deformation amplitude and do not present any overshoot. The latter is often interpreted as the destruction of filler network due to shear deformation. Because the interaction between the

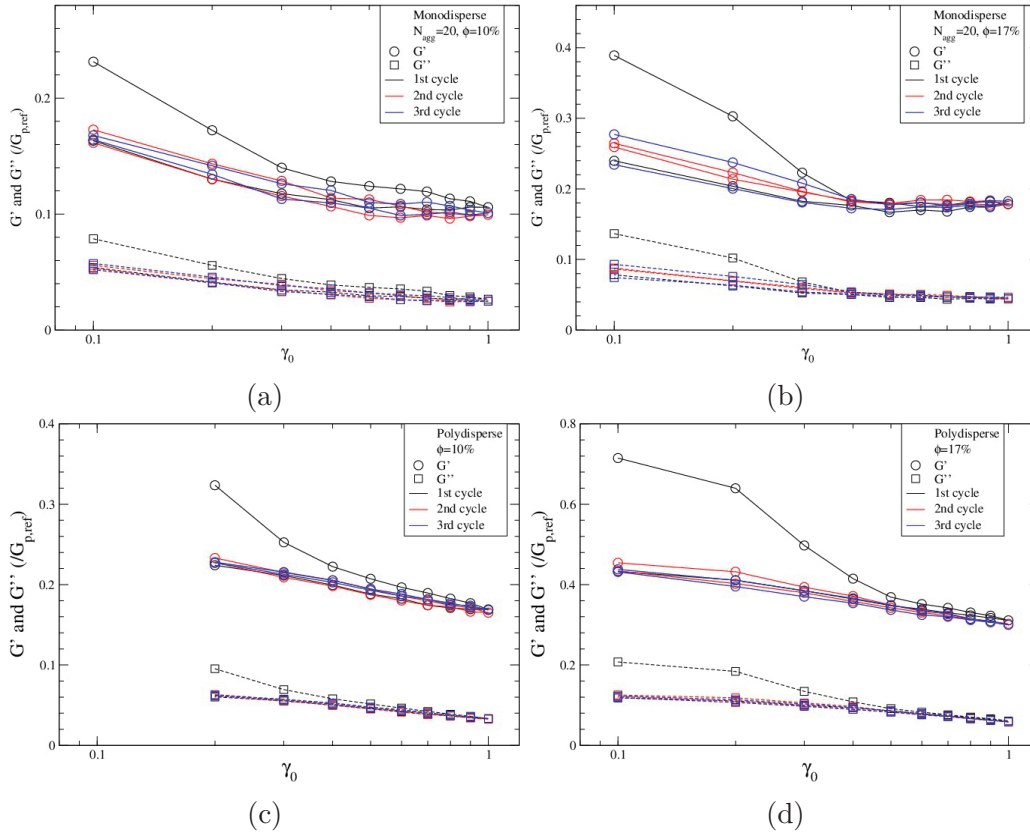


Figure 4.21: Storage and loss modulus as function of 3 cycles of shear deformation amplitudes for monodisperse rigid aggregates systems with unique aggregate size $N_{\text{agg}} = 20$ and (a) volume fraction $\phi = 10\%$ and (b) $\phi = 17\%$, and polydisperse rigid aggregates systems with (c) volume fraction $\phi = 10\%$ and (d) $\phi = 17\%$.

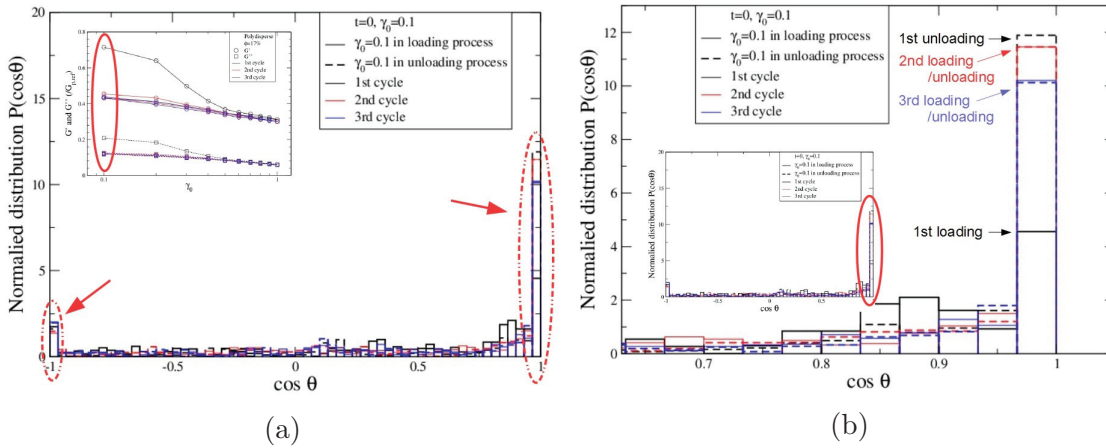


Figure 4.22: (a) Distribution of orientation angles for a polydisperse rigid aggregates system in Fig 4.21d at shear deformation amplitude $\gamma_0 = 0.1$ for the loading and the unloading processes of 3 cycles. (b) Zoom in the area near $\cos(\theta) = 1$.

aggregates considered so far are purely repulsive, the aggregates may disperse in a homogeneous manner in equilibrium state (in the absence of shear deformation) and we do not expect the formation of a network. In this section, we investigate the effect of attractive interaction between particles. We first discuss the implementation of such attractive interaction, and show preliminary results on the corresponding non-linear rheology of attractive

nanofillers systems.

Attractive potential The middle and long range attraction part of the original Lennard-Jones potential may be ideal to generate the agglomerate of fillers before shear deformation. As mentioned in the previous section 2.2.1, the original Lennard-Jones potential contains a short-distance repulsive part and a long-distance attractive part, and can be written as follows:

$$U_{LJ}(r) = 4\epsilon \left[\left(\frac{\sigma}{r} \right)^{12} - \left(\frac{\sigma}{r} \right)^6 \right], \quad (r > 0). \quad (4.8)$$

However, the long-distance attractive force is not comparable to the repulsive force at short distance if they have the same parameters. Thus, the new attractive Lennard-Jones potential is considered to be independent from the already applied repulsive Lennard-Jones potential. We consider to increase the attraction between fillers by solely enhancing the depth of the attractive Lennard-Jones potential ϵ_{att} while the other parameters remain the same as those of the repulsive Lennard-Jones potential.

The aggregates maintain their structure via the balance between the recall force from the springs and the short-distance repulsive force. Introducing an attractive interaction could modify the aggregate geometry, precluding a meaningful comparison with the results obtained so far. For this reason, we have chosen not to implement the attractive force between the particles within the same aggregates. Rather, we propose to apply the attractive force only between the particles from different aggregates. As illustrated in Fig 4.23, particles of the same aggregate interact via short-range repulsion and the springs forces, while particles belonging to different aggregate interact via repulsion and the attractive part. This approach should be effective to create the agglomeration of the fillers and maintain the global conformation within a range of shear deformation amplitudes.

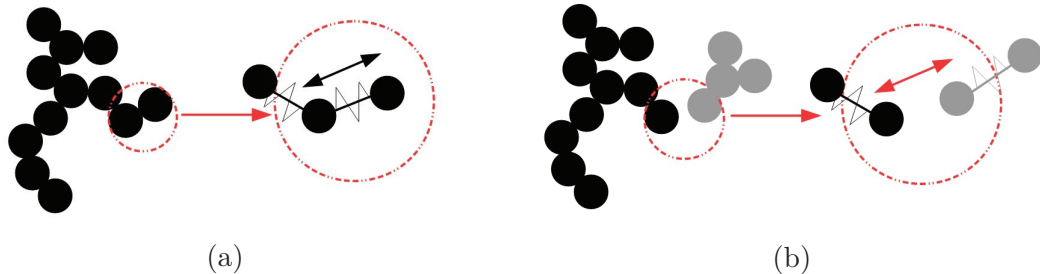


Figure 4.23: Schematic of interactions between particles belonging to (a) the same aggregate and (b) different aggregates.

Test results

We have tested this model for a monodisperse rigid aggregates system with unique aggregate size $N_{agg} = 20$ and volume fraction $\phi = 10\%$, as shown in Fig 4.24a, where the storage and the loss modulus are displayed as a function of shear deformation amplitudes γ_0 from the linear and the nonlinear regime. The attractive forces are up to 5 times larger than the repulsive forces $\epsilon_{att} = 5\epsilon_{repul}$. We see reinforcement on both the storage and the loss moduli for the case with attraction interaction when compared to the case with only repulsion. In contrast with the results obtained with the purely repulsive aggregates, the loss factors for the cases with attraction are no longer monotonous. There is a maximum in the nonlinear regime, after which the loss modulus starts to decrease, as shown in Fig 4.24b. In the future, we will characterize the evolution of the agglomerate morphology during LAOS.

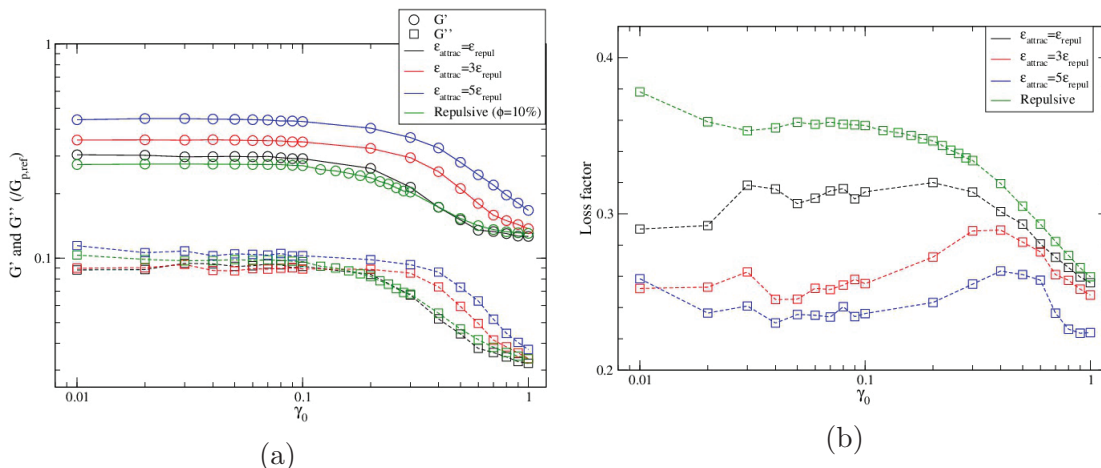


Figure 4.24: (a) Storage and loss moduli of monodisperse rigid aggregates system with/without attraction. (b) Corresponding loss factors.

Conclusion

In this chapter, we have investigated the rheological properties of filled entangled polymer systems in the nonlinear regime, under oscillatory shear. All the storage and the loss modulus in the linear regime are consistent with the dynamic moduli computed from the stress relaxation modulus via Green-Kubo simulations at equilibrium. In the nonlinear regime, the well-known Payne effect is observed for our model of nanocomposites, where the storage and the loss modulus both decrease with increasing shear deformation amplitude.

The filler type always influences the stress response, in the linear regime and the nonlinear regime. Among the three filler types, both the flexible and the rigid aggregates display a substantial reinforcement on the dynamic moduli when compared to the individual nanoparticles, where the reinforcement factors are around 10^1 and 10^2 , respectively. All three fillers show the Payne effect in the nonlinear regime, however, they are not undergoing the same dynamics. Individual nanoparticles system exhibits suspension-like behavior and its loss factor is mostly independent from the deformation amplitude. This is different from the flexible and the rigid aggregates systems, where both systems display monotonous decreasing loss factors along the deformation amplitude.

The volume fraction of aggregates has a dramatic influence on the reinforcement on the dynamic moduli for both the mono- and poly-disperse rigid aggregates systems. Note again the difficulty in generating aggregate systems with high volume fractions. Despite of various volume fractions, the mono- and poly-disperse rigid aggregates systems exhibit the same dynamic regime under oscillatory shear. Again, the overshoot in the loss factor has not been found in the systems with available volume fractions.

The aggregate size also influences the rheology of the system, especially in the monodisperse systems. The large aggregate size can induce the reinforcement on the dynamic modulus, which may be due to the enhanced interaction between aggregates. However, we have not found overshoot on the two dynamic moduli.

Since the applied shear deformation is sinusoidal, the shear stress display a perfect sinusoidal form with a phase angle in the linear regime while the signal is strongly distorted by the terms of high harmonic orders in the nonlinear regime. This effect should be considered when computing the storage and the loss modulus since they are both calculated directly from the shear stress in this chapter. We have confirmed that the effect exists but is negligible when compared to the primary terms in the nonlinear regime. Therefore, despite the intrinsic non linearity inherent to the Payne effect, the shear response may be characterized to a good approximation by the linear moduli $G'_1(\omega)$ and $G''_1(\omega)$.

Moreover, we have seen that the aggregates can be mostly aligned in the nonlinear regime and there are some slight deformation of the rigid aggregates compared to their equilibrium state. This may lead to a better understanding of the relationship between the microscopic filler conformation and the macroscopic rheological properties. Once the system is oriented by large shear deformation, the rigid aggregates can hardly return to their initial stationary state and this also influences the dynamic modulus. This induces the history-dependent LAOS phenomenon, in which the shear deformation amplitudes varies in one or multiple cycles, which contains the loading process, from the initial value to the largest value, and the unloading process, from the largest one back to the initial value.

An overshoot is often seen on the loss modulus in realistic filled polymer composites, such as *e.g.* the carbon black filled SSBR compounds. Unfortunately, this phenomenon has not been found in the present results. This may be due to the absence of the agglomeration of fillers in our model system. Thus, we have proposed a method to promote the agglomeration of filler, by adding an attractive Lennard-Jones potential. We have done the tests for the former method and the overshoot has not been found. Nevertheless, the loss factors of the system with attractive interactions are no longer monotonous and display maximum at the beginning of the nonlinear regime. More work needs to be done before one can fully assess the role of attractive interactions. Also, further investigation are needed to provide a microscopic origin of the existence of an overshoot in the loss factor.

General conclusion

The object of this work was to develop a mesoscopic model to simulate the behavior of aggregates in a polymer nanocomposites and measure the resulting rheological properties of model composites. The need to build a mesoscopic model, rather than using molecular simulations, is justified by the gap in sizes between the filler aggregates and the monomers of the polymer matrix. This model is based on a generalized Langevin equation, in which the motion of the polymer chains is not described explicitly, but its effect on the filler particles is "averaged out" and represented by a velocity memory kernel. This approach simplifies the simulation process and reduces significantly the computation cost, as compared to fully explicit methods. With this model in hand, we have concentrated our effort on model fractal aggregates nanocomposites, motivated by their wide presence in the industrial applications.

Let's summarize the results. First, we have shown that aggregates display reinforcement levels larger than individual nanoparticles. We have systematically studied the rheological properties of filled polymer compounds in the linear regime, via the stress relaxation modulus $G(t)$, the storage modulus $G'(\omega)$ and the loss modulus $G''(\omega)$, with various fillers in non-entangled and entangled polymer matrix. The filler volume fraction has been found to be one of the key parameters to cause reinforcement, mostly owing to the increasing interaction between fillers. The filler size, especially the aggregate size, also presents a different reinforcement on the rheology which is probably due to the appearance of filler network. The filler particle size can also influence the reinforcement owing to the decreasing polymer-filler interaction area when the particles size increases. We have demonstrated that the effective viscosity of the filled polymer systems are well above the conventional Einstein-Smallwood law. In terms of aggregate size, a regime change can be found on the effective viscosity which may disclose the existence of the global filler network. Moreover, the aggregate polydispersity can further enhance the rheological properties of filled polymer system over the monodisperse system. In the linear regime, the rheology of aggregates-filled polymer systems is also accompanied by slow relaxation dynamics at long times where the primary particles diffuse slowly and the aggregates are not prone to rotate. However, the local nanoparticle dynamics has been found to be relatively fast, which can be evidenced by the dynamic structure factor of primary particles, single aggregate and inter-aggregates. This indicates the complex mechanisms behind reinforcement in our model systems, which are characterized by both slow and fast degree of freedom.

Beyond the linear regime, we have systematically investigated the rheology of filled entangled polymer composites under oscillatory shear deformation of increasing amplitude. Of particular interest, we have shown evidence of the so-called Payne effect, defined as a drop of the storage modulus for moderate deformation amplitude. We have seen that the amplitude of the Payne effect is highly dependent on the type of fillers considered. Rigid aggregates display large reinforcement levels, and accordingly the highest amplitude of the

Payne effect, if we compare to flexible aggregates or individual nanoparticles. The loss factor of the individual nanoparticles is independent of the deformation amplitude while those of both the flexible and the rigid aggregates are monotonous decreasing functions of the deformation amplitude. The filler volume fraction of aggregates can influence the amplitude of the Payne effect, whatever the aggregate size dispersity. Polydisperse systems displays a relatively slightly more pronounced stress softening effect when compared to the monodisperse system, and the effect should be even enhanced by higher volume fractions that we have considered here.

In the nonlinear regime of deformation, observables measuring the stress response such as the shear stress or the dynamic moduli, may contain high order harmonic terms. For instance, the shear stress can be distorted when the system is submitted to large deformation, while it is perfectly sinusoidal in the linear regime. The dynamic moduli, however, are always dominated by the primary terms and their high order terms are small and negative in the nonlinear regime. We have investigated the primary cause behind stress softening by quantitatively characterizing the configuration changes of the aggregates. Specifically, we have computed the rotation and the deformation under deformation, via the gyration tensor which can precisely quantify the orientation direction and the elongation of the aggregates. The large levels of deformation applied on the system may align the aggregates along the flow direction, leading to the periodic movement related to sinusoidal signal corresponding to the shear deformation. This suggests that the structural change corresponds to the destruction of the filler network, which in turn reduces the effective elasticity of the system and leads to the decreasing storage modulus. This phenomenon is independent from the aggregate size dispersity, as the aggregates are only slightly distorted under large deformation.

The history-dependent LAOS behavior has been observed for a filled polymer system undergoing multiple cycles of deformation amplitude. Specifically, the deformation amplitude varies in cycle, from initial value to the last value then back to the initial one and so on. This history-dependent phenomenon appears to be independent from the dispersity or the filler volume fraction. As a result, the shear stress and the dynamic moduli are different in the loading process and in the unloading process, an effect that we explain by the alignment of the aggregates under large deformation. This effect is much enhanced in the simulations with multiple cycles, in which the dynamic moduli in the second and the third cycle display the similar values as those obtained in the unloading process in the first cycle. This suggests that the alignment of the aggregates is long-lived and relatively stable even when the deformation amplitude varies. Moreover, we have confirmed that the aligned aggregates can hardly return to their initial stationary state even after a long time relaxation process. As a conclusion, this purely structure-driven LAOS phenomenon discloses a relationship between the microscopic structure and the macroscopic properties.

Despite all systems tested, we have not found any overshoot on the storage or the loss modulus. Experimentally, an overshoot on the loss modulus in the nonlinear regime may be found for a filled polymer system, for instance, a carbon black filled SSBR compounds. However, we note that experimentally the amplitude of the effect is small, unless the filler volume fraction is high ($> 30\%$). The absence of clear overshoot in our model may be due to the lack of agglomeration of the fillers. To confirm this interpretation, we have implemented an attractive interaction between the aggregates in the present model. Preliminary results clearly show the effect of the attraction between the fillers on the storage modulus, when compared to the results without attraction. Strikingly also, the computed loss factors are no longer monotonous decreasing functions but display a maximum at the beginning of the nonlinear regime. More work is to be done to elucidate the structural origin of this overshoot.

As a conclusion, we have developed a versatile model to simulate the filled polymer composites and measure the rheology of the compounds. Our model is flexible enough to take into account the size polydispersity, the aggregate rigidity and the interaggregate interactions. We have shown that this simple model, can account for reinforcement, which

is boosted by large rigid aggregates. The Payne effect is also reproduced. Furthermore, it is possible to relate these macroscopic effects to the local configurations of the aggregates.

Perspectives The model is based on the generalized Langevin dynamics which is seen here as a mesoscopic tool, which may help in concentrating on the filler degrees of freedom, treating the polymer around the filler as an effective viscoelastic medium. This strategy has the advantage to tackle the large disparity of relevant length scales, from the monomer units to the filler network size. Specifically, the motion of the polymer chains has been averaged out in the form of a velocity kernel, apt in describing the viscoelasticity of the pure polymer melt. However, the interaction between the polymer chains and the filler particles, which may lead to "bridging" effects between linked particles, has also been discarded. An additional interaction force between fillers or a semi-empirical potential could be considered to account for the contribution of the filler-polymer interface. The precise form it should take remains an open question.

Second, the model in its prime form is designed for repulsive potential between nanoparticles. For most of the situations that we have considered, the configuration of the aggregates is homogeneous and filler agglomeration is not observed. This leads to the lack of the overshoot on the loss modulus, which is usually found in the filled entangled polymer matrix, at high volume fractions however. To build a large filler network, we need to implement attractive force between agglomerates in the present model, in which the filler network may be destructed under large shear deformation, leading to enhanced dissipation at intermediate deformation. Further investigations are needed in order to fully characterize the rheological properties of attractive filler aggregates, and also to unveil the structural origin of the overshoot of the loss tangent.

Third, the present model is flexible and not restricted neither to a given type of filler, nor to a given polymer matrix. The type of fillers is not only limited to the fractal like aggregates or the individual nanoparticles. For nanoparticle, an interesting extension would be to design a velocity kernel that may account for the presence of permanently grafted chains on the nanoparticle surface. Other type of nanofillers, that have attracted recent attention, such as nanotubes or nanofibers, can also be considered in the present model. Furthermore, realistic polymer matrices can be readily considered in the model by using the the corresponding memory kernel. Thus, there are potentially many situations that remain to be explored.

Bibliography

- [1] J. Mark, B. Erman, and M. Roland, *The Science and Technology of Rubber*. Elsevier Science, 2013. 1
- [2] R. Landel and L. Nielsen, *Mechanical Properties of Polymers and Composites, Second Edition*. Mechanical Engineering, Taylor & Francis, 1993. 1
- [3] T. A. Vilgis, G. Heinrich, and M. Kluepell, *Reinforcement of Polymer Nanocomposites: Theory, Experiments and Applications*. 2009. 1, 6, 7, 8, 14, 24, 25
- [4] J. Oberdisse, “Aggregation of colloidal nanoparticles in polymer matrices,” *Soft Matter*, vol. 2, pp. 29–36, 2006. 1
- [5] S. A. Khan and N. J. Zoeller, “Dynamic rheological behavior of flocculated fumed silica suspensions,” *Journal of Rheology*, vol. 37, no. 6, pp. 1225–1235, 1993. 1
- [6] N. Jouault, P. Vallat, F. Dalmas, S. Said, J. Jestin, and F. Boué, “Well-dispersed fractal aggregates as filler in polymer-silica nanocomposites: Long-range effects in rheology,” *Macromolecules*, vol. 42, no. 6, pp. 2031–2040, 2009. 1
- [7] G. P. Baeza, A.-C. Genix, C. Degrandcourt, L. Petitjean, J. Gummel, M. Couty, and J. Oberdisse, “Multiscale filler structure in simplified industrial nanocomposite silica/sbr systems studied by saxs and tem,” *Macromolecules*, vol. 46, no. 1, pp. 317–329, 2013. 1, 7, 8, 11, 12, 35, 53
- [8] Q. Chen, S. Gong, J. Moll, D. Zhao, S. K. Kumar, and R. H. Colby, “Mechanical reinforcement of polymer nanocomposites from percolation of a nanoparticle network,” *ACS Macro Letters*, vol. 4, no. 4, pp. 398–402, 2015. 1
- [9] S. Merabia, P. Sotta, and D. R. Long, “A microscopic model for the reinforcement and the nonlinear behavior of filled elastomers and thermoplastic elastomers (Payne and Mullins effects),” *Macromolecules*, vol. 41, no. 21, pp. 8252–8266, 2008. 1, 23
- [10] A. Papon, H. Montes, M. Hanafi, F. m. c. Lequeux, L. Guy, and K. Saalwächter, “Glass-transition temperature gradient in nanocomposites: Evidence from nuclear magnetic resonance and differential scanning calorimetry,” *Phys. Rev. Lett.*, vol. 108, p. 065702, Feb 2012. 1, 23
- [11] M. M. Kummali, L. A. Miccio, G. A. Schwartz, A. Alegría, J. Colmenero, J. Otegui, A. Petzold, and S. Westermann, “Local mechanical and dielectric behavior of the interacting polymer layer in silica nano-particles filled sbr by means of afm-based methods,” *Polymer*, vol. 54, no. 18, pp. 4980 – 4986, 2013. 1, 23

- [12] T. Glomann, G. J. Schneider, J. Allgaier, A. Radulescu, W. Lohstroh, B. Farago, and D. Richter, "Microscopic dynamics of polyethylene glycol chains interacting with silica nanoparticles," *Phys. Rev. Lett.*, vol. 110, p. 178001, Apr 2013. 1, 23
- [13] M. Krutyeva, A. Wischnewski, M. Monkenbusch, L. Willner, J. Maiz, C. Mijangos, A. Arbe, J. Colmenero, A. Radulescu, O. Holderer, M. Ohl, and D. Richter, "Effect of nanoconfinement on polymer dynamics: Surface layers and interphases," *Phys. Rev. Lett.*, vol. 110, p. 108303, Mar 2013. 1, 23
- [14] Y. N. Pandey, G. J. Papakonstantopoulos, and M. Doxastakis, "Polymer/nanoparticle interactions: Bridging the gap," *Macromolecules*, vol. 46, no. 13, pp. 5097–5106, 2013. 1
- [15] G. Armstrong, "An introduction to polymer nanocomposites," *European Journal of Physics*, vol. 36, no. 6, p. 063001, 2015. 4, 8
- [16] K. Winey and R. Vaia, "Polymer nanocomposites," *MRS Bulletin*, vol. 32, no. April, pp. 314–319, 2007. 4, 5
- [17] D. Y. Godovsky, *Device Applications of Polymer-Nanocomposites*, pp. 163–205. Berlin, Heidelberg: Springer Berlin Heidelberg, 2000. 4
- [18] S. K. Kumar and R. Krishnamoorti, "Nanocomposites: Structure, phase behavior, and properties," *Annual Review of Chemical and Biomolecular Engineering*, vol. 1, no. 1, pp. 37–58, 2010. PMID: 22432572. 4, 8, 24
- [19] S. K. Kumar, B. C. Benicewicz, R. A. Vaia, and K. I. Winey, "50th anniversary perspective: Are polymer nanocomposites practical for applications?," *Macromolecules*, vol. 50, no. 3, pp. 714–731, 2017. 4, 5, 9, 53
- [20] S. Kimoto, W. D. Dick, B. Hunt, W. W. Szymanski, P. H. McMurry, D. L. Roberts, and D. Y. H. Pui, "Characterization of nanosized silica size standards," *Aerosol Science and Technology*, vol. 51, no. 8, pp. 936–945, 2017. 5
- [21] T. Koga, T. Hashimoto, M. Takenaka, K. Aizawa, N. Amino, M. Nakamura, D. Yamaguchi, and S. Koizumi, "New insight into hierarchical structures of carbon black dispersed in polymer matrices: A combined small-angle scattering study," *Macromolecules*, vol. 41, no. 2, pp. 453–464, 2008. 6
- [22] P. Tandon and D. E. Rosner, "Translation brownian diffusion coefficient of large (multi-particle) suspended aggregates," *Industrial & Engineering Chemistry Research*, vol. 34, no. 10, pp. 3265–3277, 1995. 6
- [23] M. Couty, "Structure multiéchelles et propriétés des matériaux du pneu," *Reflète de la Physique*, vol. 12, 2008. 7, 8, 9
- [24] H. D. Bale and P. W. Schmidt, "Small-angle x-ray-scattering investigation of submicroscopic porosity with fractal properties," *Phys. Rev. Lett.*, vol. 53, pp. 596–599, Aug 1984. 7
- [25] J. Jancar, J. Douglas, F. Starr, S. Kumar, P. Cassagnau, A. Lesser, S. Sternstein, and M. Buehler, "Current issues in research on structure–property relationships in polymer nanocomposites," *Polymer*, vol. 51, no. 15, pp. 3321–3343, 2010. 8, 15, 17, 25
- [26] A. Rungta, B. Natarajan, T. Neely, D. Dukes, L. S. Schadler, and B. C. Benicewicz, "Grafting bimodal polymer brushes on nanoparticles using controlled radical polymerization," *Macromolecules*, vol. 45, no. 23, pp. 9303–9311, 2012. 9

- [27] S. K. Kumar, N. Jouault, B. Benicewicz, and T. Neely, "Nanocomposites with polymer grafted nanoparticles," *Macromolecules*, vol. 46, no. 9, pp. 3199–3214, 2013. 9
- [28] P. Akcora, S. K. Kumar, J. Moll, S. Lewis, L. S. Schadler, Y. Li, B. C. Benicewicz, A. Sandy, S. Narayanan, J. Ilavsky, P. Thiyagarajan, R. H. Colby, and J. F. Douglas, "'gel-like' mechanical reinforcement in polymer nanocomposite melts," *Macromolecules*, vol. 43, no. 2, pp. 1003–1010, 2010. 11, 15, 16
- [29] G. Heinrich, M. Klüppel, and T. Vilgis, "Reinforcement of elastomers," *Curr. Opin. Solid State Mater. Sci.*, vol. 6, pp. 195–203, 2002. 10
- [30] K. Hyun, M. Wilhelm, C. O. Klein, K. S. Cho, J. G. Nam, K. H. Ahn, S. J. Lee, R. H. Ewoldt, and G. H. McKinley, "A review of nonlinear oscillatory shear tests: Analysis and application of large amplitude oscillatory shear (LAOS)," *Prog. Polym. Sci.*, vol. 36, no. 12, pp. 1697–1753, 2011. 12, 13
- [31] K. Hyun, S. H. Kim, K. H. Ahn, and S. J. Lee, "Large amplitude oscillatory shear as a way to classify the complex fluids," *Journal of Non-Newtonian Fluid Mechanics*, vol. 107, no. 1, pp. 51 – 65, 2002. 12, 13
- [32] A. Payne, "The dynamic properties of carbon black loaded natural rubber vulcanizates. Part I," *J. Appl. Polym. Sci.*, vol. 6, pp. 57–63, 1962. 12, 14
- [33] J. F. Moll, P. Akcora, A. Rungta, S. Gong, R. H. Colby, B. C. Benicewicz, and S. K. Kumar, "Mechanical reinforcement in polymer melts filled with polymer grafted nanoparticles," *Macromolecules*, vol. 44, no. 18, pp. 7473–7477, 2011. 14
- [34] A. A. Gusev, "Micromechanical mechanism of reinforcement and losses in filled rubbers," *Macromolecules*, vol. 39, no. 18, pp. 5960–5962, 2006. 14
- [35] P. Cassagnau, "Payne effect and shear elasticity of silica-filled polymers in concentrated solutions and in molten state," *Polymer*, vol. 44, no. 8, pp. 2455 – 2462, 2003. 14
- [36] L. Chazeau, J. D. Brown, L. C. Yanyo, and S. S. Sternstein, "Modulus recovery kinetics and other insights into the Payne effect for filled elastomers," *Polymer Composites*, vol. 21, no. 2, pp. 202–222, 2000. 14
- [37] J. Ramier, C. Gauthier, L. Chazeau, L. Stelandre, and L. Guy, "Payne effect in silica-filled styrene–butadiene rubber: Influence of surface treatment," *Journal of Polymer Science Part B: Polymer Physics*, vol. 45, no. 3, pp. 286–298, 2007. 14
- [38] M.-J. Wang, "Effect of polymer-filler and filler-filler interactions on dynamic properties of filled vulcanizates," *Rubber Chemistry and Technology*, vol. 71, no. 3, pp. 520–589, 1998. 14
- [39] J. Diani, B. Fayolle, and P. Gilormini, "A review on the Mullins effect," *European Polymer Journal*, vol. 45, no. 3, pp. 601 – 612, 2009. 14, 15
- [40] T. Davris, M. R. B. Mermet-Guyennet, D. Bonn, and A. V. Lyulin, "Filler Size Effects on Reinforcement in Elastomer-Based Nanocomposites: Experimental and Simulational Insights into Physical Mechanisms," *Macromolecules*, vol. 49, no. 18, pp. 7077–7087, 2016. 16, 18, 21, 22, 57, 64
- [41] T. Desai, P. Koblinski, and S. K. Kumar, "Molecular dynamics simulations of polymer transport in nanocomposites," *The Journal of Chemical Physics*, vol. 122, no. 13, p. 134910, 2005. 16

- [42] Q. H. Zeng, A. B. Yu, G. Q. Lu, and R. K. Standish, "Molecular dynamics simulation of organic-inorganic nanocomposites: Layering behavior and interlayer structure of organoclays," *Chemistry of Materials*, vol. 15, no. 25, pp. 4732–4738, 2003. 16
- [43] G. D. Smith, D. Bedrov, L. Li, and O. Byutner, "A molecular dynamics simulation study of the viscoelastic properties of polymer nanocomposites," *The Journal of Chemical Physics*, vol. 117, no. 20, pp. 9478–9489, 2002. 16
- [44] J. Liu, Y. Gao, D. Cao, L. Zhang, and Z. Guo, "Nanoparticle dispersion and aggregation in polymer nanocomposites: Insights from molecular dynamics simulation," *Langmuir*, vol. 27, no. 12, pp. 7926–7933, 2011. PMID: 21595451. 16
- [45] K. S. Schweizer and J. G. Curro, "Integral equation theories of the structure, thermodynamics, and phase transitions of polymer fluids," pp. 1–142, 2007. 16
- [46] L. M. Hall, A. Jayaraman, and K. S. Schweizer, "Molecular theories of polymer nanocomposites," *Curr. Opin. Solid State Mater. Sci.*, vol. 14, no. 2, pp. 38–48, 2010. 16, 18
- [47] D. W. Oxtoby, "Density functional methods in the statistical mechanics of materials," *Annual Review of Materials Research*, vol. 32, no. 1, pp. 39–52, 2002. 17
- [48] G. Fredrickson, *The Equilibrium Theory of Inhomogeneous Polymers*. International Series of Monogr, OUP Oxford, 2006. 18
- [49] D. D. Biondo, E. M. Masnada, S. Merabia, M. Couty, and J.-L. Barrat, "Numerical study of a slip-link model for polymer melts and nanocomposites," *The Journal of Chemical Physics*, vol. 138, no. 19, p. 194902, 2013. 18, 19, 49
- [50] E. Masnada, S. Merabia, M. Couty, and J.-L. Barrat, "Entanglement-induced reinforcement in polymer nanocomposites," *Soft Matter*, vol. 9, pp. 10532–10544, 2013. 18, 19, 20
- [51] S. Edwards and T. Vilgis, "The effect of entanglements in rubber elasticity," *Polymer*, vol. 27, no. 4, pp. 483 – 492, 1986. 18
- [52] M. Rubinstein and S. Panyukov, "Elasticity of polymer networks," *Macromolecules*, vol. 35, no. 17, pp. 6670–6686, 2002. 18
- [53] Y. Masubuchi, J.-I. Takimoto, K. Koyama, G. Ianniruberto, G. Marrucci, and F. Greco, "Brownian simulations of a network of reptating primitive chains," *The Journal of Chemical Physics*, vol. 115, no. 9, pp. 4387–4394, 2001. 18
- [54] A. E. Likhtman, "Single-chain slip-link model of entangled polymers: Simultaneous description of neutron spin-echo, rheology, and diffusion," *Macromolecules*, vol. 38, no. 14, pp. 6128–6139, 2005. 18
- [55] P. J. Hoogerbrugge and J. M. V. A. Koelman, "Simulating microscopic hydrodynamic phenomena with dissipative particle dynamics," *EPL (Europhysics Letters)*, vol. 19, no. 3, p. 155, 1992. 19
- [56] C. H. Park, E. Tocci, E. Fontananova, M. A. Bahattab, S. A. Aljlil, and E. Drioli, "Mixed matrix membranes containing functionalized multiwalled carbon nanotubes: Mesoscale simulation and experimental approach for optimizing dispersion," *Journal of Membrane Science*, vol. 514, no. Supplement C, pp. 195 – 209, 2016. 20

- [57] A. Karatrantos, N. Clarke, and M. Kröger, “Modeling of polymer structure and conformations in polymer nanocomposites from atomistic to mesoscale: A review,” *Polymer Reviews*, vol. 56, no. 3, pp. 385–428, 2016. 20, 21, 31
- [58] G. Raos, M. Moreno, and S. Elli, “Computational experiments on filled rubber viscoelasticity: What is the role of particle-particle interactions?,” *Macromolecules*, vol. 39, no. 19, pp. 6744–6751, 2006. 21
- [59] H. M. Smallwood, “Limiting law of the reinforcement of rubber,” *Journal of Applied Physics*, vol. 15, no. 11, pp. 758–766, 1944. 21
- [60] E. Guth, “Theory of filler reinforcement,” *Journal of Applied Physics*, vol. 16, no. 1, pp. 20–25, 1945. 21
- [61] D. Moldovan, R. Fechete, D. Demco, E. Culea, B. Blümich, V. Herrmann, and M. Heinz, “The heterogeneity of segmental dynamics of filled epdm by 1h transverse relaxation nmr,” *Journal of Magnetic Resonance*, vol. 208, no. 1, pp. 156 – 162, 2011. 22
- [62] M. A. Osman and A. Atallah, “Effect of the particle size on the viscoelastic properties of filled polyethylene,” *Polymer*, vol. 47, no. 7, pp. 2357 – 2368, 2006. Single Chain Polymers. 22
- [63] S. S. Sternstein and A.-J. Zhu, “Reinforcement mechanism of nanofilled polymer melts as elucidated by nonlinear viscoelastic behavior,” *Macromolecules*, vol. 35, no. 19, pp. 7262–7273, 2002. 22
- [64] A. S. Sarvestani and E. Jabbari, “Modeling the viscoelastic response of suspension of particles in polymer solution: The effect of polymer-particle interactions,” *Macromolecular Theory and Simulations*, vol. 16, no. 4, pp. 378–385, 2007. 22
- [65] G. D. Smith, D. Bedrov, and O. Borodin, “Structural relaxation and dynamic heterogeneity in a polymer melt at attractive surfaces,” *Phys. Rev. Lett.*, vol. 90, p. 226103, Jun 2003. 23
- [66] Y. Song and Q. Zheng, “Concepts and conflicts in nanoparticles reinforcement to polymers beyond hydrodynamics,” *Progress in Materials Science*, vol. 84, no. Supplement C, pp. 1 – 58, 2016. 23
- [67] Z. Zhu, T. Thompson, S.-Q. Wang, E. D. von Meerwall, and A. Halasa, “Investigating linear and nonlinear viscoelastic behavior using model silica-particle-filled polybutadiene,” *Macromolecules*, vol. 38, no. 21, pp. 8816–8824, 2005. 23, 52, 64
- [68] M. Vacatello, “Predicting the molecular arrangements in polymer-based nanocomposites,” *Macromolecular Theory and Simulations*, vol. 12, no. 1, pp. 86–91, 2003. 23
- [69] M. S. Ozmusul, C. R. Picu, S. S. Sternstein, and S. K. Kumar, “Lattice monte carlo simulations of chain conformations in polymer nanocomposites,” *Macromolecules*, vol. 38, no. 10, pp. 4495–4500, 2005. 23
- [70] V. Arrighi, J. Higgins, A. Burgess, and G. Floudas, “Local dynamics of poly(dimethyl siloxane) in the presence of reinforcing filler particles,” *Polymer*, vol. 39, no. 25, pp. 6369 – 6376, 1998. 23
- [71] Y. Song and Q. Zheng, “Linear rheology of nanofilled polymers,” *J. Rheol.*, vol. 59, no. 1, pp. 155–191, 2015. 24

- [72] F. Yatsuyanagi, N. Suzuki, M. Ito, and H. Kaidou, "Effects of secondary structure of fillers on the mechanical properties of silica filled rubber systems," *Polymer*, vol. 42, no. 23, pp. 9523 – 9529, 2001. 24
- [73] L. S. Schadler, S. K. Kumar, B. C. Benicewicz, S. L. Lewis, and S. E. Harton, "Designed interfaces in polymer nanocomposites: A fundamental viewpoint," *MRS Bulletin*, vol. 32, no. 4, p. 335–340, 2007. 24
- [74] M. Bailly and M. Kontopoulou, "Linear viscoelastic properties of ethylene–octene copolymer/nanosilica composites investigated over a broad range of frequencies," *Journal of Rheology*, vol. 57, no. 2, pp. 407–426, 2013. 24
- [75] Q. Zhang and L. A. Archer, "Poly(ethylene oxide)/silica nanocomposites: Structure and rheology," *Langmuir*, vol. 18, no. 26, pp. 10435–10442, 2002. 24
- [76] P. Akcora, S. K. Kumar, V. García Sakai, Y. Li, B. C. Benicewicz, and L. S. Schadler, "Segmental dynamics in pmma-grafted nanoparticle composites," *Macromolecules*, vol. 43, no. 19, pp. 8275–8281, 2010. 24, 53
- [77] M. Rubinstein and R. Colby, *Polymer Physics*. OUP Oxford, 2003. 26, 28
- [78] M. Doi, *Introduction to Polymer Physics*. Oxford science publications, Clarendon Press, 1996. 26, 29
- [79] Q. Zeng, A. Yu, and G. Lu, "Multiscale modeling and simulation of polymer nanocomposites," *Progress in Polymer Science*, vol. 33, no. 2, pp. 191 – 269, 2008. 31
- [80] A. D. Baczewski and S. D. Bond, "Numerical integration of the extended variable generalized Langevin equation with a positive Prony representable memory kernel," *J. Chem. Phys.*, vol. 139, no. 4, 2013. 31, 38, 39, 40, 41, 43
- [81] T. A. Witten and L. M. Sander, "Diffusion-limited aggregation, a kinetic critical phenomenon," *Phys. Rev. Lett.*, vol. 47, pp. 1400–1403, Nov 1981. 33
- [82] A. Khokhlov, *Statistical Physics of Macromolecules*. AIP series in polymers and complex materials, AIP Press, 1994. 36
- [83] B. Schnurr, F. Gittes, F. C. MacKintosh, and C. F. Schmidt, "Determining microscopic viscoelasticity in flexible and semiflexible polymer networks from thermal fluctuations," *Macromolecules*, vol. 30, no. 25, pp. 7781–7792, 1997. 38
- [84] F. MacKintosh and C. Schmidt, "Microrheology," *Current Opinion in Colloid & Interface Science*, vol. 4, no. 4, pp. 300 – 307, 1999. 38
- [85] D. Chandler, *Introduction to Modern Statistical Mechanics*. Oxford University Press, 1987. 47, 48, 49
- [86] M. Doi and S. Edwards, *The Theory of Polymer Dynamics*. International series of monographs on physics, Clarendon Press, 1988. 48, 60
- [87] J. Ramírez, S. K. Sukumaran, and A. E. Likhtman, "Significance of cross correlations in the stress relaxation of polymer melts," *The Journal of Chemical Physics*, vol. 126, no. 24, p. 244904, 2007. 49, 50
- [88] M. Allen and D. Tildesley, *Computer Simulation of Liquids*. Oxford Science Publ, Clarendon Press, 1989. 65, 66, 68, 69

- [89] A. W. Lees and S. F. Edwards, “The computer study of transport processes under extreme conditions,” *Journal of Physics C: Solid State Physics*, vol. 5, no. 15, p. 1921, 1972. 68
- [90] D. Evans and G. Morriss, *Statistical Mechanics of Nonequilibrium Liquids*. Cambridge University Press, 2008. 68, 69
- [91] D. J. Evans and O. Morriss, “Non-newtonian molecular dynamics,” *Computer Physics Reports*, vol. 1, no. 6, pp. 297 – 343, 1984. 69
- [92] K. S. Cho, K. Hyun, K. H. Ahn, and S. J. Lee, “A geometrical interpretation of large amplitude oscillatory shear response,” *Journal of Rheology*, vol. 49, no. 3, pp. 747–758, 2005. 70
- [93] M. R. B. Mermet-Guyennet, J. G. de Castro, M. Habibi, N. Martzel, M. M. Denn, and D. Bonn, “Laos: The strain softening/strain hardening paradox,” *Journal of Rheology*, vol. 59, no. 1, pp. 21–32, 2015. 70
- [94] R. H. Ewoldt, A. E. Hosoi, and G. H. McKinley, “New measures for characterizing nonlinear viscoelasticity in large amplitude oscillatory shear,” *Journal of Rheology*, vol. 52, no. 6, pp. 1427–1458, 2008. 70
- [95] S. Hadizadeh, A. Linhananta, and S. S. Plotkin, “Improved measures for the shape of a disordered polymer to test a mean-field theory of collapse,” *Macromolecules*, vol. 44, no. 15, pp. 6182–6197, 2011. 77

